



University of Crete, Physics Department

Foundation of Research and Technology Hellas,
Institute of Electronic Structure and Laser

Master Thesis

# Fabrication of 3D low THz metamaterials via 2-Photon Polymerization

SAVVAS PAPAMAKARIOS

Supervisor
Dr. Maria Farsari

Co-Supervisor
Prof. Maria Kafesaki &
Prof. Konstantinos Makris

Heraklion 2023

## Acknowledgments

Reaching to the end of my master, I take a look back and see many people that worked in order to realize the present research. First, I would like to thank my supervisors Dr. Maria Farsari, Prof. Maria Kafesaki and Prof. Konstantinos Makris for the scientific guidance and trust they showed to me. This extensive research also, could not be done without the support and knowledge of Dr. Gordon Zyla, Dr. Odysseas Tsilipakos and Dr. Mary Manousidaki which all of them did their best to educate and guide me throughout my thesis.

I would like also to deeply thank the members of Non Linear Lithography group, which are not only good co-workers but also good friends. In addition, I would like to thank UNIS group and more especially Dr. Anastasios Koulouklidis and Christina Daskalaki for the excellent collaboration in the characterization of my samples and our technician Aleka Manousaki for her work in SEM. Last but not least, kindly thank to my previous supervisor in my bachelor thesis, Prof. Kosmas Tsakmakidis from University of Athens, for his dedication to impart me all this beautiful knowledge about metamaterials.

Last but not least, I have to deeply thank my family, my friends and all the special people that are close to me everyday and they are important part of my life, sometimes in person and other times from distance, encouraging me to keep going forward.

# Abstract

Metamaterials are artificial designed materials that can enhance nature's characteristics and provide extraordinary properties in varying fields. One of the most important categories of metamaterials are the electromagnetic, where specific architecture of the meta-atom can manipulate the electromagnetic field in scaling frequencies and wavelengths. In the present thesis the study is focused on low THz (0.1-10 THz) regime, which is an important frequency band since there are no known nature's materials that can interact with electromagnetic waves in these wavelengths scale, known as the THz gap. For this reason, it is of high interest to find ways to manipulate light at these frequencies, to evolve and expand THz technology in sensing and telecommunication applications.

In order to achieve the manipulation of low THz frequencies, the meta-atoms have to be optimized to enhance the electromagnetic response in this regime. Thus, it is crucial for the study and development of metamaterials to use simulations. For the simulations, Finite Different Time Domain (FDTD) method was used that has been shown to be one of the most accurate computational methods for electromagnetic research. For the fabrication of the metamaterials, 2-photon polymerization (2PP) was used to provide the high resolution that this frequency regime requires and the capability of fabricating dielectric and metallo-dielectric structures. Theoretical models of classical cross-shaped Split Ring Resonators (SRRs) were developed to explain the effects of broken symmetries in electromagnetic metamaterials and introduce the main study which is the fabrication and characterization of a state-of-the-art asymmetric pillar SRR that provides Electromagnetically Induced Transparency (EIT) in the frequency band of 2 THz. The whole complex and challenging process, from the synthesis of the photosensitive material until the final characterization of the sample is highlighted through the present thesis.

In addition, the final part of the thesis is focused on some of the applications that metamaterials and 2PP combined can provide, making the transition from virtual environment of simulations to reality in a straightforward way, for varying frequency bands.

# Contents

.

# 1 Introduction

## 1.1 Motivation

Metamaterials changed the way we understand miracles of nature. The original idea of metamaterials can be traced back to the origin of electromagnetism as it was described by James Clark Maxwell [1].
Maxwell's equations:
Faraday: $\frac{\partial \overrightarrow{B}}{\partial t} = -\overrightarrow{\nabla} \times \overrightarrow{E} - \overrightarrow{M}$ (differential form)
$\frac{\partial}{\partial t} \iint_A \overrightarrow{B} d\overrightarrow{A} = -\oint_l \overrightarrow{E} d\overrightarrow{l} - \iint_A \overrightarrow{M} d\overrightarrow{A}$ (calculus form)
Ampere: $\frac{\partial \overrightarrow{D}}{\partial t} = -\overrightarrow{\nabla} \times \overrightarrow{H} - \overrightarrow{J}$ (differential form)
$\frac{\partial}{\partial t} \iint_A \overrightarrow{D} d\overrightarrow{A} = -\oint_l \overrightarrow{H} d\overrightarrow{l} - \iint_A \overrightarrow{J} d\overrightarrow{A}$ (calculus form)
Gauss for electric field: $\nabla \overrightarrow{D} = 0$ (differential form)
$\oint \oint_A \overrightarrow{D} d\overrightarrow{A} = 0$ (calculus form)
Gauss for magnetic field: $\nabla \overrightarrow{B} = 0$ (differential form)
$\oint \oint_A \overrightarrow{B} d\overrightarrow{A} = 0$ (calculus form)

**AND THEN BECAME THE LIGHT**

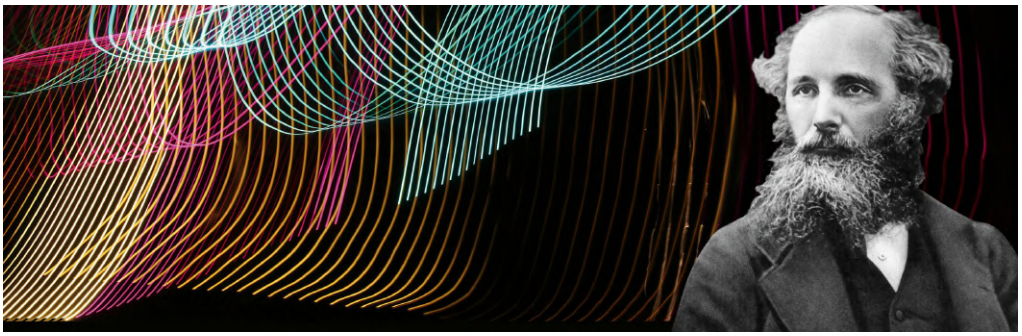

Figure 1: James Clark Maxwell [cosmosmagazine]

Metamaterials comes from the Greek word "$\mu\epsilon\tau\alpha$" which means "beyond" and materials. They are artificial materials that can enhance nature's characteristics and tuned in different ways to give the desirable results. The most commonly used categories of metamaterials are electromagnetic, acoustic and mechanical in order to manipulate light, sound and mechanical properties respectively [2].

THz band remained unexplored for many years despite the rapid growth of technology. The THz band is an area of convergence between the electronics field (up from lower frequencies) and the photonics field (down from higher frequencies). Realization of THz applications in optical, imaging and telecommunication industries seems challenging until now since no mature systems and applications exist yet [3]. There are indications that this can be solved using metamaterials instead of natural elements that can provide exotic characterisitcs in scaling frequencies. But, fabrication of metamaterials in the regime requires 3D printing techniques that can provide high resolution structures. One of the most suitable fabrication techniques for this kind of metamaterials it is settled to be 2-photon polymerization.

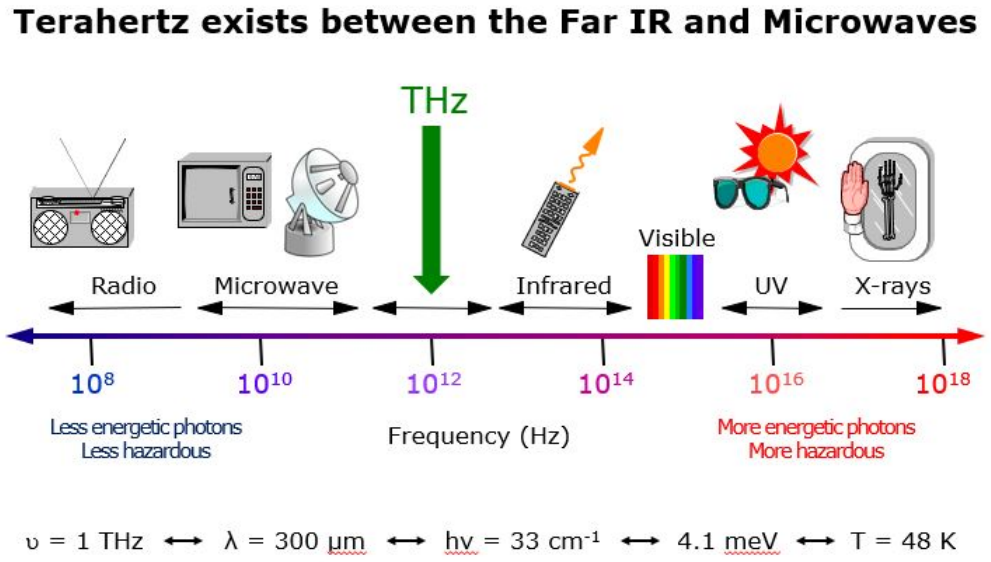


Figure 2.3.1: Electromagnetic spectrum with applications in electronic's and photonic's industry. [Obtained from LUNAinc.]

## 1.2 State of the art

Metamaterials are made in the same way common materials are, made of atoms. In common materials the design of the atoms gives the specific characteristics and properties. Now, meta-atoms design and specific geometric design can give to the complex system extraordinary characteristics that it is impossible to find in common materials in nature. This is done by aligning meta-atoms periodically. Also this behaviour can be achieved at asymmetrical geometrical patterns as it is going to presented later, or by changing chemical composition of some materials following counter-intuitive custom properties. Metamaterials were first investigated at the early of $21^{th}$ century when the first experiments were conducted in order to control a material's permittivity $\epsilon$, and permeability $\mu$. Permittivity and permeability are strongly related to the refractive index of a material since $n = \sqrt{\epsilon\mu}$. Some exotic characteristics of metamaterials that was studied in the beginning were the negative permittivity and permeability for the electromagnetic metamaterials that there were resulting to negative refractive index, n, metamaterials or the epsilon near zero (ENZ) materials were the permittivity tend to reach the value 0 at specific wavelengths. This application was first introduced by J.Pendry in 1999 with the investigation of the breakthrough geometry of split ring resonators (SRR) [2] which allowed scientists to search deeper in the field of electromagnetic metamaterials.

Due to the applications that can take place in everyday life and help in fields as telecommunications, energy harvesting, biological applications etc, the most important and known category of metamaterials is the electromagnetic. The ability to tune $\epsilon$ and $\mu$ leads to the fabrication of photonic crystals, perfect lenses, a big variety of sensors, invisible cloaks, antennas and many other applications [4]. Depending on the size of the meta-atom metamaterials can also be tuned to operate in different frequency regimes, giving the opportunity to enrich sensing technology from microwave to optical wavelengths. This advantage led to the highly impact research that it is conducted the last two decades. With the advance and the rapid growth of technology, metamaterials nowadays are much easier to be fabricated and the applications of electromagnetic metamaterials are expanding in many fields.

A very important characteristic of electromagnetic metamaterials is the negative refractive index that they exhibit under specific circumstances that

was first introduced by V. Veselago [5] and studied thoroughly later by D. R. Smith and J. Pendry [6]. This had a huge impact on artificial materials and their properties and negative refractive index metamaterials (or left handed metamaterials) have been the main research interest for many researchers for years. These materials can lead to insignificant losses [7] which is very important due to the fact that metamaterials are build up of metallic or dielectric meta-atoms which cause high dissipative losses. This extraordinary characteristic can lead to the manipulation of light or electromagnetic waves at specific wavelengths depending on the size of the meta-atom unit cell. In order to achieve the negative reftactive index $n$, both $\epsilon$ and $\mu$ must be negative. The negative $\epsilon$ is easier to achieved by using nature's materials and more specific metallic wires [8], but the challenging part is to create negative permeability. This was achieved by the use of split rings resonators (SRR) that they were designed properly and gave both negative $\epsilon$ and $\mu$ in the same frequency band [9]. The first applications of SRR were focused on chiral metamaterials in the microwave regime by D. R. Smith et al [10] and opened the way to manipulate light in different wavelengths focusing on chiral behaviours such as circular dichroism, negative refraction and polarizers from circulary polarized light propagating through these chiral metamaterials [9].

Over the past few years metallic metamaterials have have gained enormous interest in research because they can provide very interesting applications in a variety of fields such as ultra-sensitive biosensors [11], plasmon resonance chemical sensors [12], solar thermal energy absorbers [13], photoconductive low THz metamaterials switchers [14] and perfect absorbers [15] just to name a few. Another important field that had gain a lot of interest lately is low THz electromagnetic metamaterials. In general, the term "low" THz refers to the regime 0.1-10 THz or from 3 $mm$ to 30 $\mu m$. From this aspect, most of the materials that can be found in nature lack of electromagnetic response in THz band and the existing materials causes high losses due to their bulky shape and zero magnetic response in these frequencies [16]. By using electromagnetic metamaterials in low THz band a powerful tool is created to fabricate functional perfect absorption [17] , electromagnetic semi-transparent and transparent devices [18] and wavefront shaping structures through the manipulation of the phase (from 0 to $2\pi$) and amplitude (from 0 to infite) of electromagnetic waves [19].

Depending on the application, low THz metamaterials can be constructed by periodic [20] or non-periodic [21] arrangement of dielectric or more commonly used metallic meta-atoms that has specific geometry and architecture to manipulate light at THz spectrum modulation, wavefront modulation and polarization modulation [22] . Usually in this THz band, asymmetries in one direction take place or intentionally not perfectly aligned meta-atoms are used for the development and fabrication of the metamaterials.

In order to fabricate perfect absorption metamaterials for applications in avoiding electromagnetic interference and be used as filters the tunability and the designability of metamaterials provide a great advantage compared to nature's materials that are expressing high losses. To calculate the absorption coefficient at the desired frequency it is mandatory to measure the reflection and transmission coefficients. From the aspect of metamaterials this is something more than possible since by optimizing the architecture a metamaterial absorber with the desired characteristics can be achieved, by tuning the metamaterial to operate with values close to zero for the reflection and transmission coefficients since the absorption coefficient is obtained by the formula $A(\omega) = 1 - R(\omega) - T(\omega)$, $\omega$ represents the frequency, where $R(\omega)$ and $T(\omega)$ are the reflection and transmission coefficients [16], respectively.

The transmission and reflection coefficients can calculated by the Scattering parameters (S-parameters). S-parameters describe the electrical behavior of linear electrical systems when undergoing various steady state stimuli by electric signals and more specific in electromagnetic materials by electromagnetic waves. These parameters are calculated from the incident wave, the reflected wave and the transmitted wave. What is more important in studying metamaterials are the S-parameters $|S_{11}|^2$ and $|S_{21}|^2$ which represents reflectivity R and transmissivity T [23].

In order to optimize the efficiency of electromagnetic metamaterials is mandatory to use simulations to find out the suitable architecture of the meta-atoms. One of the most well known and reliable computational methods for electromagnetic simulations is Finite Difference Time Domain (FDTD) method. FDTD is a numerical analysis technique for simulating computational electrodynamics that was first introduced by Kane S. Yee on 1966 [24] and it is suitable for solving Maxwell's equations using partial differential

equations. Since it is a time domain-method it can cover a wide frequency range and handle nonlinear material properties in an effective way as the evaluation of this method presented by Allen Taflove [25]. Using the FDTD method, the S-parameters can be theoretically predicted precisely and fast while the parameters that are inserted in the simulation tend to reach the experiment's conditions. Thus, this is a handful tool to develop and fabricate electromagnetic metamaterials that can accurately be tailored to operate at any desired frequency. Aspiration of developing and fabricating metamaterials is to match the Scattering parameters of reflection and transmission from the simulations and the experimental results.

To manipulate low THz frequencies by metamaterials, the meta-atoms should be ideally smaller than the wavelength of interest (depending on the application and wavelength, the unit cell varies from $\lambda/2$ up to $\lambda/10$ [26]). For the fabrication, using 3D printing by 2-Photon Polymerization (2PP) is highly suitable since it provides the required resolution and enables to manufacture true 3D dielectric and metallic (metallodielectric) meta-atoms in a simple workflow [27]. This printing technique uses computer-aided design (CAD) that allows accurately designing of meta-atoms even at large areas compared to the size of the unit cell (up to a few $cm^2$ areas). It is a non-linear phenomenon based on the theory of absorbing two photons quasi-simultaneously and can reach a spatial resolution of 100 nm or sometimes greater [28]. It can fabricate 3D structures which are highly important for low THz regime [29], or even 2D structures with high accuracy [30]. 2PP technique is one of the most suitable printing techniques in order to fabricate dielectric/metallic structures at micro- and nanoscale and therefore to fabricate electromagnetic metamaterials with multiple scale lengths in a fast, repeatable and mask-less (in contrast with common lithography techniques) way [31].

# 2 Theoretical background

## 2.1 Electromagnetic metamaterials and Maxwell's equations

In order to define metamaterials, and more especially electromagnetic metamaterials, it is critical to create a flexible analogy to conventional materials that are found in nature. Matter consists of atoms and depending on the architecture of the atoms that are arranged in space, matter gets specific characteristics. In the same sense metamaterial is composed of its elements, the meta-atoms [32]. These structural elements of metamaterials are made of conventional materials that are made from normal atoms. This periodic structure that build up the metamaterial resemble natural crystals that have a specific periodically arranged atoms with predetermined atomic radius which comes in an analogy with unit cell's size of the meta-atom. The unit cells in metamaterials are not made of physical atoms or molecules but from small metallic or dielectric resonators which causes the electromagnetic interaction. The way that the incident electromagnetic wave interacts with these "resonators" determines the artificial material's electromagnetic properties [33].

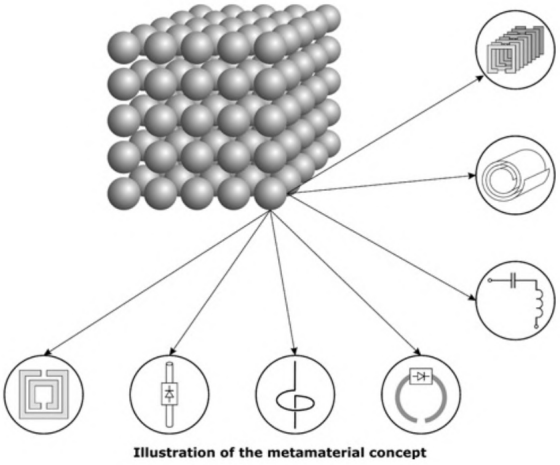


Figure 2.1.1: Illustration of the metamaterial concept in analogy to nature's materials, operating as small "resonators" [32].

By custom-designing meta-atom's geometry and dimensions it is possible to create extraordinary electromagnetic properties. One of the most characteristic and important property is when the electric permittivity and magnetic permeability become at the same time (same frequency region) negative. This response can be analyzed using the effective permittivity $\epsilon_{eff} = \epsilon_0 \epsilon_r$, where $\epsilon_{eff} = \epsilon(\omega)$ is the complex frequency-dependent permittivity of the material, $\epsilon_0$ the vacuum permittivity and $\epsilon_r$ the relative permittivity which is a characteristic of the material, and effective permeability $\mu_{eff} = \mu_0 \mu_r$ accordingly. The term "effective" refers to the fact that is calculated averaged over the volume of the unit cell. In order to have electromagnetic interaction the size of the unit cell, $\alpha$, has to be much smaller than the wavelength of the incident wave ($\alpha \ll \lambda$) [33].

In the interest of introducing the terms permittivity and permeability it is mandatory to study Maxwell's equations thoroughly and understand how these values affects the electromagnetic interaction between wave and matter. Maxwell's equations are a set of partial differential equations providing a mathematical model to explain how the electric and magnetic field are generated and how they change through the interaction with matter. It consists of four -doubled- equations:

Faraday: $\dfrac{\partial \overrightarrow{B}}{\partial t} = -\overrightarrow{\nabla} \times \overrightarrow{E} - \overrightarrow{M}$ (differential form) (2.1.1.a)

$\dfrac{\partial}{\partial t} \iint_A \overrightarrow{B} d\overrightarrow{A} = -\oint_l \overrightarrow{E} d\overrightarrow{l} - \iint_A \overrightarrow{M} d\overrightarrow{A}$ (calculus form) (2.1.1.b)

Ampere: $\dfrac{\partial \overrightarrow{D}}{\partial t} = -\overrightarrow{\nabla} \times \overrightarrow{H} - \overrightarrow{J}$ (differential form) (2.1.2.a)

$\dfrac{\partial}{\partial t} \iint_A \overrightarrow{D} d\overrightarrow{A} = -\oint_l \overrightarrow{H} d\overrightarrow{l} - \iint_A \overrightarrow{J} d\overrightarrow{A}$ (calculus form) (2.1.2.b)

Gauss for electric field: $\nabla \overrightarrow{D} = 0$ (differential form) (2.1.3.a)

$\oint \oint_A \overrightarrow{D} d\overrightarrow{A} = 0$ (calculus form) (2.1.3.b)

Gauss for magnetic field: $\nabla \overrightarrow{B} = 0$ (differential form) (2.1.4.a)

$\oint \oint_A \overrightarrow{B} d\overrightarrow{A} = 0$ (calculus form) (2.1.4.b)

The terms that are shown on Maxwell's equations are:

$\overrightarrow{E}$: Electric field( $Volts/meter$)
$\overrightarrow{D}$: Electric flux density($coulombs/meter^2$)
$\overrightarrow{H}$: Magnetic field ($ampers/meter$)
$\overrightarrow{B}$: Magnetic flux density ($weber/meter^2$)
$A$: Arbitrary 3D surface
$d\overrightarrow{A}$: Differential normal vector that characterizes surface A($meter^2$)
$l$: Close contour that bounds surface A
$d\overrightarrow{l}$: Differential length vector that characterizes contour $l$
$\overrightarrow{J}$: Electric current density ($amperes/meter^2$)
$\overrightarrow{M}$: Magnetic current density($volts/meter^2$)
and $\overrightarrow{\nabla} = \left[\frac{\partial}{\partial x}, \frac{\partial}{\partial y}, \frac{\partial}{\partial z}\right]$

In order to describe the basic properties of metamaterials and introduce the terms of $\epsilon$ and $\mu$, Maxwell's equations must be rewritten considering the fact that $\overrightarrow{D} = \epsilon\overrightarrow{E}$ and $\overrightarrow{B} = \mu\overrightarrow{H}$, where:
$\epsilon$: electrical permittivity($farads/meter$)
$\epsilon_0$: free-space permittivity($8.854 * 10^{-12} farads/meter$)
$\epsilon_r$: relative permittivity(dimensionless scalar)
$\mu$: magnetic permeability (henrys/meter)
$\mu_0$: free-space permeability($4\pi * 10^{-7} henrys/meter$)
$\mu_r$: magnetic permeability (dimensionless scalar).

⌈ **All of the above equations and definitions are obtained from A. Taflove and S. C. Hagness book "Computational Electrodynamics: The finite-Difference Time-Domain method" [34]** ⌋

Also, it is reasonable to consider that there are no generated field from currents and set $\overrightarrow{J} = \overrightarrow{M} = 0$ as well as no losses appears to the system. Then, Maxwell's equations 2.1.1.a and 2.1.2.a become:

$\overrightarrow{\nabla} \times \overrightarrow{E} = -\mu_0\mu_r\frac{\partial\overrightarrow{H}}{\partial t}$ (2.1.5.a) and $\overrightarrow{\nabla} \times \overrightarrow{H} = \epsilon_0\epsilon_r\frac{\partial\overrightarrow{E}}{\partial t}$ (2.1.5.b), respectively.

From the equations (2.1.5.a) and (2.1.5.b) the general electromagnetic, time dependent, equation is formed:

$\nabla^2 \overrightarrow{E} = -\epsilon_0 \mu_0 \epsilon_r \mu_r \frac{\partial^2 E}{\partial t^2}$ (2.1.6).

Since there are no losses and $\epsilon_r$ and $\mu_r$ are real numbers, the wave equation (2.1.6) is unchanged when the signs of $\epsilon_r$ and $\mu_r$ simultaneously change. If we assume a time-harmonic plane-wave variation for fields in (2.1.5.a), (2.1.5.b) and (2.1.6): $\overrightarrow{E}(x, y, z, t) = \overrightarrow{E} e^{i\omega t - i \overrightarrow{k}\,\overrightarrow{r}}$, where $\omega$ is the frequency and $\overrightarrow{k}$ the wavevector (similar equation for $\overrightarrow{H}$), then (2.1.5.a) and (2.1.5.b) are taking the form: $\overrightarrow{k} \times \overrightarrow{E} = -\omega \mu_0 \mu_r \overrightarrow{H}$ (2.1.5.c) and $\overrightarrow{k} \times \overrightarrow{H} = \omega \epsilon_0 \epsilon_r \overrightarrow{E}$ (2.1.5.d), accordingly. For $\epsilon_r > 0$ and $\mu_r > 0$ the vectors $\overrightarrow{E}, \overrightarrow{H}, \overrightarrow{k}$ form a right-handed triplet of vectors, while if $\epsilon_r < 0$ and $\mu_r < 0$ the vectors $\overrightarrow{E}, \overrightarrow{H}, \overrightarrow{k}$ form a left-handed triplet of vectors [33]. This is the first indicator for the existence of left-handed materials (LHM) [35] (or negative-index materials [36]), the origin of electromagnetic metamaterials.

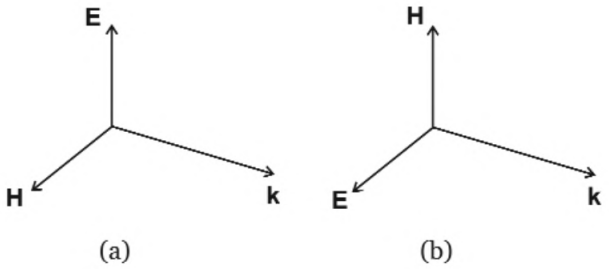


Figure 2.1.2: (a) Right-hand orientation of vectors $\overrightarrow{E}, \overrightarrow{H}, \overrightarrow{k}$ when $\epsilon_r > 0$ and $\mu_r > 0$. (b) Left-hand orientation of vectors $\overrightarrow{E}, \overrightarrow{H}, \overrightarrow{k}$ when $\epsilon_r < 0$ and $\mu_r < 0$ [33].

In order to understand better why this left handed system is so important for metamaterials a deeper research of the small "resonators" is needed. The three basic characteristics that are responsible for the interaction between the electromagnetic waves and matter are permittivity $\epsilon$, permeability $\mu$ and conductivity $\sigma$. These parameters are frequency-dependent for dielectric and

metallic materials that can be found in nature and they have individual values for these properties [37]. These dispersive materials have a significantly property that the electromagnetic wave travels through the medium with variable speed depending on the frequency. The speed is defined by the wave (or phase) speed $u = \frac{\omega}{k}$ (2.1.6.a), where $\omega$ is the frequency and k the wavevector. Phase speed is also defined as $u = \frac{1}{\epsilon(\omega)\mu(\omega)}$ (2.1.6.b) so it is directly depended on the frequency. For example, it is known that in the free space $\epsilon_r = \mu_r = 1$. Thus, the phase or propagation speed of the wave is the speed of light $c_0$ which is defined as $c_0 = \frac{1}{\epsilon_0\mu_0}$ (2.1.6.c). Also, permittivity and permeability values define the refractive index of the medium which is also frequency-dependent: $n = \sqrt{\epsilon(\omega)\mu(\omega)}$ (2.1.6.d). Since permittivity and permeability are complex numbers ($\epsilon = \epsilon' + i\epsilon''(2.1.6.d), \mu = \mu' + i\mu''(2.1.6.e)$), real part of refractive index ($n = n' + in''$)(2.1.6.$f$) can take negative values when both of the $\epsilon'$ and $\mu'$ are negative simultaneously [38]. So the left-handed system of axis is very important to define and explain on theory level the existence of negative refractive index values [39].

Next, we considered that the meta-atoms of the medium are functioning as small "resonators" like the electrons inside the atom. This behaviour can be perfectly described by the Drude-Lorentz model for dielectrics which leads also to the reason why permittivity and permeability are frequency depended is this category of materials [40]. First, there is an oscillation around an equilibrium time where a bonding force is generated; $F_1 = -kx = -m\omega_0^2 x$ (2.1.7.a), the known Hooke's law and a second force due to the deadening of vibrations $F_2 = -m\gamma\frac{dx}{dt}$ (2.1.7.b)[41], in a simplified model on one dimension. The third force origins from the electric field (or magnetic field) $F_3 = qE$ (2.1.7.c). From Newton's law, combining these 3 forces the generalized equation that every material follows:
$m\ddot{x} = F_{tot} = F_1 + F_2 + F_3 \implies \ddot{x} + \gamma\dot{x} + \omega_0^2 x = \frac{q}{m}E$ (2.1.7.d).
Choosing again the electric field to be $E(x) = E_0 e^{i\omega t}$, then (2.1.7.d) will change to $-mx + j\omega\gamma x + \omega_0^2 x = \frac{e}{m}E$ (2.7.e) which is the electric dipole generalized equation. Then, the electric dipole moment for N electrons per unit volume will be:

$P = Np = Nex = \dfrac{\dfrac{Ne^2}{m}E}{\omega_0^2 - \omega^2 + i\omega\gamma} = \epsilon_0\chi(\omega)E$ (2.1.7.f). After, the electric flux density $\mathbf{D} = \epsilon_0\mathbf{E} + \mathbf{P} \Longrightarrow \mathbf{D} = \epsilon_0(1 + \chi(\omega))\mathbf{E} = \epsilon(\omega)\mathbf{E}$ (2.1.7.g). Finally, equation (2.1.7.f) can be rewritten as:

$\epsilon(\omega) = \epsilon_0 + \dfrac{\dfrac{Ne^2}{m}}{\omega_0^2 - \omega^2 + i\omega\gamma}$ (2.1.7.h) and setting the plasma frequency as $\omega_p = \dfrac{Ne^2}{\epsilon_0 m}$ (2.1.7.i), it is finally done $\epsilon(\omega) = \epsilon_0 + \dfrac{\epsilon_0\omega_p^2}{\omega_0^2 - \omega^2 + i\omega\gamma}$ (2.1.8.a). It is clear that the permittivity is now frequency-depended and equation (2.1.8.a) is known as the Drude-Lorentz model for dielectric materials [42]. This can be also applied for the magnetic field to gain the permeability that now will be frequency-depended. For example, for arbitrary values of $\omega_0$, $\omega_p$ and $\gamma$ the real and imaginary part of $\epsilon(\omega)$ seems like the following (Figure 2.1.3).

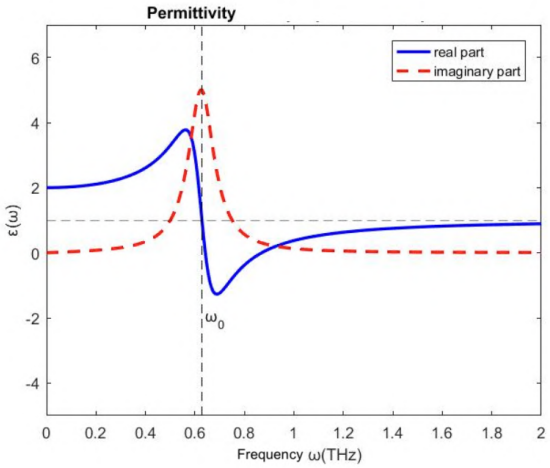


Figure 2.1.3: Real and imaginary part of electrical permittivity that follows the generalized Drude-Lorentz model for materials [43].

**⌈ All of the above equations and definitions that come to a conclusion for the frequency-depended permittivity and permeability are obtained from David J. Griffiths book "Introduction to electrodynamics" [44] ⌋**

It is proved that permittivity and permeability have strong dependence on frequency. In Figure (2.1.3) it is also clear that permittivity (and permeability accordingly) can have negative values for the real part, which is also lead to negative values of the real part of the refractive index (2.1.6.f). Although, in the case that both of these parameters are simultaneously negative, the correct value for the effective medium's refractive index is given by $n_{eff} = -\sqrt{\epsilon_r \mu_r}$ (2.1.9) [45]. This is where metamaterials comes in order to obtain these exotic properties to have both of the electric permittivity and magnetic permeability negative at the same frequency region [46].

What is difficult to find in nature are magnetic dipoles. Although, metamaterials can be designed in a way to give interaction with both electric and magnetic field, causing tunable resonances and changing the electromagnetic properties of the metamaterial. The tunability of the magnetic permeability leads to interaction of the meta-medium with the magnetic field just by controlling the design of the meta-atom which is functioning as a resonator with variable frequency [47].

Now that permittivity and permeability varies with frequency of the electromagnetic field, now $\overrightarrow{D} = \epsilon(\omega)\overrightarrow{E}$ and $\overrightarrow{B} = \mu(\omega)\overrightarrow{H}$ and equations (2.1.5.a) ,(2.1.5.b) can be rewritten as:
$\overrightarrow{\nabla} \times \overrightarrow{E} = -\mu(\omega)\dfrac{\partial \overrightarrow{H}}{\partial t}$ (2.1.5.a.i) and $\overrightarrow{\nabla} \times \overrightarrow{H} = \epsilon(\omega)\dfrac{\partial \overrightarrow{E}}{\partial t}$ (2.1.5.b.i).
From these equations there is a clear correlation with electric and magnetic field which is now frequency-depended due to the varying $\epsilon$ and $\mu$ [48]. So, in metamaterials both of the electric and magnetic field can be tuned simultaneously beyond static static applications to create exotic properties that there cannot be found in nature and engineer electromagnetic space and control propagation of waves [49].

In order to understand the electromagnetic response of metamaterials the most important parameters that have to be calculated are the Reflection (R), Transmission (T) and Absorption (A). The transmitted power is equal to the incident power multiplied by the total attenuation factor which is relevant to the properties of the medium. Then, the total absorbed power can me calculated by subtracting the total reflected power and transmitted power from the incident power: $P_a = P_I - P_R - P_T$ (2.1.10.a), where $P_I$ is the incident power

[50]. The calculation of all these parameters is based on the scattering parameters for electromagnetic waves. Since the waves are in a frequency-depended matrix form, the scattering parameters shows the corellation between the incident wave and the reflected and transmitted wave accordingly. The average power that is delivered to an area when an electromagnetic wave interacts with a medium and a part of it is absorbed is calculated by $P = \langle S \rangle A$ (2.1.10.b), where S is the Poynting vector $\overrightarrow{S} = \overrightarrow{E} \times \overrightarrow{H}$ (2.1.10.c) and A represents the area that is hit by the wave. From the last equation it is clear that the power is strongly dependent on both of electric and magnetic field [51]. Thus, power is frequency depended (through equations (2.1.5.a.i) and (2.1.5.b.i) with equations (2.1.10.c) and eventually with (2.1.10.b)) and this is how tunable resonances on metamaterials can be achieved. Changing the effective permittivity and effective permeability with frequency can change the scattering parameters and give absorption, transmission and reflection in different frequencies with narrow or wide bandwidths. These critical parameters for the architecture and operation of metamaterials are calculated by $R = \frac{P_R}{P_I}$ (2.1.10.d), $T = \frac{P_T}{P_I}$ (2.1.10.e) and $A = 1 - R - T$ (2.1.10.f) [52].

As it was mentioned before, these critical parameters for the study of metamaterials can be calculated by S-parameters $S_{11}$ and $S_{21}$. Since the study of metamaterials is occurred in a steady-state procedure one of the most well-established methods to numerically calculate the perfect matched parameters to design the meta-atoms and obtain the desirable operation of the medium is the Finite-Difference Time-Domain (FDTD) method [53]. The time/frequency domain and the capabilities of this computational method fits perfect to overcome the complexity of the artificial electromagnetic materials by solving Maxwell's equations on space and time in a wide range of frequencies make it possible to solve hierarchy and design problems and achieve the fabrication of materials that exceeds nature's materials characteristics [54]. By using FDTD, the critical S-parameters can be calculated [55] for a big variety of geometries and scaling, making the study of tunable metamaterials a straightforward process.

## 2.2 The Finite Difference Time Domain (FDTD)

The FDTD method is a computational method which allows to solve Maxwell's equations for both the electric and magnetic field. The time depended Maxwell's equations (2.1.1.a-2.1.4.b) are distincted using central-difference approximations to the space and time partial derivatives. The idea behind this came from Kane S. Yee who first introduced "Yee lattice" and describes how the electric field components in the same spacial volume are solved at a specific instant time and then the magnetic filed components are solved in the same spacial volume at the next instant time step [24].

One big benefit of FDTD method compared to other electromagnetic solvers is that it han handle arbitrary shaped structures naturally using a numerical solution to Maxwell's curl equations. The repeatable process of calculating the electric and magnetic field at each space point and time step is suitable for the complex calculations that electromagnetic metamaterials needs due to the varying permittivity and permeability.

Yee's lattice is crucial to understand the concept of the method. FDTD methods store different field components for different grid locations. This discretization is known as a Yee lattice. The vector components of E-field and H-field are represented by rectangular unit cells of a Cartesian computational grid and as a result each E-field vector component is located midway between a pair of H-field vector components and inversely [25].

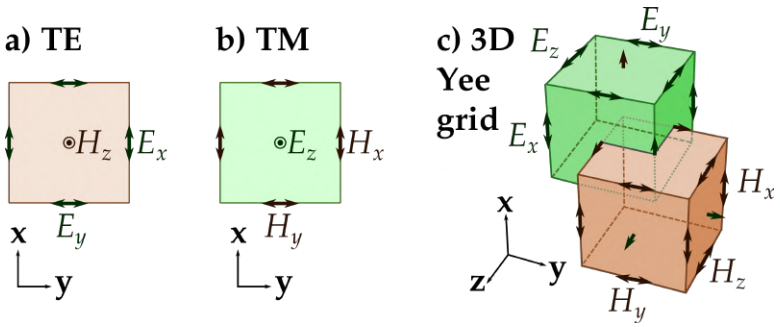


Figure 2.2.1: Illustration of FDTD Cartesian unit cell. (a),(b) For the elements of E-field and H-field. (c) Combined unit cells build Yee's grid. [Wikipedia]

As it is shown on Figure 2.2.1, the core of FDTD method is that each vector component for both of electric and magnetic fields is strongly depended on the previous and the next value of the other element. Thus, solving the complex Maxwell's equations is getting easier and straightforward since first the one element is calculated on a determinate time and then the other element of the curl product is calculated [56]. This happens in finite time and spacial steps until the whole grid is completed. The electric and magnetic fields are determined at every point in space inside this time domain method.

The freedom that FDTD method provides is precious for the study of electromagnetic metamaterials. In order to specify the geometry and the properties of the material that the electromagnetic wave will interact with only three important parameters have to specified: permittivity, permeability and conductivity [57]. Each of these parameters are showing up in discrete Maxwell's semi-differential equations as it is going to presented later.

To make a brief introduction to this computational method, a specific case will be analyzed that is commonly used and fits perfect as an introduction to FDTD method. What is highly important for the simulations and numerical analysis with FDTD are the Maxwell's equations (2.1.5.a.i) and (2.1.5.b.i). Let's first rewrite them in a more convenient form :

$$\frac{\partial \overrightarrow{H}}{\partial t} = -\frac{1}{\mu(\omega)} \overrightarrow{\nabla} \times \overrightarrow{E} \text{ (2.1.5.a.ii) and } \frac{\partial \overrightarrow{E}}{\partial t} = \frac{1}{\epsilon(\omega)} \overrightarrow{\nabla} \times \overrightarrow{H} \text{ (2.1.5.b.ii).}$$

To solve these two equations transverse-magnetic ($TM_Z$) mode is considered which includes the electromagnetic elements $H_y$, $H_x$, $E_z$. As it is going to be presented later this mode is perfect to study electromagnetic metamaterials due to the two dimensional magnetic field and one dimensional electric field only in the vertical plane. Considering these, the solutions of the equations (2.1.5.a.ii) and (2.1.5.b.ii) will be [24]:

$$\frac{\partial H_x}{\partial t} = -\frac{1}{\mu}\frac{\partial E_z}{\partial y} \text{ (2.2.1.a),}$$
$$\frac{\partial H_y}{\partial t} = \frac{1}{\mu}\frac{\partial E_z}{\partial x} \text{ (2.2.1.b),}$$
$$\frac{\partial E_z}{\partial t} = \frac{1}{\epsilon}\left(\frac{\partial H_y}{\partial x} - \frac{\partial H_x}{\partial y}\right) \text{ (2.2.1.c).}$$

The most important part now is to extrude equations (2.2.1.a-2.2.1.c) in a computational form. In 1966, K. Yee originated a set of finite-difference equations for the time-dependent Maxwell's curl equations system that is presented above. Yee's algorithm solves for both electric and magnetic fields in space and time using Maxwell's equations. The benefit is that Maxwell's equations are not solved for the electric field alone and then for the magnetic field alone using a wave equation and this lead to both electric and magnetic material's properties can be modeled in a straightforward way [58]. As it is illustrated in Figure 2.2.1, the Yee algorithm centers its $\overrightarrow{E}$ and $\overrightarrow{H}$ elements in three dimensional space so that every $\overrightarrow{E}$ element is surrounded by four circulating $\overrightarrow{H}$ components and every $\overrightarrow{H}$ element is surrounded by four circulating $\overrightarrow{E}$ components. This Yee space lattice provides central difference in nature and second-order accuracy for the curl operators that end up in the finite-difference expressions for the spacial derivatives.

In the case of two dimensional system Yee proposed a notation for space points and functions of space and time. The space point is denoted in a uniform, rectangular lattice as $(i, j) = (i\Delta x, j\Delta y)$, where i and j are the number of steps on x and y axis accordingly. $\Delta x$ and $\Delta y$ are, respectively, the lattice space increments in x,y coordinate directions and i,j are integers. Also, the contribution of time is introduced as $n\Delta t$, where n is the time steps and $\Delta t$ the time increment. Using this notation, any arbitrary function u of space and time evaluated at a discrete point in the grid and at a discrete point in time can be expressed as $u(i\Delta x, j\Delta y, n\Delta t) = u^n_{i,j}$ (2.2.2).

Yee used also centered finite-difference (central-difference) expressions for the space and time derivatives that are included in Maxwell's equations, that are both simply programmed and provide second-order accuracy in space and time increments. The partial derivative of the function u in the x-direction, at fixed time $t_n = n\Delta t$, will be:

$$\frac{\partial u(i\Delta x, j\Delta y, n\Delta t)}{\partial x} = \frac{u^n_{i+1/2,j} - u^n_{i-1/2,j}}{\Delta x} \text{ (2.2.2.a).}$$

For y-direction accordingly will become:

$$\frac{\partial u(i\Delta x, j\Delta y, n\Delta t)}{\partial y} = \frac{u^n_{i,j+1/2} - u^n_{i,j-1/2}}{\Delta y} \text{ (2.2.2.b),}$$

while for the first time partial derivative of u, evaluated at the fixed space point (i,j) will become:

$$\frac{\partial u(i\Delta x, j\Delta y, n\Delta t)}{\partial t} = \frac{u_{i,j}^{n+1/2} - u_{i,j}^{n-1/2}}{\Delta t} \text{ (2.2.2.c).}$$

**Note:** Computers cannot accept values $\pm 1/2$, as they get only integers. Thus, the $\pm 1/2$ values will become $\pm 1$.

Using this central-difference method to Maxwell's equations in the case of $TM_Z$ mode at two dimensions, (2.2.1.a-2.2.1.c) will now get the desired computational form:

$$\frac{\partial H_{x(i,j)}}{\partial t} = -\frac{1}{\mu}\frac{\partial E_{z(i,j)}}{\partial y} \implies \boxed{\frac{H_{x(i,j)}^{n+1} - H_{x(i,j)}^{n}}{\Delta t} = -\frac{1}{\mu}\frac{E_{z(i,j+1)}^{n} - E_{z(i,j)}^{n}}{\Delta y}} \text{ (2.2.3.a)}$$

$$\frac{\partial H_{y(i,j)}}{\partial t} = \frac{1}{\mu}\frac{\partial E_{z(i,j)}}{\partial x} \implies \boxed{\frac{H_{y(i,j)}^{n+1} - H_{y(i,j)}^{n}}{\Delta t} = \frac{1}{\mu}\frac{E_{z(i+1,j)}^{n} - E_{z(i,j)}^{n}}{\Delta x}} \text{ (2.2.3.b)}$$

$$\frac{\partial E_{z(i,j)}}{\partial t} = \frac{1}{\epsilon}\left(\frac{\partial H_{y(i,j)}}{\partial x} - \frac{\partial H_x(i,j)}{\partial y}\right) \implies$$

$$\boxed{\frac{E_{z(i,j)}^{n+1} - E_{z(i,j)}^{n}}{\Delta t} = \frac{1}{\epsilon}\left(\frac{H_{y(i+1,j)}^{n} - H_{y(i,j)}^{n}}{\Delta x} - \frac{H_{x(i,j+1)}^{n} - H_{x(i,j)}^{n}}{\Delta y}\right)} \text{ (2.2.3.c).}$$

In order to make further simplification, it is reasonable to assume that the increments of space are equal; $\Delta x = \Delta y$ and to import speed of light at vacuum $c_0 = 1/\sqrt{\epsilon_0 \mu_0}$ which is also connected with the propagation speed of the wave in empty space as for example in x-direction $c_0 = \dfrac{\Delta x}{\Delta t}$, when $\epsilon_r = 1$, $\mu_r = 1$. Then, the equations (2.2.3.a-2.2.3.c) will take the form:

$$H_{x(i,j)}^{n+1} = H_{x(i,j)}^{n} - \frac{1}{\mu}\frac{\Delta t}{\Delta x}\left(E_{z(i,j+1)}^{n} - E_{z(i,j)}^{n}\right) \text{ (2.2.4.a)}$$

$$H_{y(i,j)}^{n+1} = H_{y(i,j)}^{n} + \frac{1}{\mu}\frac{\Delta t}{\Delta x}\left(E_{z(i+1,j)}^{n} - E_{z(i,j)}^{n}\right) \text{ (2.2.4.b)}$$

$$E_{z(i,j)}^{n+1} = E_{z(i,j)}^{n} + \frac{1}{\epsilon}\frac{\Delta t}{\Delta x}\left(H_{y(i+1,j)}^{n} - H_{y(i,j)} - H_{y(i,j+1)}^{n} + H_{y(i,j)}^{n}\right) \implies$$

$$E_{z(i)}^{n+1} = E_{z(i)}^{n} + \frac{1}{\epsilon}\frac{\Delta t}{\Delta x}\left(H_{x(i+1)}^{n} - H_{x(i)}^{n}\right) \text{ (2.2.4.c)}$$

$$H_{x(i)}^{n+1} = H_{x(i)}^{n} + \frac{1}{\mu}\frac{\Delta t}{\Delta x}\left(E_{z(i+1)}^{n} - E_{z(i)}^{n}\right) \text{ (2.2.4.d).}$$

**⌈ All of the above equations and definitions are obtained from A. Taflove and S. C. Hagness book "Computational Electrodynamics: The finite-Difference Time-Domain method" [34] ⌋**

Equations (2.2.4.a-2.2.4.d) are in computational form and can be used in any simulation project in a straightforward manner. It is clear that the computations are strongly dependent on permittivity $\epsilon$ and permeability $\mu$. In order to obtain a smooth computational process there are some restrictions that the calculations must follow, in order for the electromagnetic wave speed not to exceed the speed of light in vacuum or the increments of spacial unit cells not to exceed the computational grid.

In computational methods there is an important factor that had to be taken in advance, the stability factor $S$. Here $S = \frac{\Delta t c_0}{\Delta x}$ (2.2.5.a). The stability condition in FDTD determines $S \leq 1$ [59]. The value $\Delta x$ is depending from the architecture of the system and how many $\Delta x$ cells there have to be in the spacial grid that they form a wavelength $\lambda$. What is commonly used is that $\Delta x = \frac{\lambda}{10}$, where $\lambda$ is calculated by $\lambda_{min} = \frac{c_0}{f_{0(max)}}$, where $f_0$ is the centered frequency of the pulse that is used in the simulation. Using Fourier transform the spectrum in frequency domain can be calculated and from there to extract the minimum wavelength that the source excites [60]. Fourier transform is used often in electromagnetic problems due to the transformation of time domain to frequency domain, and conversely, using the well-known Fourier's formula for an arbitrary function $f(t)$ with t real number and $\omega$ the frequency $\hat{f}(\omega) = \int f(x)e^{-it\omega}dt, f(t) = \frac{1}{(2\pi)^n}\int \hat{f}(\omega)e^{i\omega}d\omega$ (2.2.5.b).

The final step for the FDTD method is to convert the complex numbers of permittivity and permeability in a computational form. Since FDTD is a time domain method, $\epsilon(\omega)$ and $\mu(\omega)$ must be transformed to time domain

values. A simple example is to use a Debye medium that presents a frequency-dispersive permittivity as $\epsilon(\omega) = 1 + \frac{\sigma}{i\omega\epsilon_0}$ (2.2.6.a), with $\epsilon_r = 1$. Using the Auxilliary Differential Equation (ADE) Method [61], this dispersion will be transformed in finite differentiations. The electric flux density $\overrightarrow{D} = \epsilon(\omega)\overrightarrow{E}$ can be written as $D(\omega) = E(\omega) + \frac{\sigma}{i\omega\epsilon_0}E(\omega) \implies D(\omega) = E(\omega) + S(\omega)$ (2.2.6.b), where $S(\omega) = \frac{\sigma}{i\omega\epsilon_0}E(\omega) \implies i\omega\epsilon_0 S(\omega) = \sigma E(\omega)$. In time domain the factor $(i\omega)$ transforms to the first derivative to time: $\epsilon_0\frac{dS(t)}{dt} = \sigma E(t)$ (2.2.6.c). Now, for the calculation of the derivative the finite differential approximation will give the solution as for any given faction S the approximation gives for the first derivative $\frac{dS(t)}{dt} = \frac{S^n - S^{n-1}}{\Delta t}$ (2.2.6.d) and for the second derivative, if there is a factor of $(i\omega)^2$ in $\epsilon(\omega)$, $\mu(\omega)$ (for example in Drude-Lorentz model (2.1.8.a)), will give $\frac{d^2S(t)}{dt^2} = \frac{S^n - 2S^{n-1} + S^{n-2}}{\Delta t^2}$ (2.2.6.e), where n is the number of time step. Thus, (2.2.6.c) through (2.2.6.d) will become $\epsilon_0\frac{S^n - S^{n-1}}{\Delta t} = \sigma E^n$ and solving to S we finally take $S^n = S^{n-1} + \frac{\sigma\Delta t}{\epsilon_0}E^n$ (2.2.6.f). Finally, the electric field can be calculated from the equation $E^n = \frac{D^n - S^{n-1}}{1 + \frac{\sigma\Delta t}{\epsilon_0}}$ (2.2.6.g), $S^n = S^{n-1} + \frac{\sigma\Delta t}{\epsilon_0}E^n$ and included in equations (2.2.4.a-2.2.4.d) to solve Maxwell's equations in time domain using the FDTD method [62]. There is also the Recursive Convolution (RC) Method [63] which is based on Fourier transform to compute permittivity and permeability in time domain and Z transform method [64] which is used to transform the frequency domain to "z" domain and from there to time domain.

All of the above are just a brief introduction to the FDTD method. The applications are infinite and cannot be fully analyzed in this thesis. For the research that is done in this thesis, only commercially-available softwares were used with integrated FDTD solvers for Maxwell's equations in order to run the simulations for the electromagnetic metamaterials.

## 2.3 2-Photon polymerization (2PP)

2PP is a nonlinear phenomenon based on two-photon absorption. It enables the processing of transparent photosensitive materials, but only in those volumes where the photon density exceeds a certain threshold. Femtosecond (fs) lasers are most suitable for this purpose and their use enable to fabricate true 3D geometries when the laser beam is guided specifically through the resist [65]. This absorption is based on non-linear optical effects. In non-linear optics the polarization $\overrightarrow{P}$ of a material and the electric field $\overrightarrow{E}$ of the electromagnetic wave are not linearly related [66]. In linear optics when a field is applied to a material the polarization is linearly related to the field as $\overrightarrow{P} = \chi_e \epsilon_0 \overrightarrow{E}$ (2.3.1.a), where $\chi_e$ is the optical susceptibility and $\epsilon_0$ the vacuum permittivity. In non-linear phenomena the polarization is depended from higher-order field terms as $\overrightarrow{P} = \epsilon_0(\chi_e^1 \overrightarrow{E} + \chi_e^2 \overrightarrow{E}^2 + \chi_e^3 \overrightarrow{E}^3 + ...)$ (2.3.1.b). The first term is related to the linear effects while higher-order terms are introducing the non-linear effects [67]. These higher-order terms are responsible for the number of photons that are absorbed when an electromagnetic field is applied to a photosensitive material. The probability of n-photon absorption in general is proportional to the $n^{th}$ power of the photon flux density which is related to the electric field that it is applied (and subsequently to the polarization through (2.3.1.b)). Thus, high photon intensities are required to initialize the process. The basic idea behind this is that an atom of an any given material can absorb two or more photons simultaneously allowing electron transition to higher energy states.

Theory of 2 photon absorption (2PA) was first developed by M. Göppert-Mayer in 1931 [68] and was experimentally proved after the inventions of lasers, due to the high intensity that is mandatory to initialize the process. There are two different mechanisms of 2PA, sequential and simultaneous two-photon excitation [69]. The first mechanism relies on the existence of a real intermediate state, where an excited electron is transferred to a higher energy bound state by absorbing a photon and gaining all its energy. As for the process, it does not require coherent light and can be considered as two consequent single photon absorption process. On the other hand, the second mechanism is about simultaneous two-photon excitation which leads to a simultaneous two photons absorption. In this process the intermediate state is virtual that is not created from the absorption of energy of a photon, but from the interaction of the absorption with the first photon. This can

happen only if another photon arrives within the virtual state lifetime and this can be occur with high intensities that are provided by a tightly focused femtosecond laser beam [27].

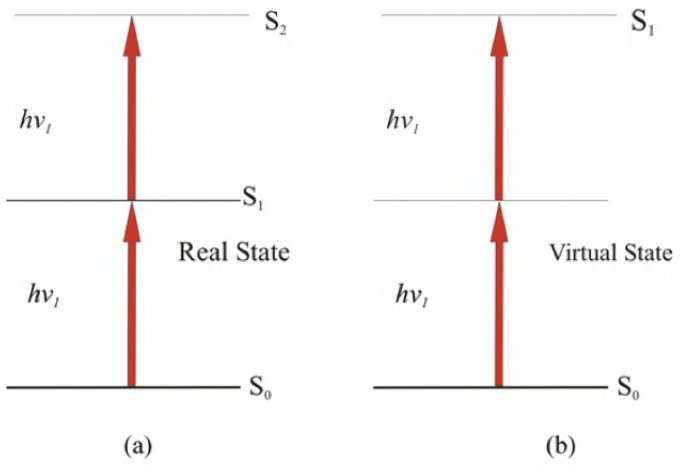


Figure 2.3.1: Schematic presentation of 2PA energy diagram, (a) sequential two photon excitation, (b) simultaneous two-photon excitation. Obtained from [27].

On the sequential two-photon excitation (Figure 2.3.1.a) the presence of the intermediate state $S_1$ implies that the material absorbs in this specific wavelength. On the contrary, in simultaneous two-photon excitation (Figure 2.3.1.b) since there is no intermediate state with a lifetime of $10^{-9} - 10^{-4}$ sec, the material is transparent to this wavelength. This can happen only if the other photon arrives within the virtual state lifetime which is approximately $10^{-15}$ sec [70]. In order to initialize the process femtosecond lasers are commonly used because of the ability to produce ultrahigh peak power (the high intensity that is needed), but also very short pulse width of approximately 100 femtoseconds ($10^{-15}$ sec) or less (the virtual state lifetime condition that is mandatory to be satisfied in order to get the second photon excitation). These lasers are also commonly used in 2PP fabrication process because of their central wavelength (approximately 800nm) which is close to half of the wavelength of the polymerization (in order to excite the second photon) and the initialization of the 3D micro-printing technique can straightforwardly occur [71].

In the 2PP technology, polymerization occurs in the focus volume inside the material where the radiation intensity is enough to initialize two-photon absorption. This focus volume is defined by the square dependence of the intensity of the pulse, $I(r_0) = I_0 e^{\frac{-2r_0^2}{\omega_0^2}}$ (2.3.3) for a Gaussian-like pulse where $r_0$ is the radius of the beam, $I_0$ the intensity and $\omega_0$ the radius of the focus beam spot. The polymerization volume is only a part of the total focus volume which is called voxel. Voxel is a complex parameter which is depending on the transmitted power of the beam, the scanning speed of the process, the Numerical Aperture (N.A.) of the objective lens and other minor parameters [72]. If there is a linear response of the material to the light intensity then there is a constant number of photons that are excited at every cross-section of the focus spot and there is one photon absorption. Otherwise, if the response is proportional to the square of intensity then 2PA can occur, given the high intensity that is formed at the center of the focus spot, inside the voxel.

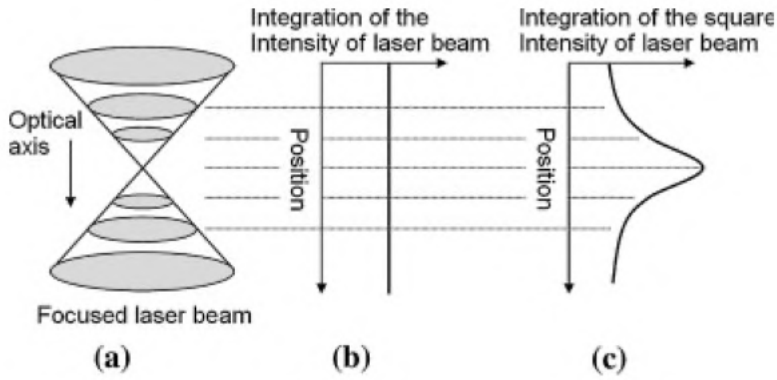


Figure 2.3.2: Schematic presentation of the focus point and intensity of the beam,(a) schematic diagram of laser focus point, (b) total single-photon absorption per transverse plane, (c) total two-photon absorption per transverse plane, which is calculated by integrating the square intensity over the plane with respect to the optical axis. Reproduced from [73].

As illustrated in Figure 2.3.2.c, if the material response is proportional to the square of the photon intensity, the integrated material response is

highly enhanced in the focus spot. In this spot the 2PA takes place and can be initialized if the intensity is above the polymerization threshold. With large values of intensity the transition rate is extremely small in general, so a very high spatial resolution can be obtained inside the voxel, enhancing 2PP ability to fabricate ultrahigh-resolution 3D micro- and nano- structures. The difference of the focal point is presented below in Figure 2.3.3.

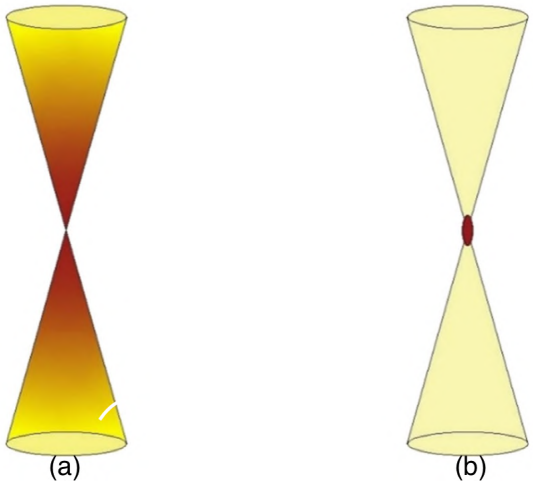


Figure 2.3.3: Schematic picture comparing the excitation volume of one-photon excitation (a) and two-photon excitation (b). In 2PP, regions outside the laser focus are less likely to exceed the polymerization threshold of the photoresist. This phenomenon allows the fabrication of complex 3D structures. Reproduced from [74].

From a chemical aspect there are three conditions that have to be satisfied in order to fabricate via 2PP; initiation, propagation, termination [75]. In order to initiate the process of two photon polymerization, a high intensity laser beam have to focus inside the volume of a photosensitive polymer, as it is presented on Figure 2.3.3. The photo-polymerization realizes via chain reactions that can reach thousands in value (Figure 2.3.4). The photoinitiator that is used to enhance two photon activation is excited by the simultaneous 2PA, resulting the generation of free radicals (initiation step). The second step is that the free radical reacts with a monomer molecule to form monomer radicals that participate in the chain reaction (propagation

step). The final step is when two radicals meet each other and the chain reaction is terminated, the center of growth is deactivated and the final molecule is formed (termination step) [76]. This formation of polymer chains cause a phase transition for specific photo-sensitive materials (resins) that under certain circumstances can go under phase transition, from sol-gel to solid via exposure only at a laser beam with high intensity and specific wavelength [27].

As it was discussed, 2-Photon polymerization process follows the same procedure like any other polymerization process. The difference is that the initiation of the process and the chain reaction is happening by exposing the material under a high intensity laser focused beam and not under specific temperature. This can lead to the fabrication of arbitrary 3D geometries with freedom of move in all the three axis. Also, the solidification of the sol gel makes easy the removal of the excess un-polymerized material, which leads to high resolution structures.

$$\text{Initiation} \qquad I \xrightarrow{hv,hv} I^* \longrightarrow R^\bullet \qquad \text{(a)}$$

$$\text{Propagation} \qquad R^\bullet + M \longrightarrow RM^\bullet \xrightarrow{M} RMM \cdots \longrightarrow RM_n^\bullet \qquad \text{(b)}$$

$$\text{Termination} \qquad RM_n^\bullet + RM_m^\bullet \longrightarrow RM_{n+m}R. \qquad \text{(c)}$$

Figure 2.3.3: Presentation of the chain reaction steps to form a polymerized molecule, (a) initiation step, (b) propagation step, (c) termination step, where v is the photon frequency in the two photon excitation beam, I the initiator, R the free radical and M the monomer, $I^*, R^*$ represents the excited state of the initiator and the radical respectively. Reproduced from [27].

3D printing by 2PP offers high versatility due to the varying materials that can be processed. Although, it is very important to form and develop the correct initiators to begin the procedure of polymerization and then the formation of polymerized material. As it is going to present below, the variety of materials that can be used is large and this gives the benefit that the polymerized materials can have varying characteristics such as varying refractive

index [77], Poisson's ratio [78], or even with post-process chemical procedures whether the material is going to exhibit dielectric or metallic properties[79]. In addition, as it was mentioned above it is a mask-less procedure that combined with CAD designing results in high resolution 3D structures. Last but not least, in the process no harsh chemicals are used and fabricated structures are compatible to be further processed with conventional deposition processes to result in extraordinary tunable properties, while the quality of the final structure and the shape can last for years maintaining their properties.

# 3 Materials and 2PP setup

## 3.1 Materials

In order to achieve two photon absorption and subsequently two photon polymerization there are many materials that can be processed. The mandatory requirements that must be fulfilled is to have a high absorption at half the wavelength is used for processing the material and high transparency of the material at the specific laser wavelength. Organic-inorganic hybrid photosensitive materials synthesized by sol-gel method [80] are commonly used for the fabrication of high resolution micro structures using 2PP technique.

Using organic-inorganic components gives the benefit that both organic and inorganic structural elements co-exist in atomic or nanoscale dimensions. This give the opportunity to gain the combines properties of these two different categories. The inorganic part is responsible for the mechanical and thermal stability of the hybrid, affects the refractive index and induce electrochemical properties. Further, the organic part tunes the mechanical properties and can give individual chemical, physical or biological properties. The most widely used hybrid materials for 2PP printing technology are $ORMOCER$®, $OrmoComp$®(both provided by Microresist Technologies) and $SZ2080^{\text{TM}}$ (provided by IESL-FORTH). In the present thesis $SZ2080^{\text{TM}}$ is used in all the experiments.

The Sol-gel method is based on two different mechanisms: Hydrolysis and Condensation [27]. Hydrolysis is the reaction of certain molecules with water which leads to decomposition of the molecules under the presence of an acid or basic solvent, and condensation is occurs when these separated atoms change their phase from gas to liquid [81]. The inorganic part is originated from metallic alkoxides, which through these two crucial mechanisms form an inorganic network inside the hybrid material. Also, the monomer units that are extracted from the organic part, form photopolymerizable elements that are attached to the inorganic network. After the creation of the sol-gel, adding appropriate photoinitiators (PIs), which are consisting of free radicals that when they are interacting with photons (laser beam) they are triggering the two photon polymerization process, gives to the hybrid material an extra linear and non-linear photosensitive behaviour. When these molecules are treated with specific wavelength radiation they initiating polymerization of

the organic part and subsequently the formation of organic-inorganic network that is mandatory in order to achieve the two photon polymerization [27].

Below there is a schematic chemical presentation of hydrolysis and condensation. Once the hydrolysis reaction is initiated, both mechanisms are occur simultaneously. This is the initiation to form the gel-like material that afterwards is developed to present photosensitive characteristics. Usually, the alkoxide precursor is Si, Ti, Zr, etc., and the acid and basic solvents are for example hydrogen chloride (HCL) and ammonia ($NH_3$), respectively [82].

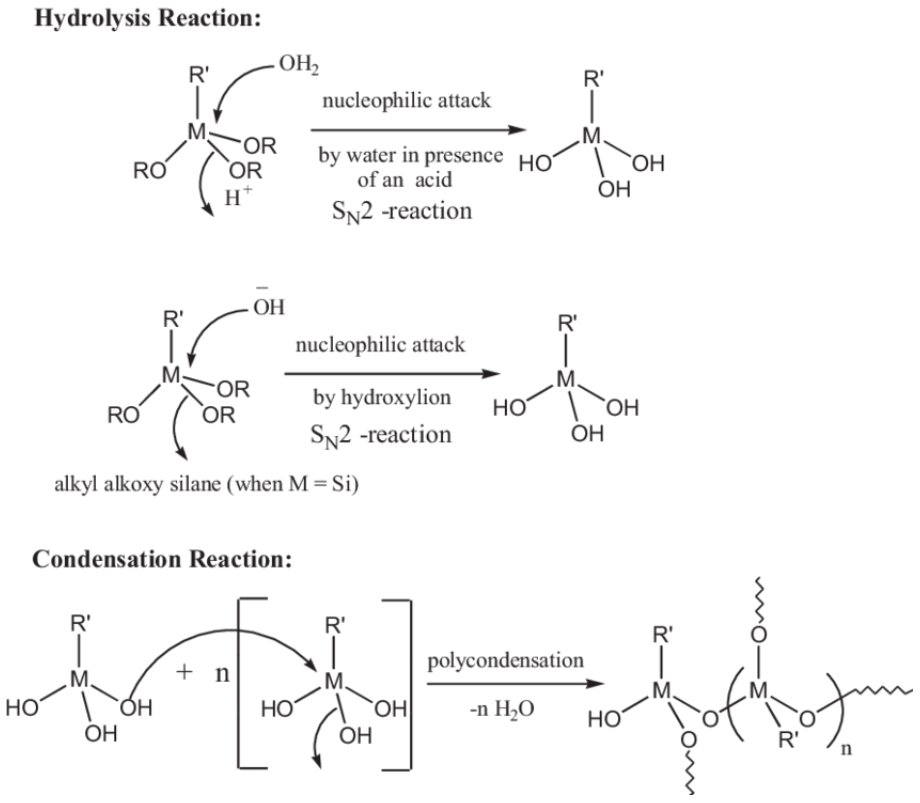


Figure 3.1.1: Formation of sol-gel due to hydrolysis and condensation polymerization reactions, under the presence of Si for alkoxide and $SN_2$ for acid. Reproduced from [83].

Using sol-gel materials comes with a great advantage to additive manufacturing of micro structures using two photon polymerization technique. The variety of materials that can be used to form the sol-gel gives the ability to tune the properties of the polymerized material. Depending on the alkoxide and the condensation's chemical element, the final polymerized material can have different characteristics [84] regarding to the refractive index, porosity, mechanical properties, optical properties etc. [85]. In addition, the excess un-polymerized material can be easily removed using organic and inorganic developers.

To sum up, the polymerized material can generally formed through a 4-step procedure [27].

1. Precursors and monomers are mixed with water solution and through hydrolysis and condensation reactions they form a porous interconnected cluster structure.

2. The gelation of the material is done when the solvents are removed by heating in low temperature or the material is stored in vacuum conditions.

3. The presence of the photoinitiator triggers the polymerization process only in the area that the laser beam is focusing and the photoinduced radicals will polymerize the sol-gel.

4. Finally, the sol-gel material is immersed in proper solvent and the excess un-polymerized material will be removed, leaving only the polymerized structure.

## 3.2 Synthesis of photosensitive hybrid materials

The novel active 3D printable hybrid material that is used in this thesis is $SZ2080^{TM}$ [86], provided by IESL-FORTH. Basic components of the material are zirconium (Zr) and silicon (Si). For the organic part 3-(Trimethoxysilyl) propyl methacrylate (MAPTMS) and 2- (Dimethylamino)ethyl methacrylate (DMAEMA) are used, where the DMAEMA component is the organic photopolymerizable monomer. For the inorganic part Zirconium n-propoxide (ZPO) was used. In combination with the alkoxysilane groups of MAPTMS, that can undergo hydrolysis and condensation, served as the inorganic network forming moieties. ZPO is used to provide mechanical stability to the polymerized material.

The organic photosensitive part have a weak absorption from IR to UV and a low two photon absorption cross-section. Thus, even though the material is transparent at the laser central wavelength at 800nm, the two photon absorption is weak. Adding a photoinitiator that absorbs strongly at lower wavelengths and triggers the two photon absorption mechanism, the initial step of two photon polymerization, is suggested. At the thesis the photoinitiator 4,4'- Bis(diethylamino) benzophenone (Bis) is used, which absorbs strongly at 400nm but weaker at 800nm [87]. Bis makes two photon polymerization more efficient in lower energy values and does not affect at all the organic-inorganic network of the hybrid materials. Structural formula of the 4 basic materials that are used for the synthesis of the novel hybrid SZ2080 is presented in Figure 3.2.1.

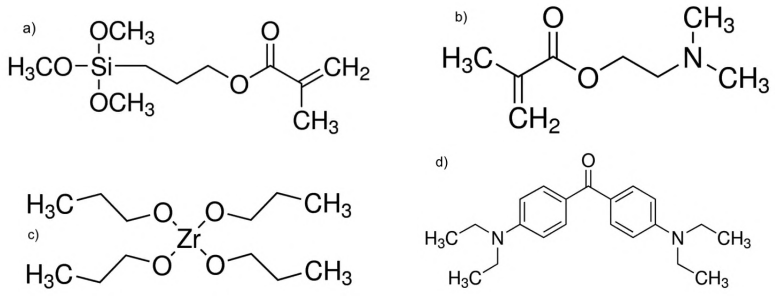


Figure 3.2.1: Structural formula of a) MAPTMS (organic monomer), b) DMAEMA (photopolymerizable material), c) ZPO (inorganic component), d) Bis (photoinitiator) [SigmaAldrich]

Synthesis of the hybrid material is a complex process where a variety of reactions take place. First, MAPTMS and 0.1M HCL (diluted in water) at 10:1 ratio are combined in a flask and stirred for 15 minutes until the solution become homogeneous and completely transparent. Hydrolysis takes place in the solution immediately and after the stirring the hydrolyisis of the alkoxysilane groups is completed. The second solution is ZPO with DMAEMA. ZPO is highly reactive with moisture so it is diluted in 70% w/w concentration of propanol. DMAEMA is slowly added to ZPO at a molar ratio 7:3, where DMAEMA serves as a carrier for ZPO and no reaction takes place. DMAEMA is responsible for the photosensitive characteristic of the material and provides also metal-binding moieties that are crucial for the metallization of the material with a post-treatment technique that will be analyzed later in this thesis. Again, the solution is stirred for 15 minutes to become homogeneous.

After the two components have homogeneously disolved, the partially hydrolyzed MAPTMS is slowly added to the zirconate complex in a droplet-by-droplet approach. In this case, the organic-inorganic network is formed due to the Si atoms that are attached to the polymer matrix. The solution is stirred for 15 more minutes until it becomes transparent. Finally, the photoinitiator, Bis, is added to the final solution at 1% w/w concentration. The final solution is stirred for 15 minutes until all of the components are disolved. Afterwards, the final solution is filtered using 0.22 $\mu m$ syringe filters [88]. The material then is sealed and stored in a cool environment to protect it from heat, light and moisture and make it last longer. A simplified scheme of the 4-steps procedure is presented in Figure 3.2.2.

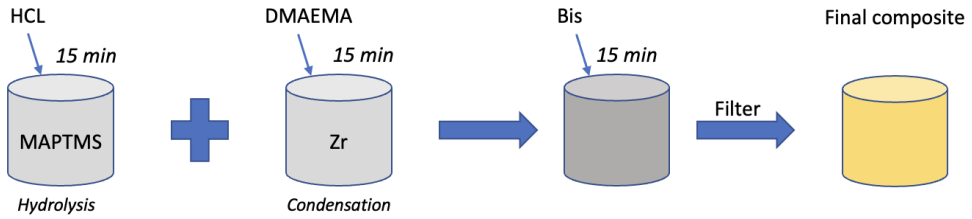


Figure 3.2.2: Schematic presentation of SZ2080 synthesis process.

### 3.2.1 Sample treatment

There is a variety of substrates that are used in two photon polymerization technology, depending on the application. In this thesis, square microscope pure glass ($2x2$ $cm^2$, 100 $\mu$m thickness) and silicon substrates ($1x1$ $cm^2$, 1 mm thickness) are going to be used. Further details about the performance of these substrates in low THz regime will be analyzed later. The samples must be prepared with a post-process treatment in order to be ready for use and the material after the printing process to attach to the surface of the substrate and not be washed. The silanization protocol is consisting of three steps. Firstly, the substrate is being immersed in ethanol for 1 hour in the ultrasound machine in order to clean the surface from dirt and other organic components that they may exist. Secondly, the substrate is being immersed in a solution of MAPTMS and dichloromethane at volume ratio 80:1 for 4 hours at the ultrasound machine or overnight. This cause the formation of a MAPTMS layer on the substrate that has free bonds and the polymerized material can attach there. On the final step, the substrates are being immersed in ethanol and can be stored. The protocol for the silanization is the same for any substrate.

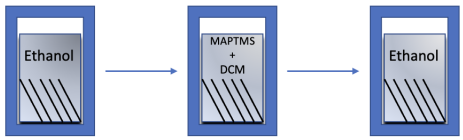


Figure 3.2.1.1: Schematic presentation of silanization protocol.

For the preparation of the sample, first the substrate must be dried using an air pistol. Secondly, a drop of material is placed on the substrate using a pipette. Then the sample must be placed on a hot plate for at least 1 hour at 60 $^oC$, or for at least 24 hours under low vacuum conditions. This has a result the formation of the sol-gel material that the excessive solvents have been evaporated. The samples can be stored in a low vacuum chamber for about 20-30 days, until the DMAEMA component spoils and it is no more photopolymerizable [86].

Figure 3.2.1.2: Schematic presentation of the droplet-like sample formation on the substrate, before and after the solvents have been evaporated.

Finally, to get the polymerized structure a post-process development must be done. After the printing process, the sample is developed in a solution of 4-methyl-2-pentanone for at least 15 minutes and then rinsed in 2-propanol, in order to remove the un-polymerized material. Then the sample must be let it to dry [89].

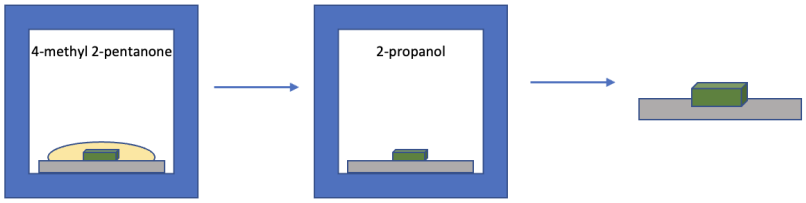


Figure 3.2.1.3: Schematic of the final development process and final result.

## 3.3 The Two Photon Polymerization setup

The irradiation source for the 2PP process is a Femto-second Fiber Laser (FemtoFiber pro NIR, Toptica Photonics AG emitting at 780 nm with pulse duration 150 fs, average output power 500 mW and repetition rate 80 MHz) [84]. The beam splitter divides the beam at ratio 70:30 into two different setups which are using different principle for guiding the beam. The setup used more in the present thesis uses a galvo-scanner to deflect the beam in the specific geometry of each layer which allows the fabrication of large areas in small time. The other setup uses only the movement of the stage to print the geometry of each layer and allows the fabrication of ultra-high resolution structures with spatial resolution of a few nm. The beam is passing through an acousto-optic shutter which which operates as a high frequency Q switch blocking and allowing the beam to pass through the crystal, while rotating the crystal can change the power of the laser beam using electric signals [90].

Then the beam is inserted in the Galvo scanner that it consists of galvanometric mirrors that scans the laser beam on xy plane during the fabrication process. Increasing the movement speed of the mirrors has a result to increased scanning speed and reduced fabrication time. Then, the beam passes through a telescopic lens that expands the beam to illuminate the full back aperture of the microscope objective lens and achieve optimal focusing. After, the beam is reflected on a dichroic mirror that has a CCD camera mounted behind in order to observe the fabrication process and find the interface where the beam focuses and fabrication should begin. The rest of the laser beam is focusing in a microscope objective lens that magnifies the laser beam with a high numerical aperture (NA) which varies depending on the lens and focus it at the focal point onto the sample. Higher NA results in higher resolution and working distance, while the field of view is determined by the magnification of the microscope lens. The sample is placed on a high-precision three-axis linear translation stage with accuracy of 100 nm. Since it is a layer by layer printing technique correlated to the CAD design, Galvo setup structures with 100 nm layer distance are able to be fabricated. The xy movement of the stage provides the ability to fabricate large areas through stiching process, a very useful tool for the fabrication of metamaterials and metasurfaces. Finally, a green LED is placed under the stage in order to pass through the transparent substrate and observe the fluorescence of the material through the CCD camera as long as the fabrication procedure.

The fabrication process begins with designing the structure in CAD software. Then the stl file is uploaded in a custom-made software that controls the whole procedure of printing, developed in FORTH. After, the beam has to be aligned in the optical path to pass through the microscope objective lens completely vertically. If it is not aligned then the layer by layer printing will be done in an angle, resulting in low-quality structures. After the alignment, the sample is placed on the stage and the interface is spotted using the photosensitivity of the material. When the beam focus inside a volume of the material, then it starts to produce bright spots due to the polymerization. This can be quite challenging when the fabrication has to be done on Si substrates, since they are not transparent at visible spectrum and CCD cameras cannot detect the brightness of the volume there. If the interface is inside the material, then in the development process the polymerized material will flow of the substrate. Then the ultimate variables of scanning speed and power of the laser beam have to be adjusted in order to start the polymerization process and write, but not destroy the material due to high power. After the printing is completed, the development protocol as it was discussed above is followed to get the final structure. A simplified design of the optical path is presented below in Figure 3.3.1.

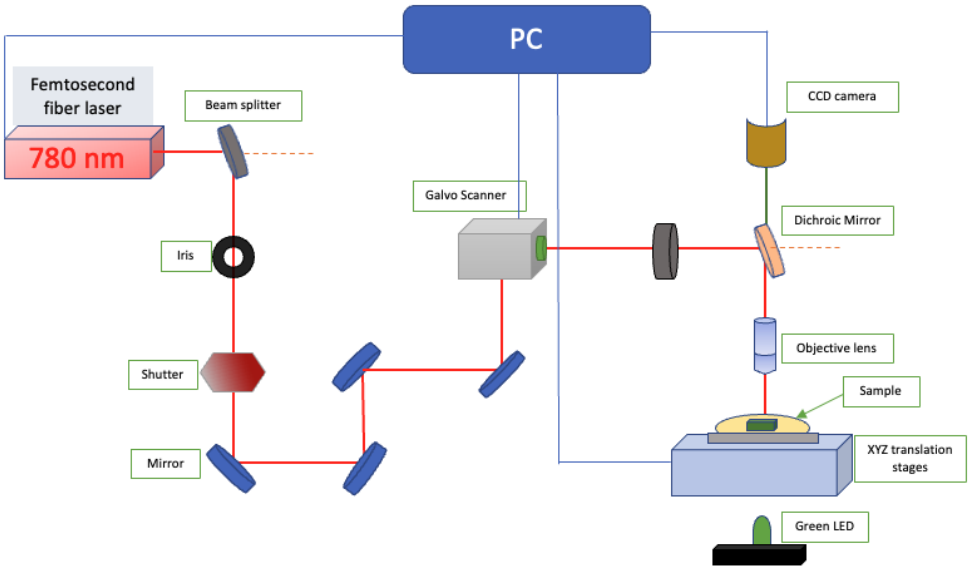


Figure 3.2.3: Two Photon Polymerization -Galvo scanner- setup.

## 3.4 Scanning Electron Microscope (SEM) as a handy tool for 2PP

2PP is a true 3D printing technique that provides high resolution structures at micro- and nanoscale. Observation of the fabricated structures is mandatory in order to obtain optimal results. A common imaging tool that is used for this situation is SEM, which produces images of a sample by scanning the surface with a focused beam of electrons instead of light compared to conventional optical microscopes. Most important function of SEM is the high-magnification and high-resolution imaging of surface texture and structure [91] allowing the detailed observation of the fabricated geometries.

Basic operational principle is the detection of secondary electrons that are scattered due to the topology of the structure, resulting in different intensities depending on the spot the electron beam is focusing. The electrons are accelerating through an electron gun, then pass through a group of converging and diverging lenses that magnify the electron beam and finally reach the target [92]. In order to be scattered, the sample must be conductive. Thus, in dielectric materials a pre-process is required by covering the sample with a thin layer of conductive material using a "sputter coater" machine. In metallodielectric materials this process is can be omitted. The scattered electrons are passing through a detector which analyse the intensity of the incoming electrons, providing the high-magnification image. In Figure 3.4.1 a scheme of SEM setup is presented, as well as an example of high-magnification image of a fabricated structure with different scaling using 2PP.

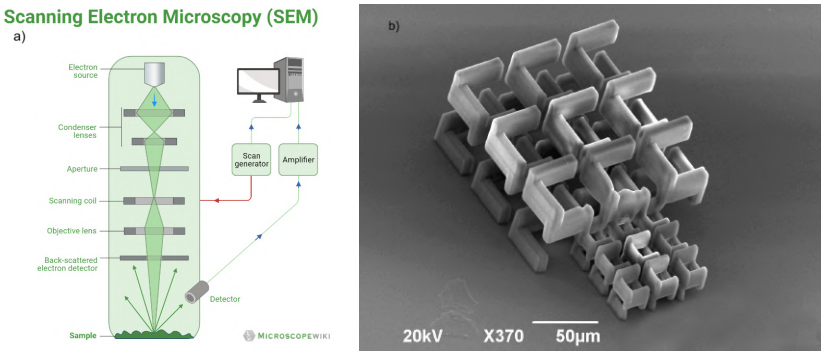


Figure 3.4.1: a) SEM setup, obtained from [microscopewiki], b) SEM image with high-magnification.

# 4 Development and fabrication of electromagnetic (EM) metamaterials combining FDTD and 2PP

## 4.1 FDTD setup for simulating THz metamaterials

All the simulations are performed using a high performance 3D EM analysis software package for designing, analyzing and optimizing electromagnetic (EM) components and systems, CST Studio Suite (CST). The software uses FDTD method to solve Maxwell's equation for both electric and magnetic field, performing complex calculations for arbitrary and complex 3D geometries for ultrahigh-frequencies. Everything can be set in order to reach as close as possible to real experiment's conditions by controlling the electromagnetic interference that is present in measurements. The variety of materials that can be used as well as the freedom to import custom made material's properties makes it makes it perfect for thoroughly study of electromagnetic metamaterials.

The setup of the simulation remains the same for the analysis. What changes in every experiment is the geometry of the meta-atom and the material that is made of, to exploit the total benefits of metamaterial's technology. Different materials give different scattering parameters through the interaction of electromagnetic waves and matter. The important part is to import a source that will generate the electromagnetic wave and a detector which will make possible the extraction of the spectral characteristics at the desirable frequency region, calculating the scattering parameters of the total system. Simulations are also mandatory to get the optimum design of the THz metamaterial by modifying the structural components of the meta-atom to give the ultimate electromagnetic response.

In order to determine the size of the unit cell for the simulations, a virtual box is created with vacuum's material properties (permittivity $\epsilon_{eff} = 1$, permeability $\mu_{eff} = 1$ and propagation speed $u = c_0$). The dimensions of the box are made so the x-y length defines the size of the unit cell and the height z the vertical size of the structure combined with a free space that the electromagnetic wave will propagate.

For the determination of the simulation's conditions, first the field has to be defined. A field is imported as an exciting port at the top surface of the box ($Z_{max}$) and can generate either Transverse Electric (TE) either Transverse Magnetic (TM) modes of oscillation. The region of frequencies that must be covered is set to be from 0.5 THz to 7 THz frequencies, providing a ps ($10^{-12} sec$) pulse. The (0,0) mode is selected in both of TE and TM case. Second, two ports are also added to the system. The first at the top surface of the box $Z_{max}$ and the second at the bottom surface of the box $Z_{min}$. These two analyzing ports are operating as detectors, measuring the incident and transmitted power of the electromagnetic wave after been scattered from the meta-atom that is designed inside the box. From these values, the S-parameters are calculated after.

Afterwards, the boundary conditions of the system are included. Perfect Matched Layer (PML) boundary conditions provides the tool to simulate an infinite array of unit cells without designing individual unit cells. This of course is not coming in agreement with the measurements, but since every measuring system has a working field it is correct to consider that the simulation approaches the experiment. On x-y plane, unit cell boundaries conditions are selected in order to provide the infinite array. At z direction, the boundaries $Z_{min}$, $Z_{max}$ are selected as open and floquet boundaries are set in order to have an infinite extension of the external medium in the vertical direction and as a result an infinite propagation of the electromagnetic wave without external interactions (commonly used for dispersion curves). For the generated pulse it is considered that the angle of the incident wave is at 0 degrees, thus it is propagating absolutely vertical to the medium.

After, the discrete units $\Delta x$, $\Delta y$ and $\Delta z$ are set equal to $0,01\ \mu m$. In order to get more precise results, adaptive fine mesh settings are also set. The maximum quality of mesh reach the value of 1, while 4 computational cells per wavelength are chosen. For the external box made of "vacuum", a triagonal mesh is done with maximum and minimum element size equal to 1 and $0,05 \mu m$ accordingly. For the geometry a free-tetrahedral mesh with maximum and minimum element size of 10 and $0,01\ \mu m$ is selected. This provides that the calculations will be more accurate and the final results will be as close as to the experiment's.

From the modeling section, the geometry is designed as desired. Then the material of the structure can be defined through the material's library or by defining the values for $\epsilon_{eff}$, $\mu_{eff}$ and $\sigma$ of the selected material at these frequencies. The geometry and the material are the variables in the present thesis, everything else is set as discussed above. The simulation is ready to run. After this, the S-parameters are presented through calculations of the output signal spectrum and input signal spectrum. From the S-parameters, a linear and a dB graph are visualised. The dB unit graph is common in measuring reflection, transmission etc. as it expresses the ratio of a power or root-power quantities on a logarithmic scale.

The quantities of interest are the reflection and transmission for the study of electromagnetic metamaterials. Depending on the electromagnetic mode of the source that was chosen, there are curves with different S-parameters. For the TE(0,0) mode, reflection is presented by $S_{Zmax}(1), Z_{max}(1)$ and transmission by $S_{Zmin}(1), Z_{max}(1)$. Accordingly, for the TM(0,0) mode, reflection is extracted from $S_{Zmax}(2), Z_{max}(2)$ and transmission from $S_{Zmin}(2), Z_{max}(2)$. The number 1 and 2 refers to the detecting port that was operating to measure these values [93]. Finally, the absorption spectrum can be obtained from the post-process sector using the equation 2.1.10.f ; $A = 1-R-T$. Depending on the resonances the simulation can run multiple times with varying sizes of the geometry's structural elements until the optimal results are achieved. Ports of the simulation setup is presented in Figure 4.1.1.

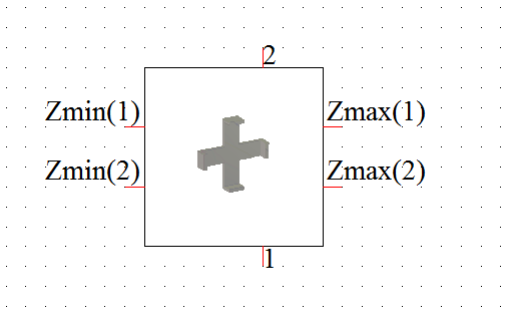


Figure 4.1.1: Scheme of S-parameters ports. In the middle there is the CAD geometry, while on top and bottom are the excitation port and detection port accordingly. Depending on the polarization of incident wave, S-parameters for TE (port 1) and TM (port 2) modes can be calculated.

### 4.1.1 Simulations of cross-based SRR

One of the most well-established designs for the study of electromagnetic metamaterials are SRR [6]. Split ring resonators are based on the fact that the deformations in their architecture provides fertile conditions, such as magnetic response, to create metamaterials that can operate from microwave to NIR frequencies. SRR's geometries can vary depending on the frequency that they operate. Most of the SRR are designed as circular SRR [94] or rectangular SRR [95] that they have a hole in the geometry. The consept of metamaterial in these structures comes from the fact that they show a symmetry-asymmetry pattern which can lead to electromagnetic interference using a repeated complex of unit cells. The sub-wavelength periodicity that is easily scaled, makes this SRR designs perfect for applications.

Another design that seems to operate in the same manner as the classic SRR, is the cross-shaped SRR that it is shown to enhance perfect absorption at low THz frequencies [96]. A variation of the cross-shaped metamaterial was done in order to obtain a dual band perfect reflection and transmission. The idea behind the design was to create an "imperfection" at the edge of every side of the cross to enhance the interference of the THz field and create a strong reflection-transmission behaviour. The designs and simulations were done in collaboration with Ioannis Sakellariou, Bachelor student at Physics Department at University of Crete.

The first CAD design that indicates the existence of at least one resonance in low THz frequencies is the above with dimensions a=25 $\mu m$, b=112 $\mu m$, w=5 $\mu m$, h=25 $\mu m$ and periodicity 130 $\mu m$.

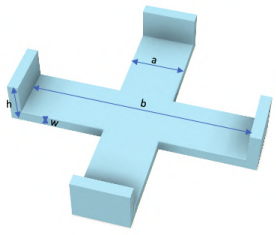


Figure 4.1.1.1: CAD design of symmetric cross-shaped SRR metamaterial.

In order to obtain the electromagnetic response of this metamaterial at low THz frequencies, an infinite array of the unit cells is considered. The material that was chosen is PEC (Perfect Electric Conductor) operating as perfect dielectric such metallic materials. For the source, the frequency ranges from 0.5-3.5 THz, which generates a ps pulse. The excitation signal of the source in time domain is presented in Figure 4.1.1.2.

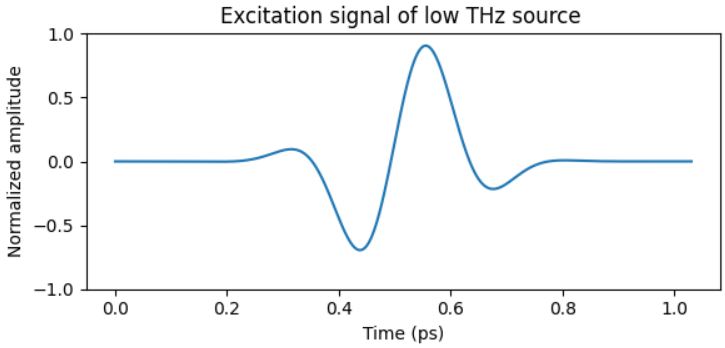


Figure 4.1.1.2: Excitation signal of the source for low THz (0.5-3.5 THz).

The results of the simulations for reflection and transmission for the cross-shaped metamaterial are presented in Figure 4.1.1.3, for the TM(0,0) mode.

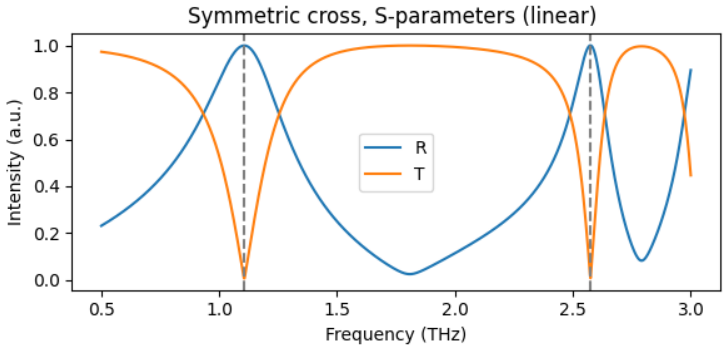


Figure 4.1.1.3: Simulation results of Reflection (R) and Transmission (T) for cross-shaped metamaterial, TM(0,0) mode.

A dual-band resonance is showing up at 1.1 and 2.6 THz respectively. A heat-map design of the absolute value of current that circulates the geometry originating from the interaction between the electromagnetic field and the medium is shown below.

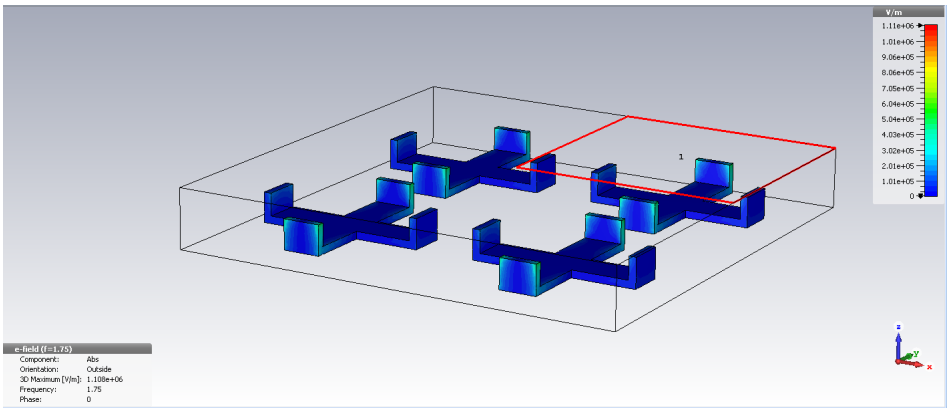


Figure 4.1.1.4: Surface currents induced in cross-shaped metamaterial by 1.75 THz plane wave.

The fabricated array of the design, using 2PP is also introduced in Figure 4.1.1.5 (using a 40x objective lens, with N.A. 0.95), exploiting the resolution of the printing technique.

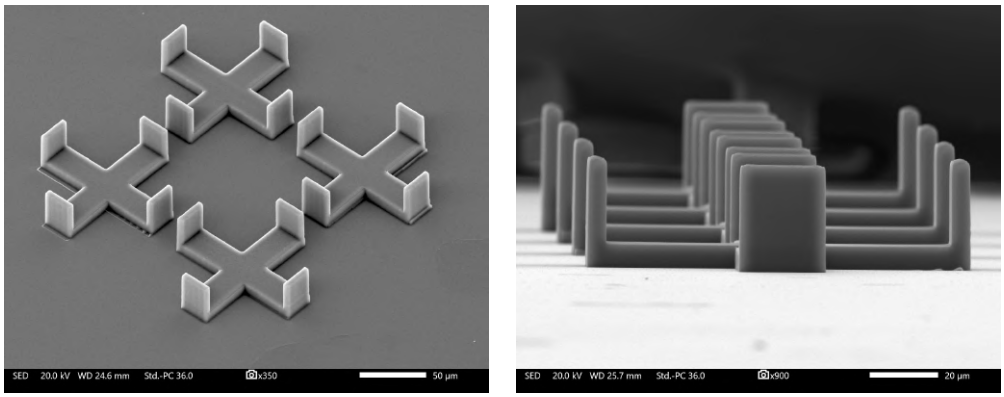


Figure 4.1.1.5: Sem images of the cross-shaped metamaterial.

Although the material is dielectric, it is obvious from Figure 4.1.1.3 and 4.1.1.4 that the architecture of the cross is suitable for the generation of a low THz electromagnetic metamaterial that enables -theoretically- zero absorption due to symmetrical features. At the resonances, there is quasi-perfect reflection with zero transmission, resulting in total absorption with significantly low energy losses (calculated from equation 2.1.10.f).

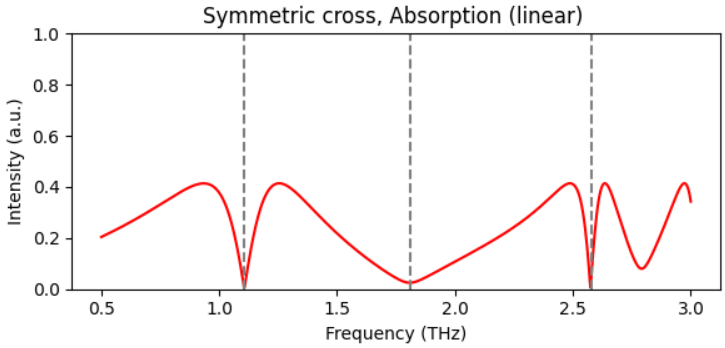


Figure 4.1.1.5: Calculated results of Absorption spectra.

From the absorption spectrum also on Figure 4.1.1.5, the medium can turn completely transparent with total transmission and zero absorption in a wide frequency band around 1.8 THz. A sensor for low THz frequencies could be based on a design like this with these specific electromagnetic response. Flow of the current that is generated from the interaction of the electromagnetic field with the components of the structure creates a magnetic response that is capable to manipulate specific wavelengths. As a result, a transparency can be achieved in order to create a low THz sensor to construct a THz modulator in a narrow frequency band, with the reflected wave amplitude acting as the modulated signal can be strongly modulated, and the zero transmitted wave amplitude to create a quasi-perfect mirror. In conclusion, the device can operate also as a switch that totally reflect and transmit the incident wave, accordingly, depending on the given wavelength. In addition, modifying the geometry the alternate designs can give a better modulation performance.

### 4.1.2 Cross-based SRR with 1 asymmetry simulation

In order to improve the electromagnetic response of the cross-shaped SRR metamaterial a reasonable idea is to create an one direction fold asymmetry. Asymmetries have been studied on a great scale in metamaterials and it has been proved that including them in the architecture can give better performance that conventional symmetrical geometries.

Asymmetries can enhance the Electromagnetically Induced Reflectance (EIR). EIR is an interference phenomenon where a narrowband state opens a reflectance window inside the broader absorption band of the whole state. Next step is to create a Plasmonically Induced Reflectance (PIR), where this phenomenon allows very narrow reflectance resonances in the electromagnetic response spectrum. For the plasmonic behaviour, at least one sharp reflection peak in the EM spectrum is formed [97]. This fulfills the condition in order to make devices suitable for ultra-fast switching in a narrow frequency band, signal processing and sensing [98]. Especially in low THz frequencies, this behaviour is almost impossible to be found in natural elements so metamaterials become significant for the development of this kind of devices.

For the creation of the one direction asymmetry in the cross-shaped design a feature of same width as the cross is inserted, at the edge of one cross's part. The CAD design is exhibited below. The dimensions for the design are a=25 $\mu m$, b=112 $\mu m$, c=45 $\mu m$, w=5 $\mu m$, h=25 $\mu m$ and periodicity 130 $\mu m$.

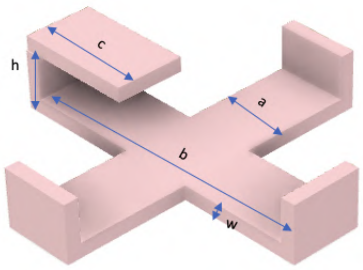


Figure 4.1.2.1: CAD design of asymmetric cross-shaped SRR metamaterial.

For the simulation, the material that was chosen is again PEC, while for the source the range of 0.5-3.5 THz was included (with excitation signal same as Figure 4.1.1.2). The mode that was selected was TM(0,0), exploiting the magnetic response of the structure. The results of the simulations for the asymmetric cross-shaped metamamaterial are presented in Figure 4.1.2.2.

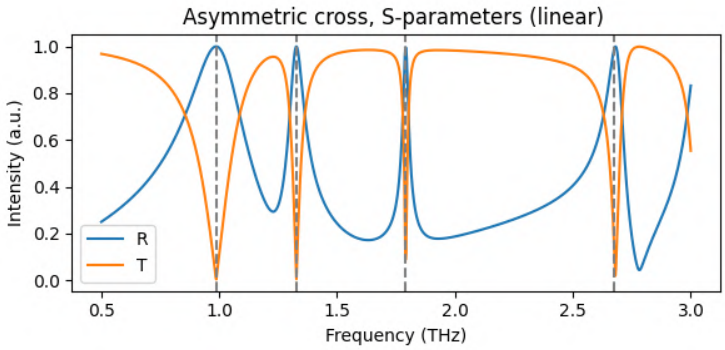


Figure 4.1.2.2: Simulation results of Reflection (R) and Transmission (T) for asymmetric cross-shaped PIR metamaterial.

A heat-map of surface currents flowing the asymmetric cross-shaped metamaterial is also provided in Figure 4.1.2.3.

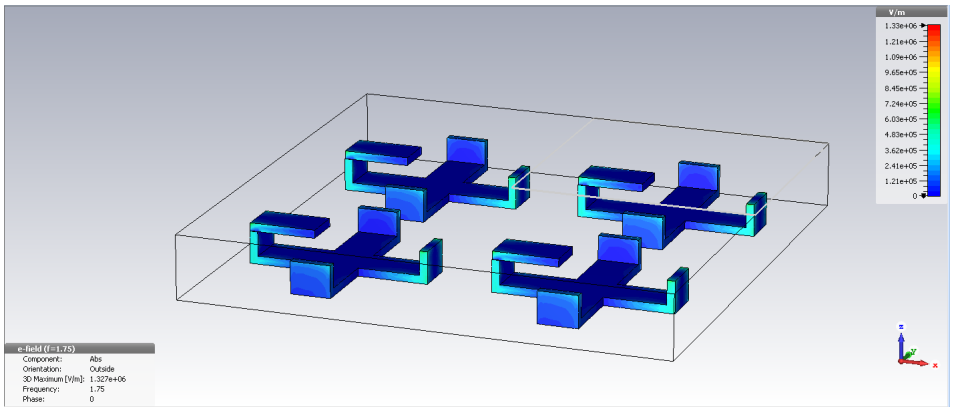

Figure 4.1.2.3: Absolute value of surface currents induced in cross-shaped metamaterial by 1.75 THz plane wave.

The electromagnetic response of the proposed structure, as taken from Figure 4.1.2.2 reveals a magnetically–tunable quad–band resonance with high tunability in the frequency range of 0.95–2.65 THz. The four resonances in a such narrow bandwith indicates the existance of PIR phenomenon. From the scheme of Figure 4.1.2.3 the flowing current at the asymmetric element of the geometry can be detected. The broken symmetry system leads to excitation of surface plasmon resonance (SPRs) which results in near field coupling between the plasmonic modes [99]. As a result, this may lead to an on/off switch performance due to the simultaneous total reflection while the transmission tends to be zero for specific wavelengths. In order to achieve PIR, the wide band absorption spectrum has to be zero when the resonance takes place. The calculated absorption (from equation 2.1.10.f) is presented below.

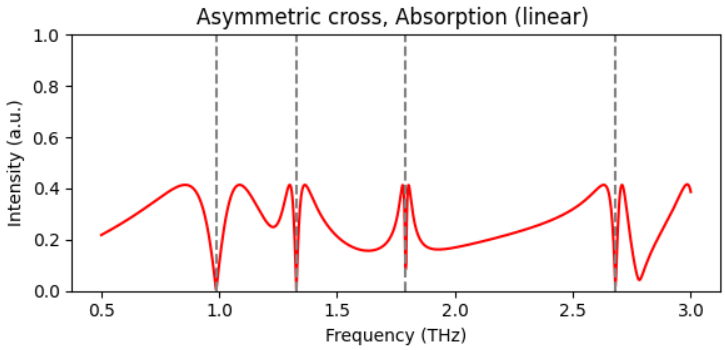


Figure 4.1.2.4: Calculated results of absorption for the asymmetric cross .

At the resonances, there are sharp reflection peaks while the absorption goes to zero. In combination with the zero transmission, low losses are obtained from the system. This means that no information is lost due to the architecture of the total system. When the incident field interacts with the cross the plasmons are excited. But, due to the asymmetry now there is higher-order excitation that leads to multiple resonances of the system. This characteristic is significant for metamaterials operating as electromagnetic filters, cutting the signal or letting pass in a very small frequency region. The narrow perfect reflection in combination with the zero transmission and absorption at specific wavelengths leads to a system that can reflect perfect

the electromagnetic signal as a mirror with no absorption and let transmit completely in a very narrow frequency band accordingly. Designs as the proposed one, can lead to the development of functional biological sensors that needs to have very narrow resonances in order to detain the signals at low THz frequencies which is a critical condition for sensing technology.

Finally, the fabricated array of the asymmetric cross-shaped design, using 2PP as a fabrication tool is presented in Figure 4.1.2.5 (using a 40x objective lens).

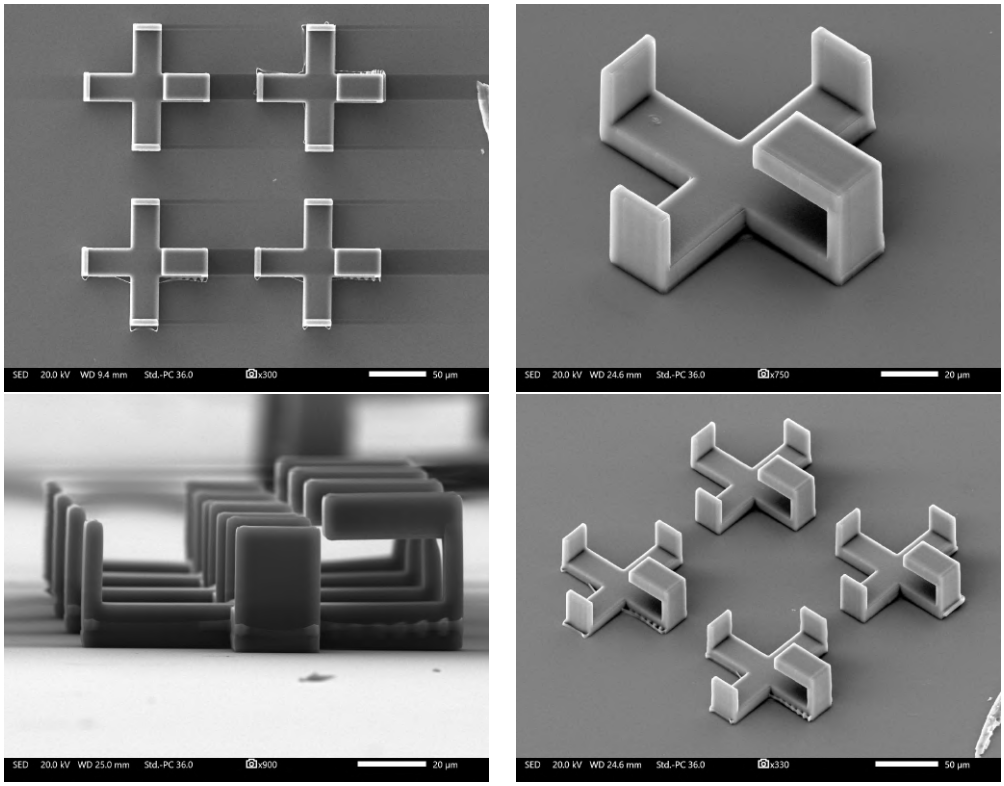


Figure 4.1.2.5: Sem images of the asymmetric cross-shaped metamaterial.

In Figure 4.1.2.5 the resolution of 2PP can be observed in different angles. This makes 2PP a highly suitable technique for the fabrication of metamaterials with complex geometries.

### 4.1.3 Cross-based SRR with double symmetry simulation

Following, it is critical to understand where the asymmetries in the architecture start to interact with each other and destroying the resonances. The basic component of the geometry remains the same, the cross-shaped SRR with the deformation at the edges. Now, two identical asymmetries can create a double symmetry. A x-y/y-x symmetry can enhance the electromagnetic interference of the wave and the medium but sometimes symmetries tend to cancel out the generated currents and fields. Although, the existence of the surface currents again is more than enough to create an LC system and provide oscillations for the electromagnetic resonance and leads to tuning magnetic response. Devices as the proposed one, can provide systems for sensing technology or filters for low THz but usually not as sensitive as with the one asymmetry theory.

The proposed geometry now, consists of the cross-shaped SRR as in subsection 4.1.2 with two symmetric parts added. The parts are inserted at the edge of the cross and have different length in order to create the double symmetry-asymmetry perspective. For the creation of the double symmetry cross-shaped design features of same width as the cross are inserted, at the edge of each cross's part. The CAD design is exhibited below. The dimensions for the design are now a=25 $\mu m$, b=112 $\mu m$, c=45 $\mu m$, d=50 $\mu m$, w=5 $\mu m$, h=25 $\mu m$ and periodicity 130 $\mu m$.

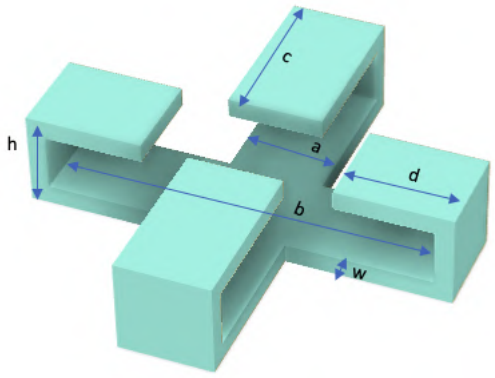


Figure 4.1.3.1: CAD design of double symmetric cross-shaped SRR metamaterial.

For the simulations, the material that was chosen was PEC for better electromagnetic response. In order to get the H-field characteristics, TM(0,0) mode was chosen for the source. The range of frequencies are 0.5-3.5 THz, for studying the low THz behaviour of the meta-structure (signal Figure 4.1.1.2). The simulation's results of the proposed system are presented below.

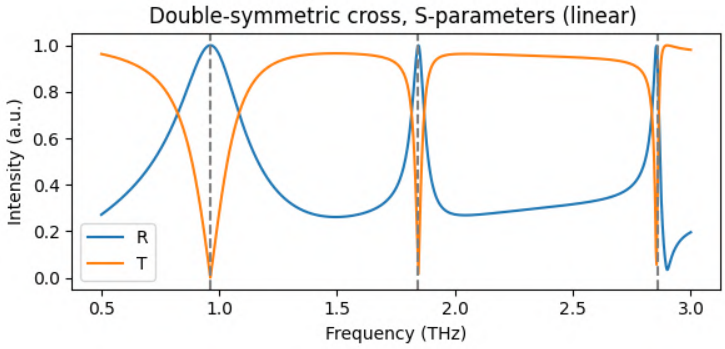


Figure 4.1.3.2: Simulation results of Reflection (R) and Transmission (T) for double symmetric cross-shaped PIR metamaterial.

Besides the resonances, in this situation is important to observe also the absolute value of currents flowing through the medium.

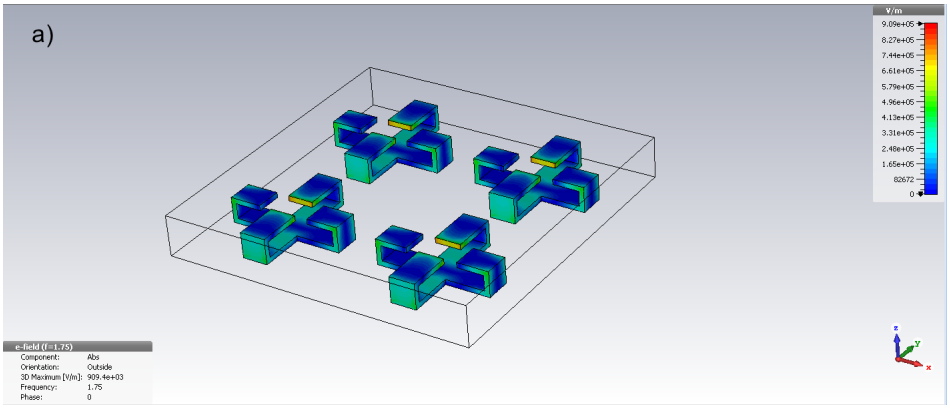


Figure 4.1.3.3: Absolute value of surface currents induced in double symmetric cross-shaped metamaterial by 1.75 THz plane wave, Phase=0.

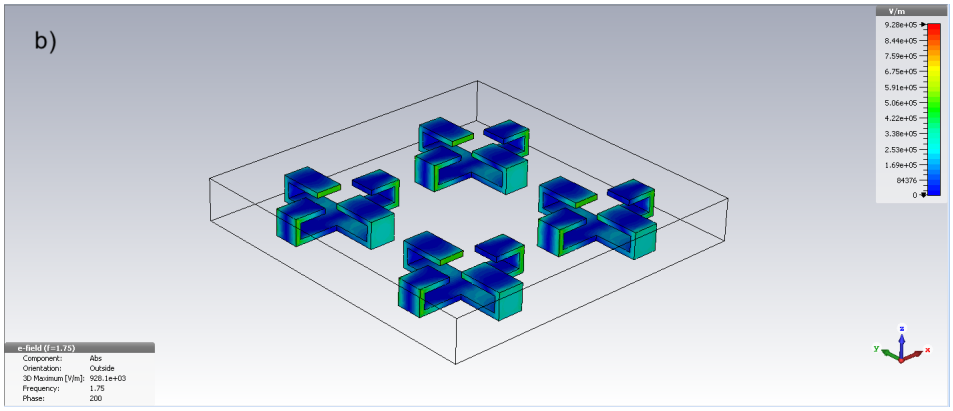


Figure 4.1.3.4: Absolute value of surface currents induced in double symmetric cross-shaped metamaterial by 1.75 THz plane wave, Phase=200.

From the results of Figures 4.1.3.3 and 4.1.3.4 it can be observed that the current flows in all directions of the extra features of the design and depending on the phase of the H-field it can decreased a lot. This can cause the resonances to neutralize each other and reduce the surface current. As a result, from Figure 2.1.3.2 the resonances now have change. There is a wide peak of reflection at 0.97 THz and a dual band narrow resonance at 1.9 and 2.9 THz respectively. The calculated absorption of the system is shown below also.

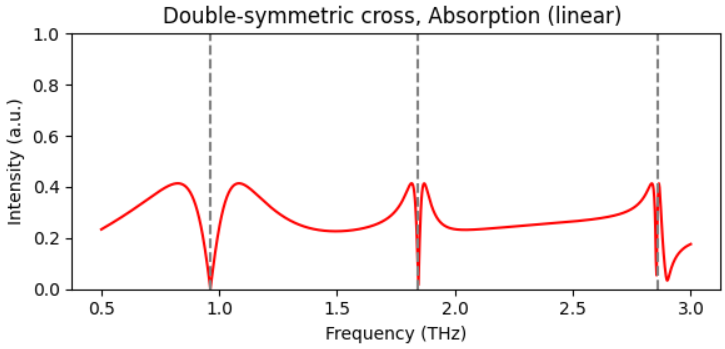


Figure 4.1.3.5: Calculated results of absorption for the double symmetry cross.

Similar to the previous suggested designs in subsections 4.1.1 and 4.1.2, a strong resonance band is noticed. The electromagnetic response is better that the one observed in the total symmetric cross-shaped metamaterial in Figure 4.1.1.2, but of lower rank than the one asymmetric cross-shaped metamaterial in Figure 4.1.2.2. This is a first indication that in geometries such as the proposed cross-shaped metamaterial, asymmetries can enhance the electromagnetic response of the system. Although, the phenomenon of zero absorption is observed again since when the reflection tends to a value of one (a.u.), transmission simultaneously tends to zero, providing an ultra-low losses device. The suggested device can be used as an attenuator, providing reduction in the strength of the signal depending on the wavelength that is operating. The last two ultra-narrow band resonances enhance the capability of the metastructure to be used as a switch for specific wavelengths. Also, the symmetry of the resonances in the frequnecy band provides Fano resonances with very sharp resonance features, theoretically leading to nearly zero losses [100], especially in the case of the third resonance at 2.9 THz.

Additionally, the fabricated proposed structure using 2PP technology is presented in Figure 4.1.3.6 (using a 40x objective lens).

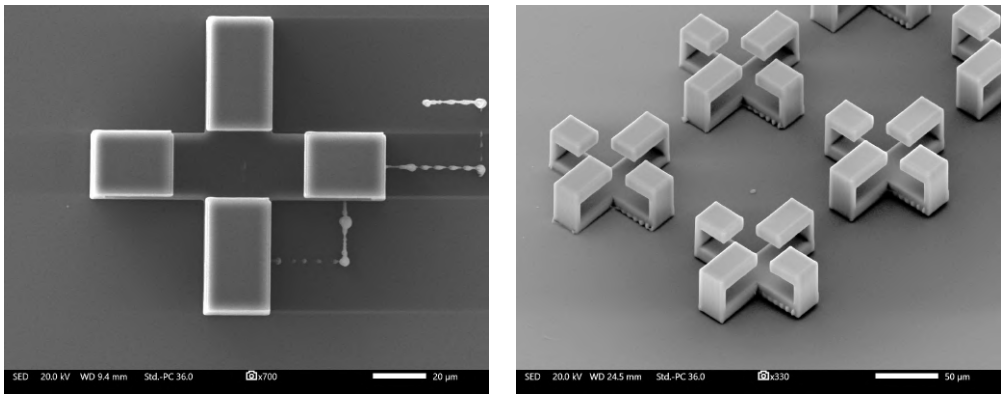


Figure 4.1.3.6: Sem images of the double symmetric cross-shaped metamaterial.

## 4.2 Summary for using simulations in study and development metamaterials

Using simulations for the study of low THz metamaterials provides a very strong tool for the optimization of the electromagnetic characteristics of the structured geometry. As it was demonstrated above, changing the architecture of a unit cell by just adding -a few $\mu m$ in size- elements can enhance the electromagnetic interference of the wave and the medium.

Although the material that is used is for ideal conditions, PEC provides a good indication about the characteristics of the geometry at the specific frequency band. Especially, in comparison with natural materials these geometries can provide manipulation of THz fields, something that is not possible to find in nature. Thus, even though ideal conditions are taking place in simulations, they are mandatory to find the ultimate design for the development of the device.

Changing the geometric parameters of the system the manipulation of the operation of the device can be easily done. In low THz frequencies, most of the metamaterials can operate as sensors, filters and switchers, due to the multi-band resonance that is noticed in this regime generated via the interaction of the electromagnetic field with the structural elements of the metastructure. This can lead to a highly promising development process for the fabrication of such devices that due to the luck of metamaterial's studies they are very challenging to be completed.

As it was presented above, using asymmetries in classic SRRs systems can enhance the electromagnetic response. This can lead to new capabilities for designing the optimized devices for new applications in low THz frequencies. But modifying the geometries can be really challenging due to the multiple and mutually reliant procedures that occur inside the system. Even though the material remains the same, changing the structural elements provides different operational characteristics. That is why, simulations are strongly corresponding with the study and development of metamaterial's technology and are very important to understand the exotic characteristics of the artificially constructed meta-atoms.

Comparing the results of transmission coefficients for the 3 proposed geometries, it was found that resonances were spotted at the same frequency band (0.5-3.5 $THz$), as it is presented in Figure 4.2.1. This happens due to the consistent size of the unit cell, which is highly correlated with the frequency of the resonance and the wavelength of the incident wave.

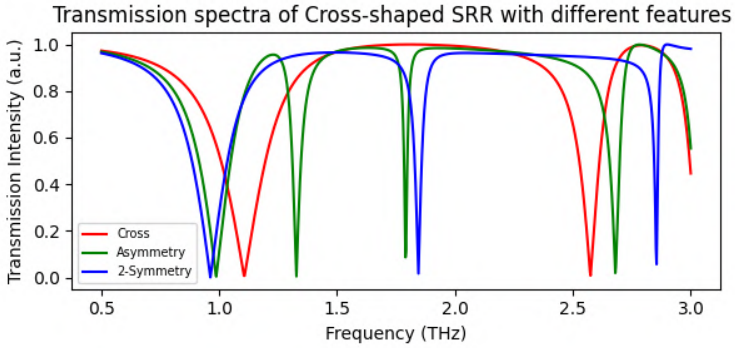


Figure 4.1.3.2: Comparison of Transmission (T) spectra for the three proposed Cross-shaped SRR designs.

In the case of the cross-shaped metamaterial with one asymmetry included there are the most resonances, while in the simple cross metamaterial there are the least. This indicates that asymmetries are very important since they provide fertile conditions for the electric and magnetic field individually, to interact with the specific elements of the geometry. Thus, TE and TM modes give increased number of resonances enhancing the electromagnetic response of the metamaterial. This, results in different operation modes providing a variety of applications that are related with sensors, filters, switches and mirrors, just to name a few, for these specific wavelengths that cannot be manipulated with materials that can be found in nature.

What is even important with the simulations although, is the transition from virtual environment to reality. This can be done using 2PP in a straightforward way, just by changing the CAD design. Thus, fabrication of complex metamaterials with different geometric elements can be achieved and with high resolution which is required in metamaterial's technology.

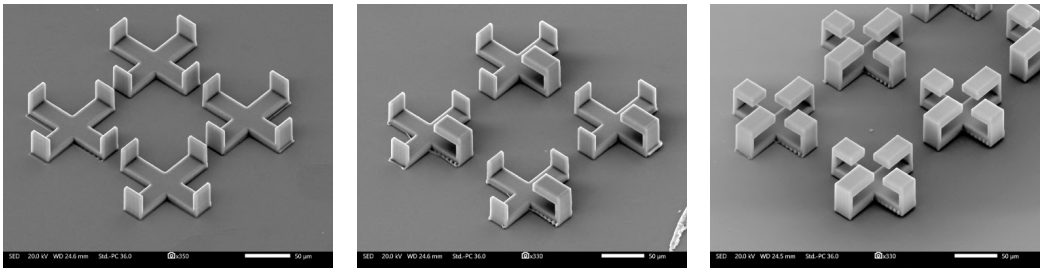

Figure 4.2.2: Sem images of the fabricated cross-shaped SRR, underlining the accuracy this printing technique provides and the straightforward way that different designs can be printed.

Emphasizing also the requirement of resolution in the development and fabrication of electromagnetic metamaterials, 2PP can provide the necessary accuracy and detail in the final fabricated structure. In Figure 4.2.2 and 4.2.3 is highlighted that using 2PP can fabricate changeable, versatile, geometries with high resolution and very smooth surface which can be related to the low losses that are important in a metastructure.

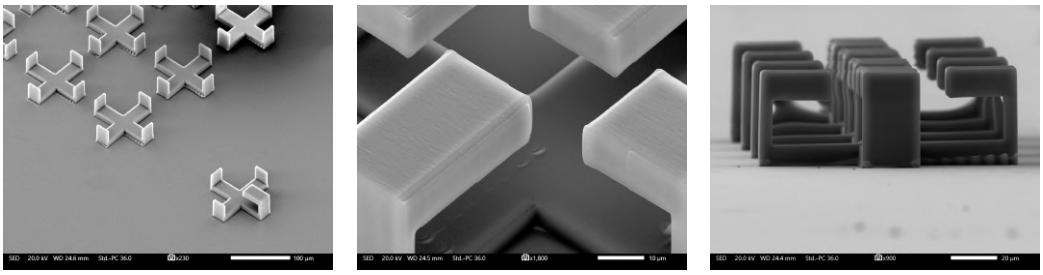

Figure 4.2.3: Sem images of the fabricated cross-shaped SRR, exploiting the resolution and surface quality, as well as versatility of the 2PP technique.

Creating metamaterials with asymmetries has a high influence in the development of state-of-the-art metamaterials that can operate at low THz frequencies and provide new applications that can be used in THz technology. Inspired from the theoretical study of asymmetries induced in classic SRR metamaterials, in chapter 5 the whole process, from simulations to production and measurements, will be presented for a futuristic geometry.

# 5 Asymmetric pillars SRRs for low THz applications

Recently, filling the "THz gap" where nature's element are not able to modulate terahertz wave effectively has an increased interest in scientific community for the fabrication of artificial designed materials that are suitable to manipulate waves of these frequencies. As it was discussed before, low THz regime refers to electromagnetic waves in the frequency range from 0.1 to 10 THz. These frequencies require high resolution printing process, making the realization of the theoretical designed structures challenging. The complete study and development of state-of-the-art low THz metallic metamaterial design based on asymmetric pillars resonators is presented below, using FDTD for the theoretical study to achieve the optimal response of the design and two photon polymerization for the fabrication process.

## 5.1 State-of-the-art metamaterial filter for low THz

A novel design of pillars creating free-standing U-shaped SRRs with asymmetry in one direction will be presented. Recently, this kind of metamaterials have attracted quite some interest because of its promising behaviour for a low-loss slow-light medium. Slow-light media can exhibit very slow propagation velocity of the electromagnetic wave [101] or even stop the light entirely [102]. One of the mechanisms that are responsible for such operation in electromagnetic fields is Electromagnetically Induced Transparency (EIT) where a medium turns transparent in a narrow transmission window with low absorption and sharp dispersion, resulting in slow light and optical storage applications [103]. The characteristic features of EIT, simultaneously low absorption and sharp dispersion, can be observed in classical systems as coupled resonators [104] and described by a simple model of two coupled harmonic oscillators resulting in dark and bright resonances [105].

In the present thesis, the individual oscillators are sub-wavelength electromagnetic elements that compose an electromagnetic metamaterial in low THz regime (approximately 3 $\mu m$). The excitation of a dark mode now can be described by the microscopic electric or magnetic dipole moment that is created in the unit cell of the metamaterial with broken symmetry, fulfilling the essential requirement of EIT: "two coupled resonances that are

asymmetrically driven by the external force" [105]. The external force in electromagnetic fields are the components of the electric ($\overrightarrow{E}$) and magnetic field ($\overrightarrow{H}$), accordingly. Probing EIT in 3D bulk materials can be challenging since most EIT metamaterials are single-layer structures.

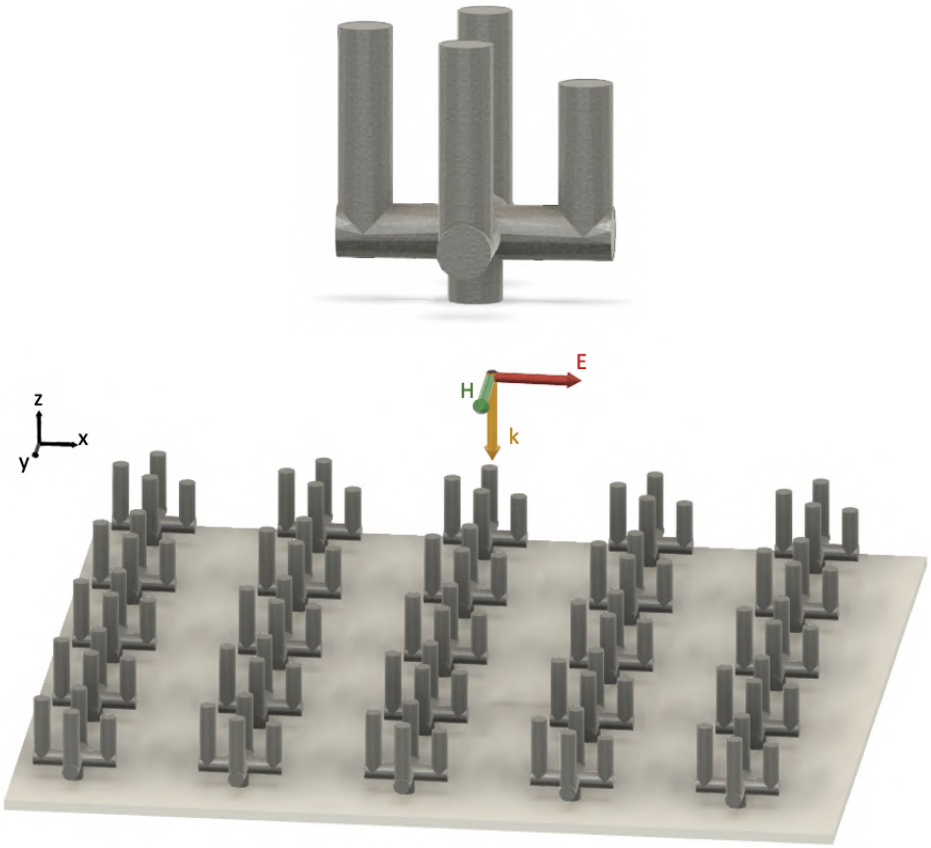


Figure 5.1.1: CAD design of the double U-shaped SRR and metasurface with axis orientation and direction of the electric (E) and magnetic field (H). The incident wave is propagating vertically to the surface (k) (grey=silver).

The original idea behind the "cactus" 3D structure is to couple the electromagnetic response of two different U-shaped free-standing structures, with the one consisting of a broken symmetry in one direction compared to the

other one. Dark and bright plasmonic eigenmodes in the medium are enhanced by the TE and TM electromagnetic modes correspondingly, that are parallel to the x-y plane and placed properly compared to the direction of the broken symmetry. Transmission results for the proposed metasurface in Figure 5.1.1 obtained from simulations are presented in Figure 5.1.2. For frequencies above 3.75 $THz$, periodicity (80 $\mu m$) overcomes the wavelength. Thus, sub-wavelength size condition is no longer fulfilled and there is excitation of higher diffraction orders.

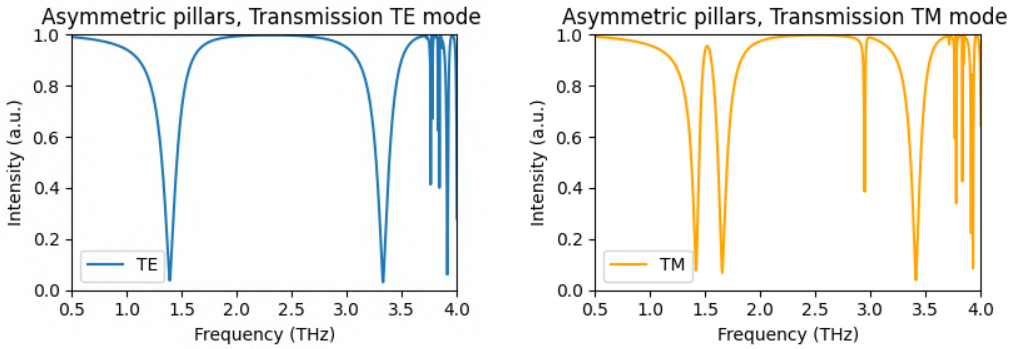


Figure 5.1.2: Simulation results of Transmission for TE and TM mode.

First of all, it is interesting to investigate the electromagnetic response of the individual elements of the design. The two separate U-shaped designs are combined perpendicularly at the final design (Figure 5.1.1). The first element is a classic analog of U-shaped SRR where both pillars have the same height. We consider that both of the pillars are positive charged (conventionally) and there is one resonance created from the pillars,due to the coupling of the positive charges. Since the aim is to study EIT, the transmission spectra has to be calculated theoretically with FDTD method for TM(0,0) and TE(0,0) modes, respectively. These two modes are defined by the polarization of the incident electromagnetic wave regarding to the plane. Propagation is along the z axis and it is considered that electric field (E) is pointing along x axis, while magnetic field (H) is pointing along y axis. Schematic presentation of the unit cell of the symmetric U-shaped SRR, as long as the transmission spectra for TE and TM mode (using PEC as material) as they were calculated through the simulations are presented in Figure 5.1.3.

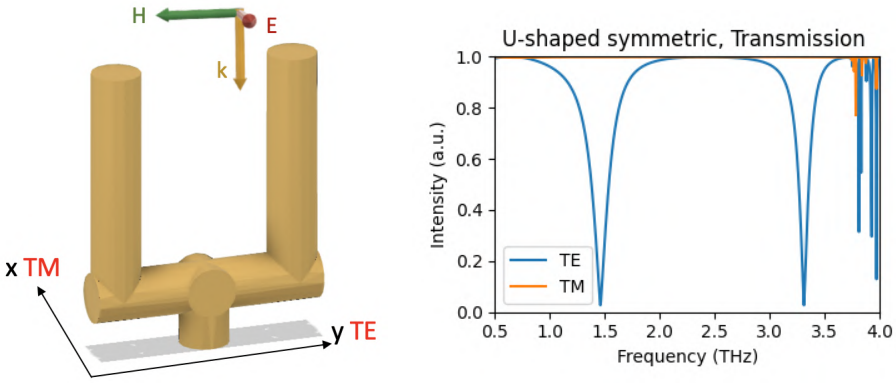


Figure 5.1.3: CAD design of the U-shaped symmetric structure with TE and TM mode's orientation and results of transmission spectra for TE and TM modes (gold=PEC).

It is clear from the transmission spectra in Figure 5.1.3 that in TM mode there are no charged elements and subsequently no interaction with the electric field. Thus, transmission remains constant to a value of one. At the same time, the pillars in the direction of the magnetic field (y axis) create a magnetic dipole that results in broad resonances of zero transmission in specific frequencies.

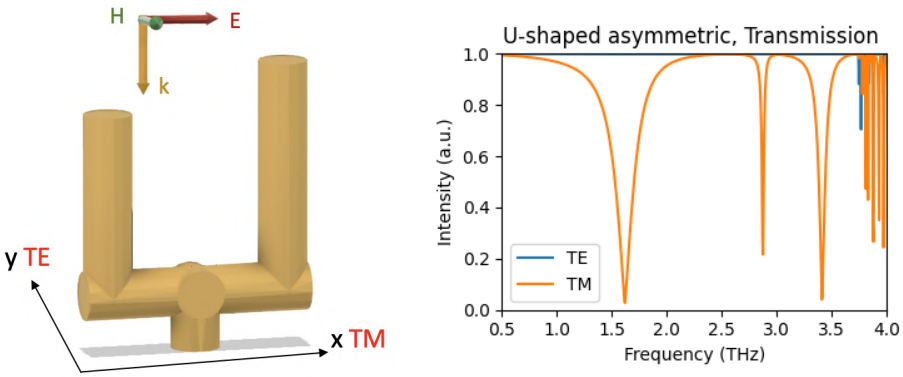


Figure 5.1.4: CAD design of the U-shaped asymmetric structure with TE and TM mode's orientation and results of transmission spectra for TE and TM modes.

Similar to the previous U-shaped SRR, the other element is rotated 90 degrees in the plane to enhance the electric field from TM mode (along x axis). In order to create different dipole moment and enhanced electromagnetic response, the one pillar is slightly shorter than the other resulting in broken symmetry. Schematic presentation of the unit cell, as long as the transmission spectrum for TE and TM mode as they were theoretically calculated are presented in Figure 5.1.4.

From the results in Figure 5.1.4 it is clear now that only TM mode and subsequently electric component of the field is interacting with the elements of the structure, since transmission for TE mode is constantly in value of one making the meta-atom completely transparent. In addition, the broken symmetry creates different resonant response not only in electromagnetic field components (TE, TM) but also in the frequencies that resonances occur.

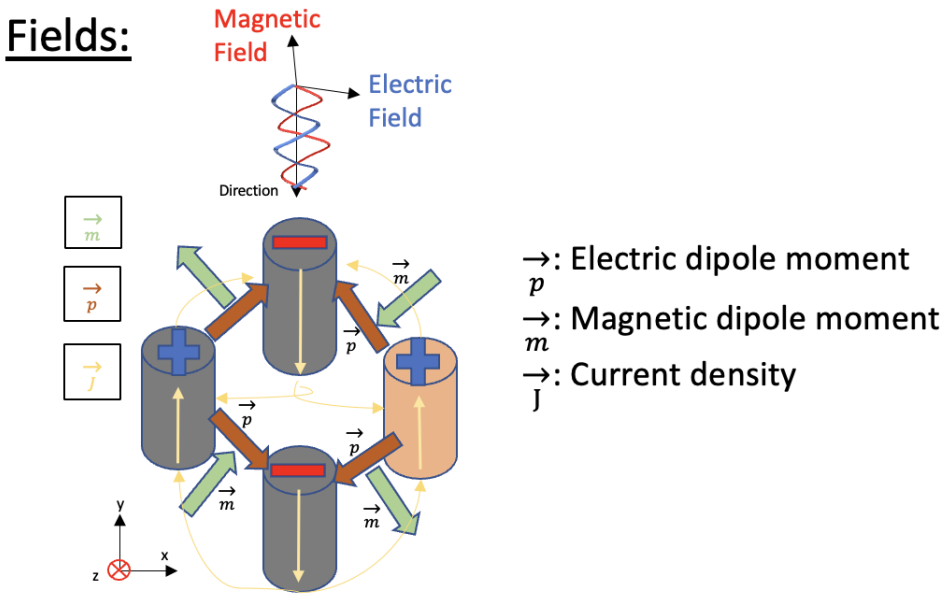


Figure 5.1.5: Schematic presentation of the pillars, including the charges and the electromagnetic field components that are creating the electric and magnetic dipole moments.

In order to be more clear how the charges are distributed in the new dipoles and subsequently the electric and magnetic dipole moment changes, resulting in extraordinary transmission response of the meta-atom, a schematic of the system with the asymmetric pillars is presented in Figure 5.1.5. Excitation of different resonance mode that is depending not only on the coupled resonators, but also on the external force of the incident field, is possible to occur if a displacement from the microscopic electric or magnetic dipole moment is present in the system. Combining the two proposed U-shaped SRR, a new design with different operating mechanism is generated. In this situation, it is reasonable to consider that each separate U-shaped design has opposite charge from the other. Thus, interaction between the pillars of the same U-shaped element will neutralize both the electric and magnetic response that was observed in the individual components and there will be no coupling from opposed pillars.

As it is presented in Figure 5.1.5, it is considered that opposite elements have the same charge, creating current loops with each nearest-neighbor, while there is no cross-interaction between the parallel features. Since the pillars are positive and negative charged, an electric dipole moment is generated with direction from positive to negative charged element, while at the same time a magnetic dipole moment is generated with direction depending on the Right-handed coordinate system (see section 2.1) that is assumed, as it is presented on the left side. The electric field is propagating along x-axis providing the TM mode, while the magnetic field is propagating along y-axis creating the TE mode. The incident electromagnetic wave is propagating perpendicularly to the plane of the meta-atom. As a result, a coupling response is produced by the two SRRs. From the aspect of the electric current, the charges of the pillars are the same, thus, the electric dipole moment that is generated is neutralized and does not affect the electric response of the system. For the magnetic dipole moment, the vector of the shorter pillar is different from the near one, resulting in non-zero total magnetic dipole moment. The broken symmetry of the system result in alternating the direction of the magnetic dipole moment. Bigger asymmetries imported in the system of the pillars and larger difference in height of one element results in larger difference in magnetic dipole moment, while the average dipole moment must be proportional to the electric field at the surface.

The surface loop current that is created through the propagation of the electromagnetic wave through the metasurface is presented below, in Figure 5.1.6. The heat-map (blue color refers to zero current) that is presented shows the case of propagation of the electric field where the asymmetry takes place.

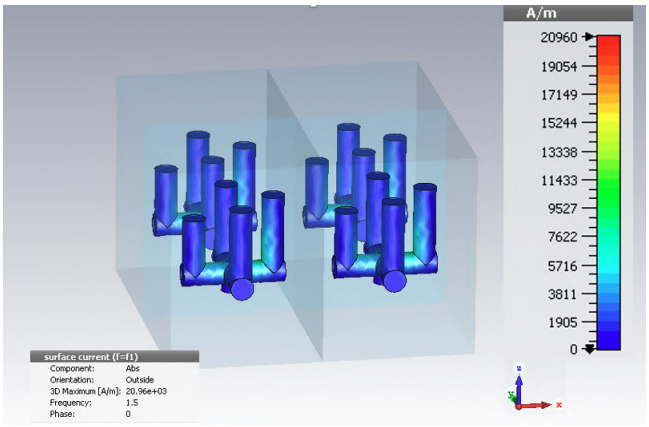


Figure 5.1.6: Absolute value of surface currents generated from the current loop of asymmetric pillars in TM mode.

Distribution of the surface current in Figure 5.1.6 shows that the surface currents at the resonance frequency of 1.5 THz (Figure 5.1.2) are reaching to a value of zero at the top of the pillars as it was predicted in Figure 5.1.5 though the opposite charges that formed on the pillars. Combining the two U-shaped SRRs results in one new resonance mode superimposed from the coupling of the two separate resonators, as it is theoretically calculated in Figure 5.1.2 from the simulations. Thus, it is expected to show a sharp peak in transmission between the two broad resonances that are exhibited in Figures 5.1.3 and 5.1.4 in low THz frequencies.

From the results of transmission in Figure 5.1.2, it can be observed that in TE mode, where the symmetric pillars are placed, the resonance remains unchanged and are similar to the results of Figure 5.1.4 of the symmetric SRR. What is very interesting is the transmission in TM mode, where the asymmetric pillars are designed, that a sharp peak is exhibited between the two resonances where transmission tends to zero. This is aligned with our

above mentioned claims about the expectation of a sharp peak in transmission spectra within a narrow frequency band. The steep transition from the value of one to zero and from zero to one, and then again in zero, in such a narrow frequency regime (approximately in just 0.2 THz) indicates the presence of bright (transmission close to a value of one) and dark resonances (transmission tends to a value of zero). On one side, there is a bright resonance occurs due to the broken symmetry followed, by a dark resonance due to the symmetric pillars in opposite direction. This superposition of the resonances comes in agreement with the two transmission spectra in Figures 5.1.3 and 5.1.4 in the frequency that the resonances occur.

This transmission behavior indicates that EIT occur in this "cactus" metamaterial design. The double resonance with a sharp peak existing between them and the steep transition from dark to bright oscillations makes the recognition of EIT in this theoretical model possible. Now there are losses from the silver and the roughness of the surface inserted in the simulations in order to make the calculations as close to the experimental environment. Bright resonance can be observed at 2.1 THz. Thus, the theoretic model about EIT in low THz metamaterials seems to come in an agreement with the predictions.

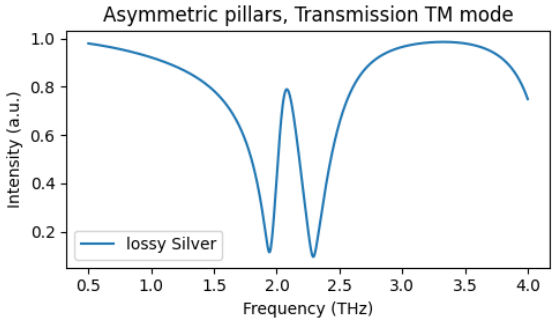


Figure 5.1.7: Simulation results of Transmission for TM mode using lossy silver as material and other losses imported in the calculations.

It is also reasonable to assume that due to the large, narrow, transmission and small absorption, the transmission phase will exhibit a large normal dispersion, with a fast phase shift in narrow frequency's window (Figure

5.1.8) which also leads to a significantly enhanced group delay [105], since the group velocity is strongly correlated with the slope of transmission phase shift ($\tau_g = -d\phi(\omega)/d\omega$). This slight difference in frequency superimposed in the transmission spectra (Figure 5.1.7) will also results in different group velocity that can enhance the slow light mechanism for promising results in applications for light storage, even when the medium is getting transparent at the bright resonance.

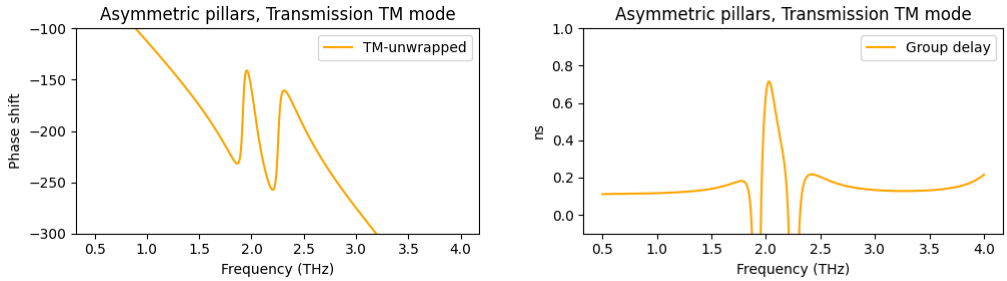


Figure 5.1.8: Simulation results of Transmission phase for TM mode using lossy silver as material and calculated group delay of the metasurface.

From the theoretical results in Figure 5.1.8, and in combination with the frequency depended transparency of the metasurface in Figure 5.1.7, there is something remarkable takes place. At the bright, transmission peak resonance (Figure 5.1.7), it can be observed that value of transmission phase (Figure 5.1.8) is reduced in a very narrow region. This results in high slope which subsequently results in large, positive values of group delay. As it is exhibited in the right graph in Figure 5.1.8, group delay is constant until the resonance's deep, where the metasurface becomes non-transparent and it reaches high negative values of delaying in a very narrow frequency window. Almost simultaneously, at the bright resonance the group delay reaches at a value of approximately 0.8 $ns$, which indicates that even though the metasurface is transparent at this frequency regime, the wave that is propagating through the metamaterial is delayed due to the high group delay value. In order to experimentally prove that this mechanism can exist in the suggested metasurface, electromagnetic response of transmission as it was calculated in Figure 5.1.2 has to be measured for TE and TM mode at the resonance frequency.

## 5.2 Fabrication of the proposed structure

For the fabrication of the proposed "cactus" design, a high resolution printing technique is required. Thus, 2PP is suitable to fabricate this kind of structures for all the reasons that have been mentioned above. The CAD design is presented in Figure 5.2.1, with a unit cell of $80\mu m$ and the basic elements of the design to be $arm_1 = 40\ \mu m$, $arm_2 = 32\ \mu m$, resulting in broken symmetry, $L = 40\ \mu m$ and diameter of the cylinder to be $d = 9\ \mu m$.

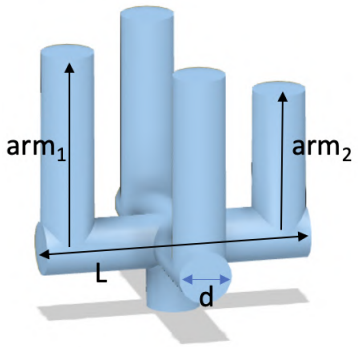


Figure 5.2.1: CAD design of the proposed asymmetric pillar SRR.

For the fabrication the setup with the Galvo-scanner was used as it was presented in section 3.3, using an 40x objective lens with N.A.=0.95. The power was set at 100mW, while the scanning speed was $3000mm/s$.

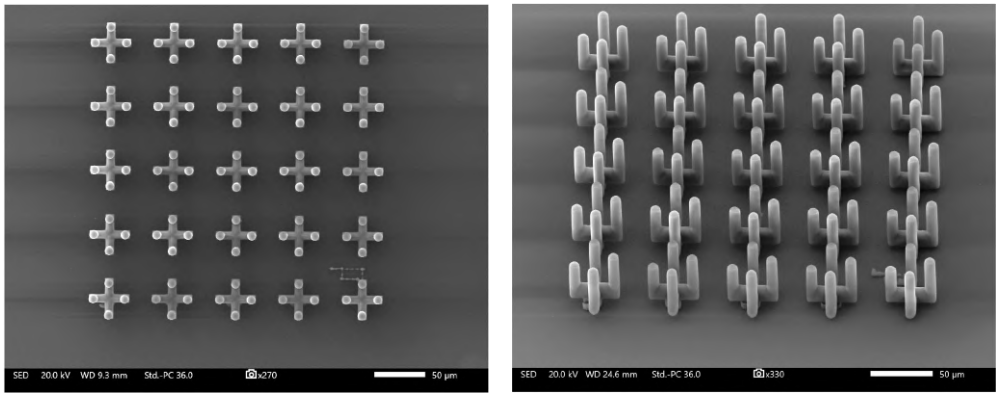

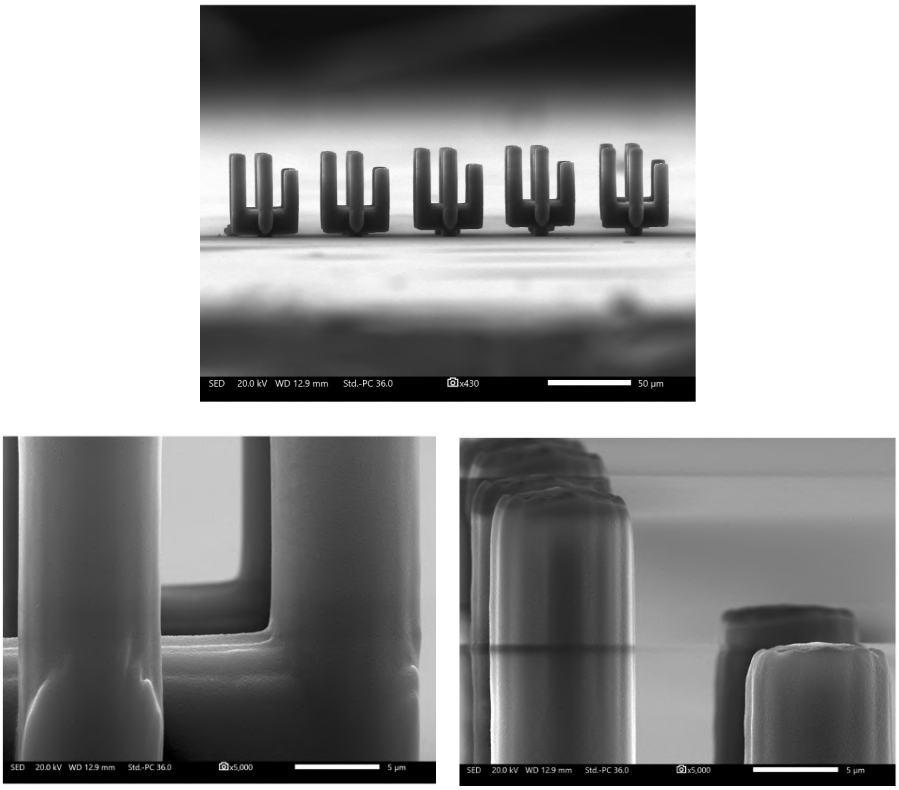


Figure 5.2.2: Sem images of the fabricated asymmetric pillars SRR, underlining the accuracy this printing technique provides and the detailed fabrication of the asymmetric cylinders.

Using the setup including the galvo-scanner mirrors provides a handful tool for the fabrication of detailed structures. In addition, it is a high-detailed fabrication process with small fabrication time consumption due to the capability of printing large areas with high scanning speed of the laser beam in the photosensitive material. Thus, the fabrication of the proposed metasurface is done in a straightforward manner. In order to measure the transmission response of the metamaterial design experimentally, the structures had to be covered with a highly conductive material, such as silver and fabricated on a high resistivity silicon substrate which is transparent in low THz frequencies.

## 5.3 Electroless coating with silver nanoparticles

In order to create metallic metamaterials, an Ag-based metallization process is required. The following process is a modification of the one established by K. Terzaki [106] and further demonstrated by M. Manousidaki [11] for the photoresist SZ2080 with 30% DMAEMA that is used in the present thesis (synthesis was discussed above in subsection 3.2). The photosensitive material is doped with metal-binding tertiary amine moieties (DMAEMA). This metallization technique is 100% selective as Energy Dispersive X-ray Spectroscopy (EDX) measurements shown compared to other metallization techniques (for example Physical Vapor Deposition (PVD) [107] and Chemical Vapor Deposition (CVD) [108] that are used widely) providing a useful tool to exploit the exotic properties of electromagnetic metamaterials. Conductivity measurements showed that the experimental conductivity of these silver nanoparticles is $\sigma = (5.71 \pm 3.01) \times 10^6\ S/m$ [109] which is very close to the pure Ag conductivity $\sigma = (6.3 \times 10^7)\ S/m$.

The process consists of three steps: seeding, reduction and silver plating.

1. Ag seeding: The sample is immersed in $0.05M\ AgNO_3$ in $H_2O$ for 38-42 hours. This creates pores on the surface of the polymerized material. Subsequently, the sample is immersed in distilled water and let it dry completely.

2. $NaBH_4$ reduction: Immersing the sample in $6.6M\ NaBH_4$ aqueous solution for 22.5 hours. In this step the surface is prepared so the Ag nanoparticles can be attached on the polymer. This is a violent chemical interaction, so if the fabricated structures have a big ratio of base and total volume then it is suggested to prepare the solution from the previous day. Subsequently, immerse the sample in distilled water and let it dry competely.

3. Ag plating: In the final step there are three solutions that have to be prepared; (a) 0.2M $AgNO_3$ in $H_2O$, (b) 5.6% $NH_3$ in $H_2O$, (c) 1.9M glucose in $H_2O$ at volume ratios 5:3:8, at room temperature. First, (b) is poured in (a) drop-by-drop until the solution becomes completely transparent. Then (c) is also added to the solution. Finally, the sample is immersed in the solution for 1-2 minutes. This step is to cover

the surface with densely packed silver nanoparticles. The sample is removed and rinsed with distilled water and let dry completely.

The final step of the process can be repeated from 2-5 times, depending on the thickness of silver layer required for the application's needs. From SEM measurements it was found that the thickness of the silver was varying from 20-180 nm, depending on how densely the silver nanoparticles are distributed. Also, it was observed that after 5-6 baths in the final solution the silver on the structures started to aggregate causing deformations on the sample. Some indicative values for the preparation of the solutions are:
1. 20ml $H_2O$ +0.1698gr $AgNO_3$
2. 20ml $H_2O$ +1.875gr $NaBH_4$
3. (a) 0.339gr $AgNO_3$ + 6ml $H_2O$, (b) 0.37gr $NH_3$ + 6ml $H_2O$, (c) 5.47gr glucose + 16ml $H_2O$.

In order to observe how the silver nanoparticles are arranged on the surface of the polymerized material the samples underwent through SEM.

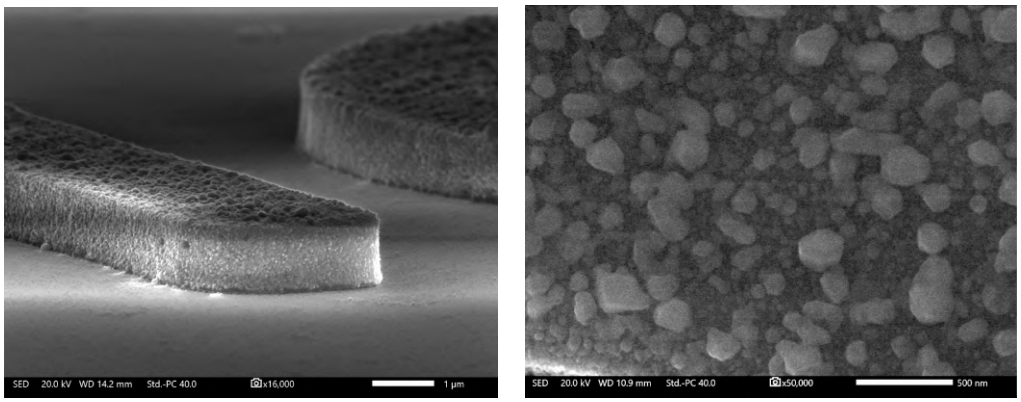


Figure 5.3.1: Sem images of fabricated structure after the metallization process.

From the SEM images in Figure 5.2.1, it can observed that the Ag nanoparticles are attached only on the polymerized material and not on the substrate. Also, another notice is that silver rocks are formed in an irregular way and size. Furthermore, EDX measurements were conducted to prove that the process is competely selective.

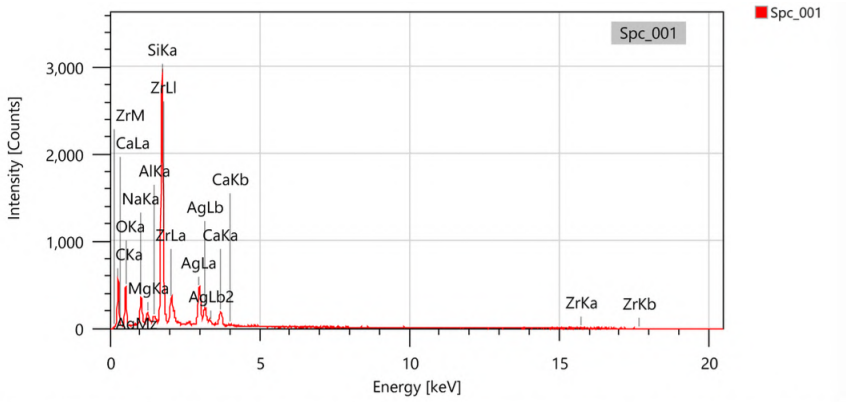


| Name | C | O | Na | Mg | Al | Si | Ca | Zr | Ag | Total |
|---|---|---|---|---|---|---|---|---|---|---|
| Spc_001 | 37.52 | 23.91 | 3.03 | 0.76 | 0.37 | 16.05 | 1.79 | 5.55 | 11.02 | 100.00 |
| Average | 37.52 | 23.91 | 3.03 | 0.76 | 0.37 | 16.05 | 1.79 | 5.55 | 11.02 | |
| Standard Deviation | | | | | | | | | | |

Mass%

Figure 5.3.2: EDX spectrogram of the metallized structure. Silver (Ag) peaks are clearly visible.

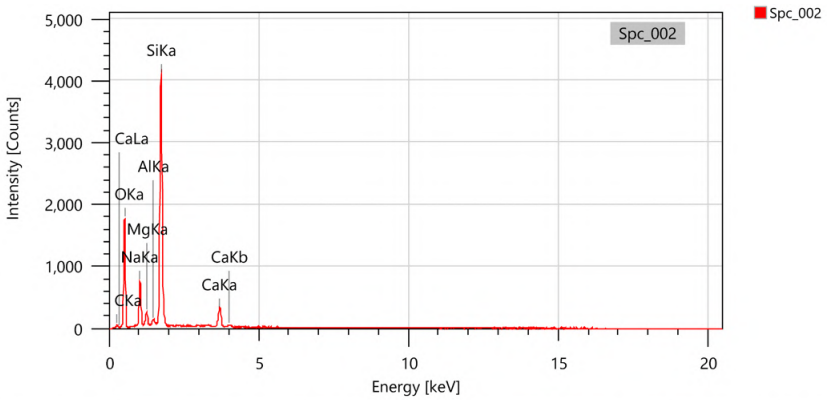


| Name | C | O | Na | Mg | Al | Si | Ca | Total |
|---|---|---|---|---|---|---|---|---|
| Spc_002 | 5.44 | 49.86 | 8.05 | 1.95 | 0.70 | 29.68 | 4.33 | 100.00 |
| Average | 5.44 | 49.86 | 8.05 | 1.95 | 0.70 | 29.68 | 4.33 | |
| Standard Deviation | | | | | | | | |

Mass%

Figure 5.3.3: EDX spectrogram targeting at the substrate of the sample.

From EDX measurements in Figures 5.2.2 and 5.2.3 it is evaluated that the Ag particles are attached only onto the polymer.

## 5.4 Measuring system

The characterization of the sample conducted in collaboration with Ultrashort Nonlinear Laser Interactions and Sources (UNIS) research group in IESL-FORTH. In order to detect the response of the fabricated sample in THz frequencies, Time Domain Spectroscopy (TDS) was used [110]. THz time-domain systems use the time-resolved pump-probe method to measure the shape and intensity of the THz pulse, or waveform.

Generation of THz waves is done using a fs laser pulse which generates transient photo-carriers in photo-conducting antennas (PCAs). A PCA consists of two metallic electrodes which are placed on the top of a semiconductor substrate with specific band gap. Applying bias voltage between the electrodes accelerate the photo-carriers which are generated by the laser pulse. Depending on the band gap of the semiconductor and the applied bias, THz radiation is generated [111] (Figure 5.4.1). The THz PCA emitter and detector have to be fully aligned above and below the sample, respectively, in Transmission measurements. When PCA is placed as a detector, the photocurrent generated by the probe beam across the electrodes gap and biased by the THz electric field is measured. This results in the detection of an electric pulse in time domain which is subsequently transforms in frequency domain using Fourier Transform.

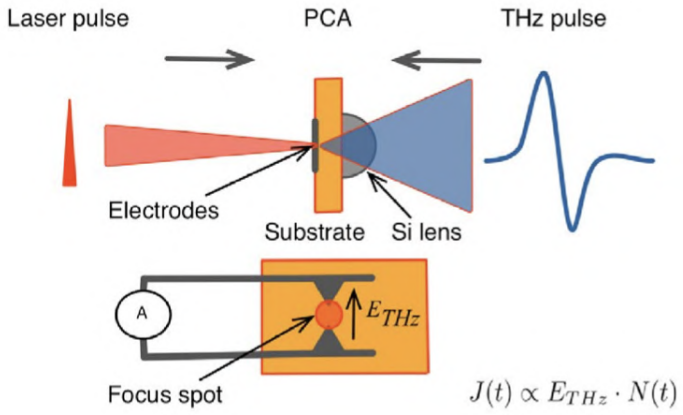


Figure 5.4.1: Detection layout of THz radiation using PCA.

A typical spectrum in time domain of the THz pulse detected on reference metal and thick glass is presented below in Figure 5.4.2. The time delay of the two signals and the intensity of the pulse provides the information that is required in the Fourier Transform to calculate the intensity of the scattering parameters of reflection and transmission.

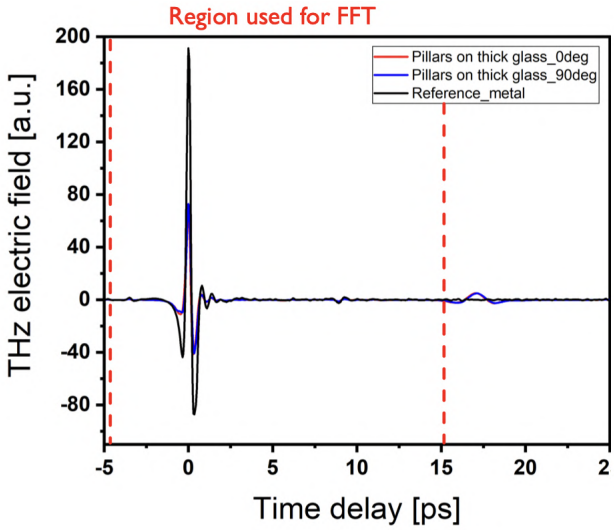


Figure 5.4.2: Electric signal detected from PCA.

After the Fourier transform, in order to calculate the transmission of the sample, the transmission response of the silicon substrate is measured as a reference. For the final result, the transmission response of the sample in frequency domain is divided by the transmission response of the reference sample (substrate) which results in the transmission of the metasurface.

As a way to measure the TE and TM mode of the metamaterial, the sample first was placed horizontal (TE mode) and then it was rotated 90 degrees (TM mode). The orientation refers to the propagation of the electric and magnetic field in x and y axis accordingly (Figure 5.1.1).

## 5.5 Results and discussion

In order to characterize the electromagnetic response of the fabricated sample, the structures had to be fabricated on the top of a silicon substrate and then metalized with silver nanoparticles. It is mandatory that only the structures must be conductive and covered with Ag particles, and not the substrate in order to create the different refractive index and conductivity ratio that is required for measurements in low THz regime. The final sample was fabricated in large a area ($3.2 \times 3.2\ mm^2$) compared to the size of the unit cell ($80\ \mu m$) to achieve better focus and fulfill the minimum focus spot of the beam in the measurements instrument as it was discussed above. In Figure 5.4.1 images of the fabricated sample undergoing through the metalization process are exhibited.

Figure 5.4.1: Images of the final sample, through the metalization process highlighting the change of the surface refractive index and color of the sample.

From the pictures in Figure 5.4.1 it can be clearly observed that the fabricated structures are changing color through the metalization process. This is a first indication that the structures are being coated with a thin layer of silver nanoparticles. Although, in order to detect the signal from the structures at low THz frequencies, thickness of the silver has to be much more than a thin layer. It is estimated that in 1-3 $THz$ the thickness of the silver must be at least 80-100 $nm$. For this reason, the final step of Ag plating process is repeated approximately 5-7 times. This can cause damage to the sample since it is a highly reactive chemical procedure and sometimes it creates a very thin layer of Ag even at the substrate, as it is observed in the right picture of Figure 5.4.1. It can also lead to aggregation of silver nanoparticles

on the structures, as well as on the substrate in random places. In order to get a rough estimation of the silver thickness, as long as the quality of the fabricated structures after the metalization process the sample underwent into SEM again.

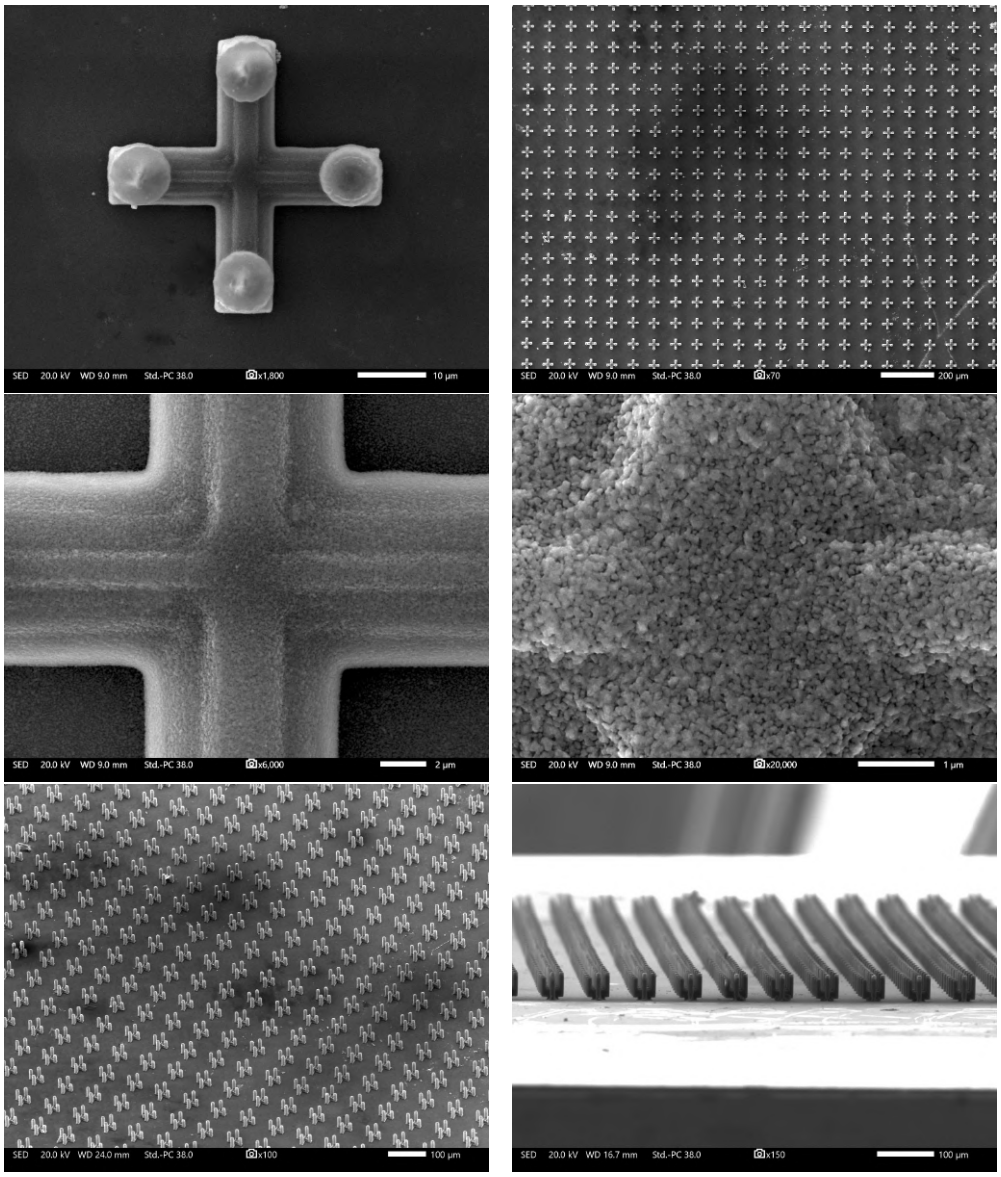


Figure 5.4.2: Sem images of the fabricated, metalized final sample.

In order to get the correct theoretic electromagnetic response of the final sample, after the SEM the unit cell of the design in the simulations was alternated. More specifically, the height of the pillars changed a bit which in these wavelength results in significant resonance shift. Moreover, the material that was used in the simulations changed to lossy silver with specific conductivity of the coated silver as it was presented in chapter 5.3 and finally a roughness of 500 $nm$ was imported in the coating layer of silver. These parameters change remarkably the resonance, but not the operational characteristics. Thus, due to the losses that are inserted in the simulation we expect to get lower intensity of transmission but unchanged behaviour of the sharp peak between the two transmission resonances. The theoretical and experimental results are presented in Figure 5.4.3, for the TE and TM mode accordingly.

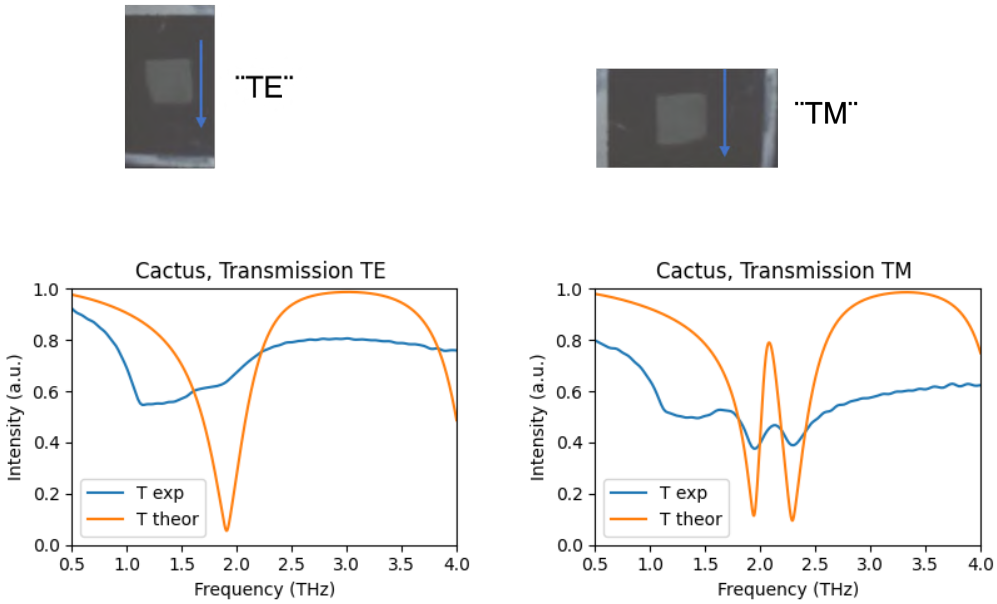


Figure 5.5.1: Simulation and experimental results of Transmission for TE and TM mode, accordingly, for the final sample. Orange line shows the theoretical results from the simulations, blue line demonstrates the experimental results.

For the experimental procedure, TE mode refers to the placement of the sample with direction that the incident field is propagating through the symmetric pillars of the geometry, while on the other hand TM mode refers to the

placement of the sample that the field propagates through the asymmetric pillars.

Results shown in Figure 5.5.1 seems quite interesting. First of all, there is different response of the sample regarding to the direction it was placed, exhibiting the different behaviour of the structure when the incident field is propagating through the symmetric pillars (TE mode) and asymmetric pillars (TM mode). In both occasions, irrespective of the intensity in the transmission, the resonances occur where the theory predicted to. For TE mode, the drop that was expected is at the frequency of 1.9 THz (blue curve), even though it is not so clear with all the losses that are included in the characterization of the sample, coming in agreement with the theoretical calculations (orange curve). For TM mode the sharp peak exhibited at 2.1 THz, while the narrow drops occur at 1.95 and 2.35 THz respectively (blue curve), aligned with the theoretical results of the simulations (orange curve). In spite of the fact that the intensity is not the expected one, the results are very promising and indicate that EIT occurs in this electromagnetic metamaterial due to the response that is shown above and as it was analyzed previously in section 5.1.

The decreased intensity of the transmission is something that was expected because of the significant losses that take place not only during the development of the sample, but also in the measurements. From experimental aspect, there are two main parameters that have to be taken into consideration that are able to explain the existence of high losses. First, regarding to the silver coating, there are losses due to the silver nanoparticles that are attached on the polymerized material. As it is shown in Figure 5.4.2 in SEM images, even though the fabrication quality is quite satisfying, silver nanoparticles are like small rocks growing at the surface of the fabricated structure creating a rough surface. This is getting more intense as the metalization process is repeated multiple times resulting in decreased intensity of the signal that reaches the detector. Also, as it can be observed from the SEM images (Figure 5.4.2) the repeated metalazation process forms a very thin layer of silver nanoparticles (roughly 5 $nm$) on the substrate because of the aggregation of the particles. This can cause, in small amount regarding to the wavelength, additional losses to the electric signal that is finally detected. These two parameters that are originating from the silver coating,

are capable of reducing the electric signal and subsequently resulting in lower intensity compared to the expected one.

Second parameter from the experimental aspect, losses are also included because of the sensitivity of the measurements system. As it was analyzed in section 5.4, the characterization of the sample relies on the photoconductive mechanism. This is a sensitive detection mechanism of electric signals and strongly depending on environmental conditions such as humidity and temperature. Thus, it is reasonable to get losses just from the characterization procedure. Also, regarding to the placement of the sample, this is done by guiding it by hand resulting in displacement errors due to the fact that the incident wave cannot be 100% aligned with the sample. Last but not least, an important parameter for the characterization is the silicon substrate that was used. Since the detection of the signal relies on the varying response of the electric current that is stored in the detector, a high resistivity Silicon substrate is required. As it can be observed from the experimental results in Figure 5.5.1, there is a strong absorption of the signal (approximately 25%) in the frequency region from 0.5-1 THz, that indicates that the substrate "blocks" a small part of the signal. Thus, the signal that reaches the detector is lower from the initial due to the absorption of the substrate and the interference of the signal that takes place in the connection point of the fabricated structure with the substrate. This can be possibly solved in a straightforward way, substituting the substrate with a higher-resistivity one.

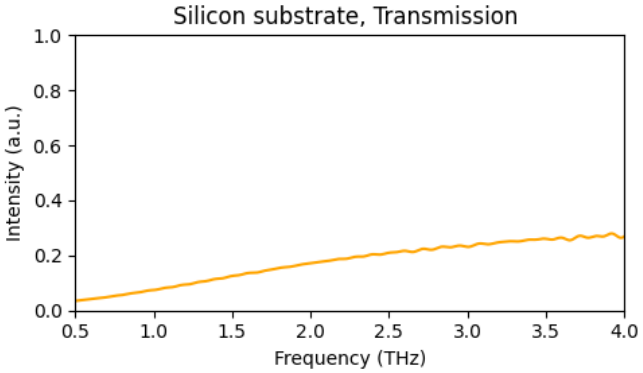


Figure 5.5.2: Transmission measured from the silicon substrate.

Besides the systematic errors that occur during the characterization, there is also a physical parameter introduced in the experimental results. Transmission losses result in lower signals than the math would indicate [112]. In the sharp peak of transmission, the losses are proportional to a factor of $\propto Im(\epsilon)|E|^2$, where $Im(\epsilon)$ is the imaginary part of the electrical permittivity which is proportional to the real part of conductivity ($Re(\sigma)$) and $E$ relies for local electric field [113] that is concentrated in the pillars due to the coupling resonances that take place (see Figure 5.1.6 for the surface current distribution in the resonance's frequency where the electric field results in concentration of current in the base of the pillars). Thus, the concentrated local field reaches high values of $|E|$ resulting in high losses in transmission spectra, while at the same time conductivity of the chosen silver cause also losses due to the $Im(\epsilon)$ factor. As a result there are losses from physical aspect that have to be taken into consideration and can potentially explain the reduced signal's intensity at the experimental results.

In conclusion, the suggested low THz metamaterial electromagnetic response seems to align with the mathematical predictions in basic operational characteristics. Thus, this provides a strong indication that EIT can occur in such structure in the THz frequency regime around 2 THz. Although, from the experimental results the intensity of the transmission does not provide optimized results due to multiple loss factors that are included in the development and characterization of the sample. These losses are not originating only from systematic errors, but also from transmission losses that occur physically in this kind of systems, especially from the concentrated local fields as it was briefly explained above. Moreover, as the transmission properties depend strongly on the polarization and the incident field, this complicates the interpretation of experimental and numerical data when electromagnetic metamaterials are characterized for their transparency. Further experimental demonstration is required, with main focus to be on eliminating the systematic errors, to make the experimental results come to an agreement as much as possible with the theoretical predictions and reach to a better result regarding the intensity of the transmission and subsequently to the transparency of the metasurface.

# 6 Other applications combining metamaterials and 2PP technology

Two photon polymerization technique has been proved to be one of the strongest tools to fabricate structures in micro and nano scales. The potential applications generated combining this fabrication technique with metamaterial's growing technology are countless. The easy scaling process in 2PP gives the ability to fabricate structures that can operate in a wide range of frequencies. Some potential applications from fabricated structures that -theoretically- operates in visible, mid IR and microwave wavelengths will be presented below. Also, a potential fabrication method for creation of ultra-high resolution metasurfaces with smooth surface that can provide high Q-factor resonances will be highlighted. The existence of smooth surfaces in fabricated structures is very important to avoid losses from scattering, and here 2PP technology overcomes the fabrication issues of conventional lithography techniques.

## 6.1 Photonic crystals metamaterials for biosensing

Photonic crystals (PCs) are periodic structures composed of periodic elements with different refractive index , high and low respectively. These exotic structures are indicated in order to manipulate light due to the periodicity that they exhibit, which is proportional to the wavelength of light in the band-gap. Depending on the period, certain wavelengths are allowed to pass from the crystal while the rest are forbidden to propagate through the medium [114]. Thus, it operates as an artificial atom with energy band where allowed and forbidden states inside the band-gap takes place, like nature's elements.

First identification of the photonic crystals and the way they operate came in 1987 by E. Yablonovitch [115] and S. John [116], where they demonstrate the way a periodic slab of different refractive index materials can manipulate light. After that, research and publications about photonic crystals have been increased impressively. The application that PCs takes place are countless since they can significantly enhance the interactions between light and matter just by tuning the periodicity and the refractive index of the layered geometry.

A lot of novel research has been conducted the last decades for manipulation of light. Since light acts as a wave, PCs have been used for several applications. K. M. Ho, C. T. Chan, and C. M. Soukoulis [117] proved the existence of a photonic gap in periodic dielectric structures "solving Maxwell's equations for the propagation of electromagnetic waves in a periodic lattice of dielectric spheres in a uniform dielectric background". This was the first indication that 3D structures with refractive-index contrasts can provide photonic band-gap when the elements are arranged in diamond lattice structure. After, E. Yablonovitch et al. [118] came up with the experimental existence of photonic gaps using non-spherical elements in 3D structures with a face-centered-cubic (fcc) lattice. After that, woodpiles geometries have been commonly used for the fabrication of 3D PCs, where rods with diameter of a few nanometers are periodically arranged in fcc lattice, where lattice constant **a** now presents the periodicity. In order to manipulate optical wavelengths microfabrication can be very challenging to achieve the resolution of tens of nanometers, which was solved using 2PP technology.

Initially, the PCs were made of periodically arranged dielectric elements with periodicity of a few hundreds of nanometers in order to manipulate visible light. But as the period decreases, the low ratio of refractive index through the dielectric material and air causes interactions that lead to losses and not clear photonic band-gaps, making the medium operating as a bulk material. In order to overcome this issue at optical wavelengths where small periodicity is mandatory, the use of metallic elements gave the solution [119]. Using metallic PCs cause stronger interactions while at these frequencies metals are operating as perfect reflectors with low absorption, with higher ratio of refractive index through the two mediums, leading to low losses systems which cannot be observed at dielectric PCs. Some of the applications that metallic PCs have been used are filters [120], different kind of sensors [121], high resolution imaging [122], as well as energy harvesting and photovoltaics since they can operate at optical regime with high efficiency [123].

Since in these structures electromagnetic interference is very strong and detection of changes in the system is quite sensitive, metallic PCs lately have been also used for the development of ultra-sensitive chemical and bio sensors [124]. In 2009, Kabashin et al. [125] made a major breakthrough in sensing technology where they used plasmonic nanorod metamaterial in 2

dimensions for biosensing. In consequence of the metallic PCs properties, nanostructured metal-surfaces can detect minor molecular-binding events, since "localized plasmons demonstrate orders of magnitude lower sensitivity compared to modern nanobiotechnology architectures". Using plasmonic metamaterials this characteristic can be improved a lot since metamaterial is able to provide an enhanced sensitivity to refractive index variations of the medium between the rods. An issue that emerges is that some biological systems need higher sensitivity in order to detect the response when they interact with electromagnetic waves.

Later, A.I. Aristov, M. Manousidaki et al. [11] conducted a research where this high-sensitive biosensing behaviour was further improved, using 3D plasmonic metamaterials. Inserting a third dimension to the geometry generates more plasmonic states that can be excited and wider photonic gaps. This plasmonic crystal can exploit a delocalized plasmonic mode which results in extremely high spectral sensitivity, measured as nm or phase per refractive index unit (RIU). Molecules-binding interactions can be detected in real-time using the excitation of plasmons from the plasmonic metamaterial while they cause changing in the reflection. Using this, study of biomolecular binding events can be studied through plasmonic transduction which is caused by the difference of the refractive index between molecules and aqua solutions. When a detection occurs, a big rise of the phase can be observed indicating that there is interaction between the molecules providing the sensing application.

### 6.1.1 Plasmonic metamaterial for tissue sensing

In collaboration with professor A. Kabashin (Aix Marseille University), a novel metallic photonic crystal with active plasmonic resonators has been developed and fabricated and remains to be measured for the plasmonic response and the sensitivity that can provide. The aim of the project is to provide an ultra-high sensitive detector which will be used as biomedical tool to detect breast cancer cells, using the plasmonic excitation with high phase transition in the electromagnetic field as an indication that a molecular event takes place at the targeted tissue. For the purpose of this, a photonic crystal-based architecture was designed in the same way as a woodpile geometry [117]. The woodpile photonic crystal geometry is composed of layers of one-dimension rods with a stacking sequence that repeats itself every four layers.

In each layer, the rods are parallel to each other, with a distance within them to be defined as **a** which is also the period of the crystal. The adjacent layers are rotated by $90^o$. In order to achieve the fcc unit cell with a basis of two rods, each layer is shifted proportional to the previous layer by $a/2$. Scheme of the woodpile geometry is shown in Figure 6.1.1.1.

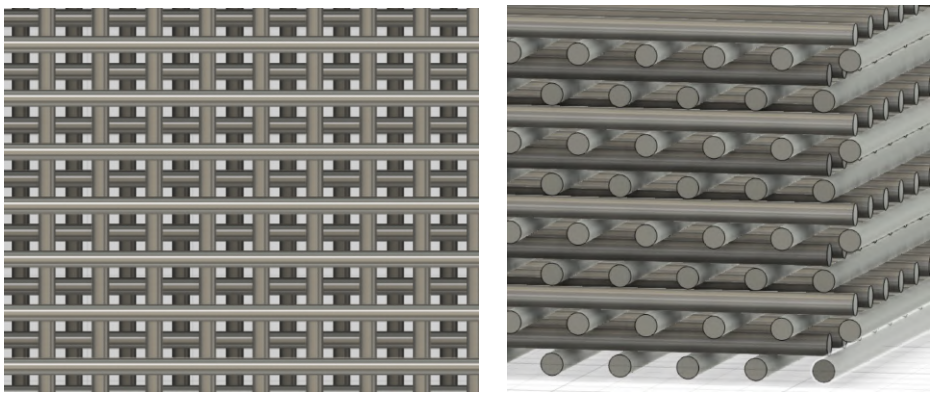

Figure 6.1.1.1: CAD image of the photonic crystal's geometry (top view - side view).

### 6.1.2 Fabrication of 3D metallic plasmonic metamaterial

For the fabrication of the plasmonic metamaterial, the metal-binding photoresist SZ2080 with 30% DMAEMA was used (synthesis in section 3.2 of the thesis). The experimental setup employed for the fabrication is a Nano-cube setup (similar to the Galvo setup in section 3.3 of the thesis). The irradiation source is a fiber pulsed fs laser operating at 780nm which is focused inside the photopolymer using a high numerical aperture microscope objective lens (100x, N.A.=1.4, Zeiss, Plan Apochromat) witch operates with oil immersion providing spacial resolution of a few nm [126]. The laser beam, in comparison with the Galvo setup, is now in a fixed position and all x-y-z movements are performed by three piezoelectric stages (Physik Instrumente M-110.1DG, 50nm minimum incremental motion), making it suitable for the fabrication of structures at scale of optical wavelengths.

The plasmonic crystal metamaterial is designed to have a period of 650 nm and the thickness (diameter) of every rod is in average 250 nm. The size of

the plasmonic crystal is set at 50 $\mu m$. For the fabrication, the average laser power that it was used was 2.5 mW, while the scanning speed of the printing process was set to be 20 $\mu m/s$. For this experiment, the photonic crystal consisted of 7 unit cells (each unit cell has 4 layers, as it was mentioned before).

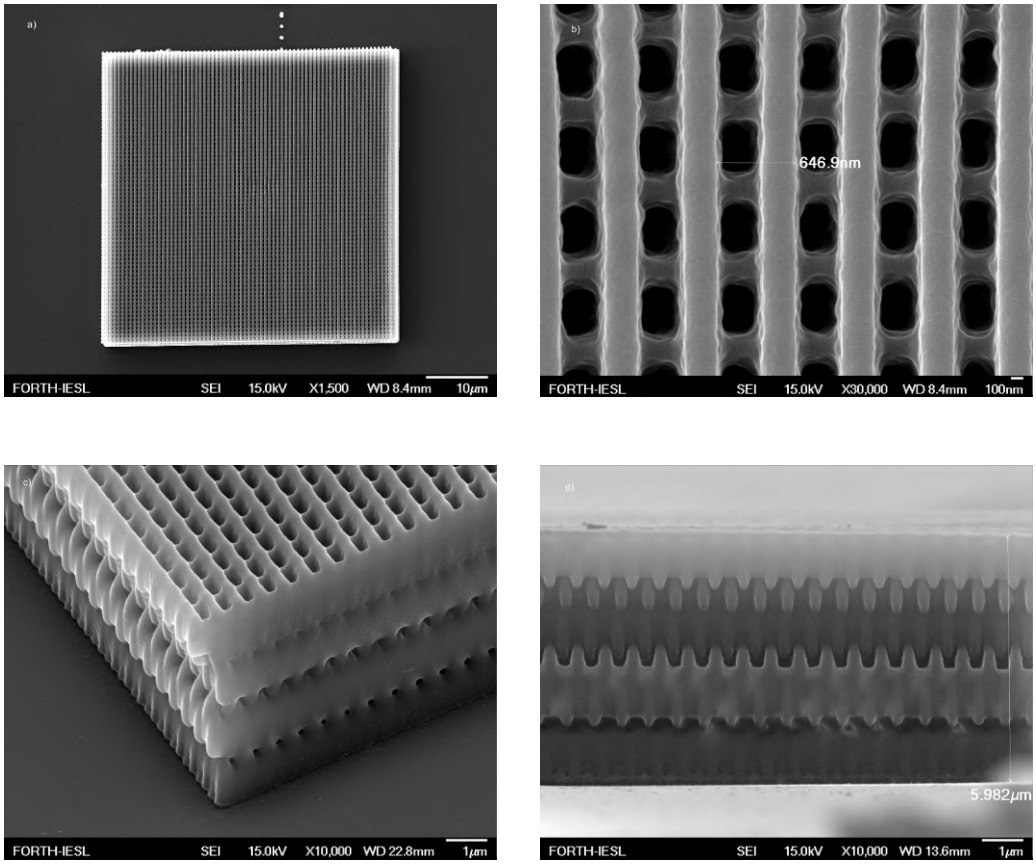


Figure 6.1.2.1: Scanning electron microscopy (SEM) images of the plasmonic metamaterial before the metallization, a) top view, b) top view magnified exploiting the resolution of the 2PP technique, c) tilted view, d) side view.

From the SEM images (Figure 6.1.2.1) it was measured that the period of the fabricated structure is almost 647 nm (very close to the designed one) and the diameter of the rod in average is 270 nm. The high percentage of DMAEMA in the photoresist cause the material to look like melting at the

edges of the structure (Figure 6.1.2.1 c,d) but this does not cause any issue to the performance of the medium.

After the fabrication process, a post-process must take place for the plasmonic metamaterial to become metallic in order to obtain the desired sensitivity. The protocol that is followed is the same as in subsection 5.3. For the results, ellipsometry measurements are going to be conducted to see the size of the change in polarization that trigger the sensitivity when light reflects or transmits from the crystal [127]. In ellipsometry, the polarization change is represented by the changes in amplitude $\Psi$ (ratio of amplitude reflection coefficients for light polarization parallel, p, and perpendicular, s, to the plane of incidence) as well as the phase difference $\Delta$ between the s- and p- components [11]. It is strongly depends on the optical properties that the material exhibits and thickness of the medium. High scale of changes in these values indicates strong sensitivity in order to detect molecular interactions under specific circumstances. The results will be compared with simulation results they are will conducted using FDTD method.

## 6.2 Mid-Infrared (MIR) metamaterial for sensing applications

Mid-IR optical gas sensors generated from electromagnetic metamaterials systems play a vital role in atmospheric research. Sensitivity and tunability that electromagnetic metamaterials can provide are the most important characteristics that have to be taken in consideration for the advance and development of novel metamaterial structures that can operate as gas sensors, especially in Mid-IR regime where the atmospheric window exists and greenhouse gases radiate in high intensity [128]. Also, high selectivity that can be achieved through meta-structures provides a strong tool for sensing different gases with high accuracy, since each molecule has a specific radiation signature. Developing metamaterials for gas sensing can also deal with issues such as power consumption and large volume devices , since down scaling in size can be easily achieved and result in next generation gas sensors that will be small in size and controllable compared to conventional devices.

### 6.2.1 High absorption mid-IR metamaterial

The central axis for the development of the novel metamaterial structure is to exhibit high absorption characteristics in specific wavelengths. In this case, the study is focused on the limit of MIR region, from 10-15 THz (or 20-30 $\mu m$ in wavelength scale). In these frequencies greenhouse gases such as carbon dioxide ($CO_2$) and water vapor ($H_20$) present an intense footprint in the radiation they emit [129]. This is something that has to be taken in advantage in order to create a small, light-weight and with low-power consumption sensor operating at these specific wavelengths.

Manipulation of THz wave propagation in layered media can create fertile conditions for the absorption of radiation. More specifically, fabricated metallic unit cell structures that are periodically arranged can change the emission and absorption spectra as a results of surface waves coupled to the external radiation [130]. These micro-resonators can also create narrow-band absorption for specific wavelengths due to thermal radiation emission [131].

Gas molecules due to the vibrations that take place and the interference with the atmospheric radiation have the ability to absorb and emit radiation at specific wavelengths. In the atmospheric window, gases that emit

with high intensity radiation such as $CO_2$ and water vapor can be detected if the artificial designed medium absorbs at the same wavelength. This kind of sensors is based on the interaction of light with gas molecules and can offer high sensitivity [132]. The idea of optical gas sensors rely on absorption spectroscopy, which is calculated through reflection and transmission coefficients, where a gas can be detected by measuring the light it absorbs in specific wavelengths [133]. The above mentioned molecules have characteristic absorption lines in the MIR spectral region which is expanding at 20-30 $\mu m$. The absorption spectra for major greenhouse gases in Earth's atmosphere is presented below.

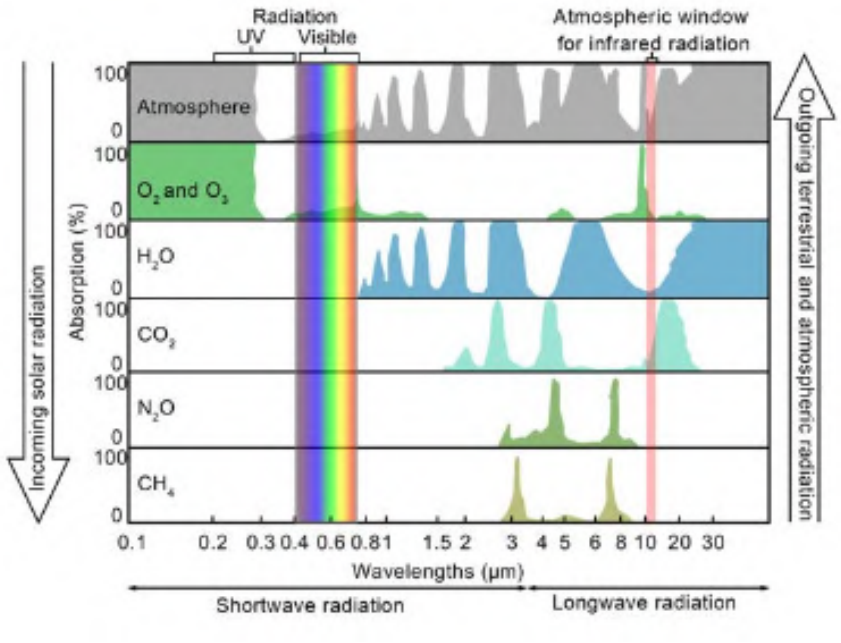


Figure 6.2.1.1: Absorption spectrum of major greenhouse gases in atmosphere. Obtained from [134].

From Figure 6.2.1.1 it is observed that $CO_2$ and water vapor ($H_2O$) have a strong absorption and emission of radiation above the atmospheric window for infrared radiation. In order to create the MIR gas sensor, the medium has to absorbs strongly at the same wavelegth, approximatelly at 20-22 $\mu m$ which is equal to a frequency of 13 THz.

### 6.2.2 Design and fabrication of the gas sensor

The proposed metamaterial design for gas sensing applications is a complex "$2D+1$" metamaterial structure. CAD design is presebelow. The dimensions that are included are: a=20 $\mu m$, b=16 $\mu m$, c=6 $\mu m$, $h_1$=4 $\mu m$, $h_2$=4 $\mu m$, $w_1$=1 $\mu m$, $w_2$=2 $\mu m$, $w_3$=3 $\mu m$.

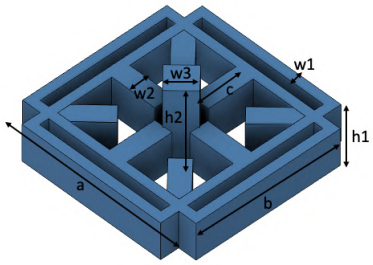


Figure 6.2.2.1: CAD design of the metamaterial absorber.

Simulations where done in order to find the optimized geometric parameters, following the same protocol as it was described in section 4.1 of the thesis. Now, the range of the excitation signal was set to be 10-15 THz. The material that was used is Silver, which provides low losses at these frequencies. The results of the simulation for the TM(0,0) mode are presented below.

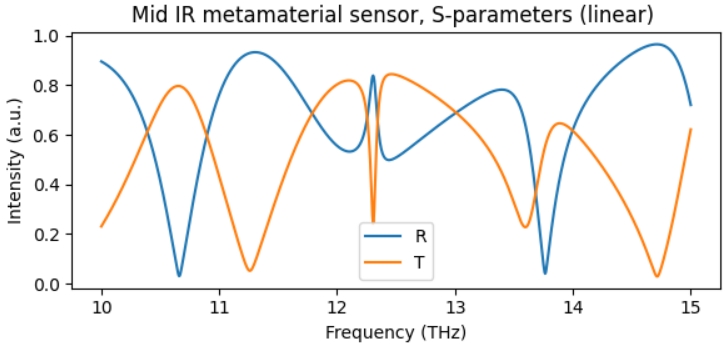


Figure 6.2.2.2: Simulation results for reflection and transmission.

Scheme of the absolute value of current generated from the radiation that propagates through the medium is also presented below. It is clear that the generated currents are very strong for the proposed geometry.

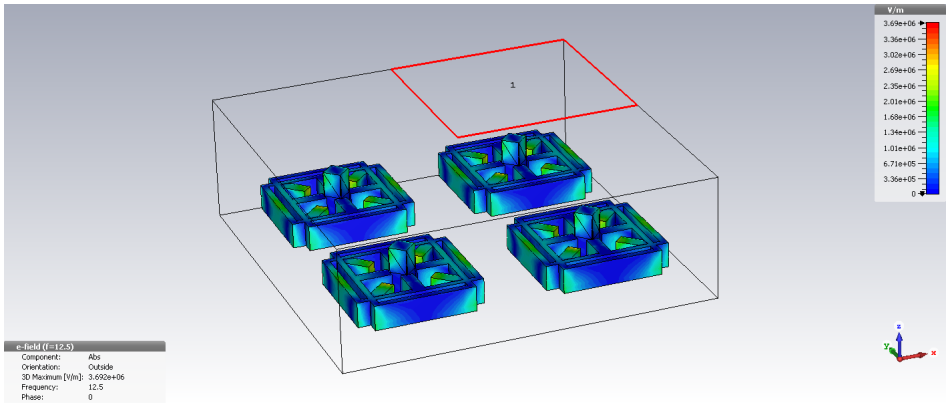


Figure 6.2.2.3: Absolute value of surface currents induced in metamaterial absorber by 12.5 THz plane wave.

In order to observe the response of the proposed structure in the wavelengths that molecules mentioned before emit, the absorption spectrum has to be calculated using equation 2.1.10.f, depending on the results of Figure 6.2.2.3. High absorption will indicate that in this region the device can detect signals from the radiation of the gases. The results are presented below.

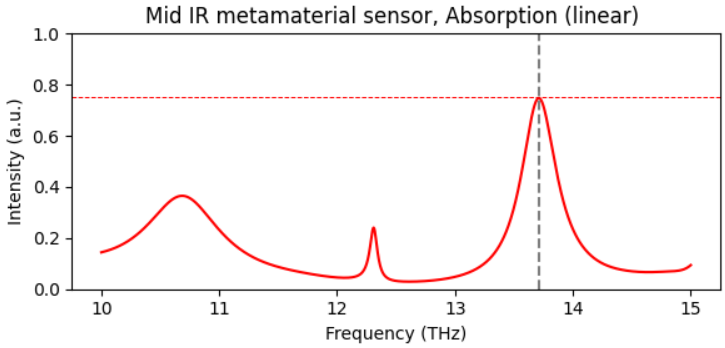


Figure 6.2.2.4: Calculated results of absorption spectrum for the sensor.

Taking into consideration the results of Figure 6.2.2.4 for the absorption spectrum, a near-perfect absorption is observed at 13.7 THz (21 $\mu m$ in wavelength scale), where it reaches a percentage of almost 80%. The wavelength that this metallic metamaterial is able to absorb in high percentage indicates very promising result for detection of greenhouse gases that were discussed above using light-weight and low-consumption power device that can operate with high sensitivity for specific wavelengths.

Moreover, using silver instead of PEC was not an arbitrary selection. Ag nanoparticles have been reported to show a very good absorption performance in MIR frequencies [135], providing very low losses which are critical for the detection of sensitive and wavelength selective signals such as the radiation from gas molecules. For comparison, simulations were repeated using the same parameters for the system but now using PEC material to highlight the difference in absorption spectra between the two materials. The results of the calculated absorption for the two systems are presented below.

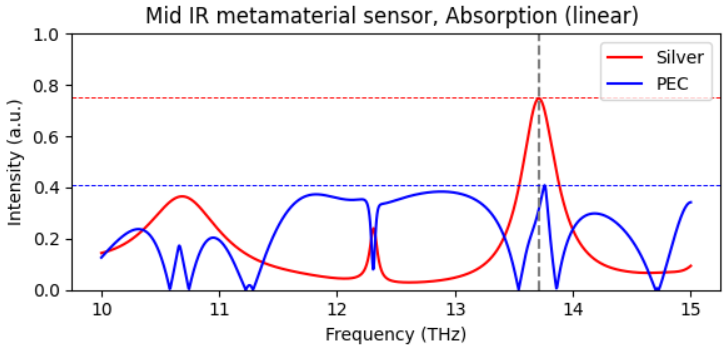


Figure 6.2.2.5: Calculated results of absorption spectrum for the sensor; red line with silver, blue line with PEC.

From the results in Figure 6.2.2.5 it can highlighted that using a polymer provides in the same frequency region the half absorption than using a silver medium. Also, using PEC does not provide clear absorption peaks making the device less sensitive. As for the complete application, this metamatateterial could be fabricated on silicon substrate (as a semiconductor) with high conductivity and then place in an electrical circuit that will provide a small

voltage supply in order to stimulate the absorption performance of the material [136] and detect the existence of the gases depending on the intensity of the absorption spectrum that is obtained behind the device.

For the fabrication of the metallic metamaterial, 2PP setup with Galvo scanner was used that is presented in section 3.3 of the thesis. A 40x objective lens (Zeiss, Plan-Apochromat with N.A.=0.95) was used to achieve the details in the geometry of the design. The average laser power was set at 200 mW, while the scanning speed of the printing process was 2000 $mm/s$. Images from SEM are presented below.

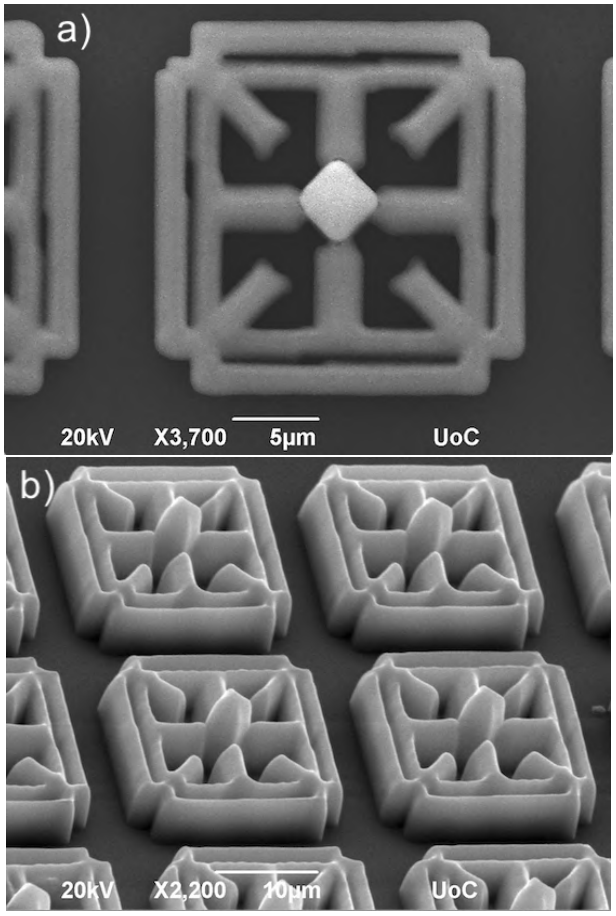


Figure 6.2.2.6: SEM images of the fabricated metamaterial, (a) top view, (b) tilted view.

The proposed near-unity narrow-band terahertz absorber is seized of considerable potential in the application of gas sensing due to the sensitivity the absorption peak provides in Figure 6.2.2.4. In addition, one of the necessary requirements for metamaterials absorbers to get near-unity absorption, is the impedance matching [137]. The effective impedance of the perfect absorber is evaluated by [138]; $Z(\omega) = \sqrt{\frac{(1+S_{11}(\omega))^2 - S_{21}(\omega)^2}{(1-S_{11}(\omega))^2 - S_{21}(\omega)^2}}$, where $S_{11}$ and $S_{21}$ are the reflectance and transmission coefficients, respectively. Calculated effective impedance for the MIR absorber metamaterial is shown in Figure 6.2.2.7.

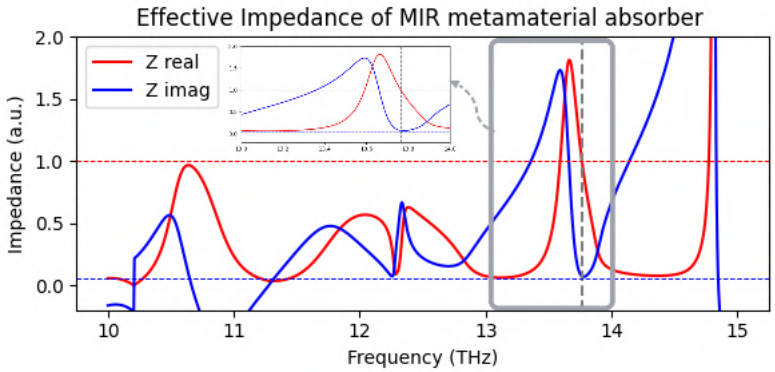


Figure 6.2.2.6: Real and imaginary part of the effective impedance of the absorption peak.

At the resonance in Figure 6.2.2.6 is observed that the impedance is matching, since the real part of the equivalent impedance is near to the unity, while the imaginary part is near zero. Thus, the proposed MIR metamaterial absorber achieves the impedance matching with the impedance of the free space at the resonant frequency (where real part equals to one and imaginary part equals to zero), resulting in high absorption effect [139].

## 6.3 Far-Infrared (FIR) metamaterial for energy harvesting

The exotic property of scaling the size of metamaterials has been a usefull tool to fabricate structures that can operate in different frequency regimes using the same architecture. Re-size and tuning the dimensions of the meta-atoms can provide strong electromagnetic interactions that lead to many applications in different wavelengths. One of them, that is essential for the development of high efficiency renewable energy sources, is metamaterials absorbing at FIR regime.

### 6.3.1 High absorption from FIR metamaterial

FIR regime refers to wavelengths that range from 15 $\mu m$ up to 1 mm (in frequency scale from 20 THz to 300 GHz) [140]. This specific region is highly interesting for energy harvesting applications since absorption of far infrared wavelengths, especially in visible light, can be very challenging. Research is focused mainly on the development of devices for efficient solar energy harvesting, such as photo-voltaic based solar cells. These devices have been proved to have fundamental limitations based on the physical mechanisms that convert light into voltage. Theoretical limits of photo-voltaic systems showed that the maximum efficiency that a photo-voltaic system can reach is around 43% using very complex and unstable systems, while in lab conditions using the most common semiconductors, Si, it reaches 25% [141]. Thus, developing light-weight and high efficiency absorption devices using metamaterials is major interest in the field of improving renewable energy sources.

Most of the solar energy is reflected and returns back in atmosphere in a photo-voltaic system due to the limitation in absorption spectrum that conventional materials exhibit. Thus, artificial made materials such as metamaterials can imporve this performance. Adding an FIR absorption device in a photo-voltaic system, a high percentage of the reflected radiation can be absorbed before it returns and lost in atmosphere. The idea is to create a compact device that will absorb one part of the wasted light and resulting in the increase of the efficiency of solar panel systems. Silicon and other commonly used materials in solar cells can absorb wavelengths until yellow (approx. 570 nm), reflecting lower wavelengths such as green (approx. 500

nm) and blue (approx. 460 nm) [142]. These two reflected wavelengths can excite infrared photons that enhance FIR radiation [143] providing fertile conditions for the development of a metamaterial selective absorption geometry that will absorb the wavelengths that cannot be absorbed from Si solar cell. Then, more photons are going to be absorbed from the total surface (solar cell including the metamaterial geometry), providing higher total absorption of light and resulting in increased solar cell efficiency. This means that more voltage can be generated from the same amount of incident sunlight. Also, manipulating high energy blue light can also lead to even higher power efficiency in solar panels.

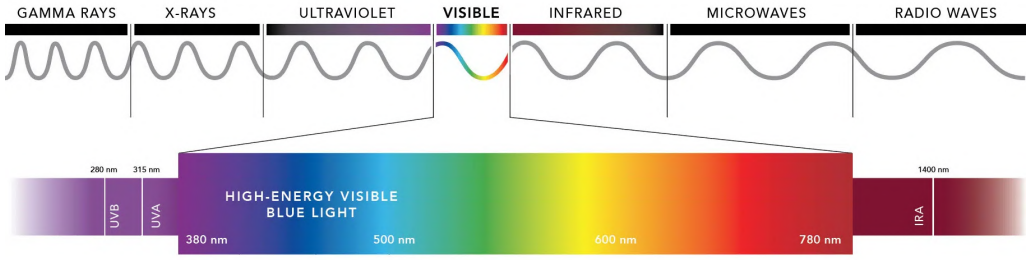


Figure 6.3.1.1: The visible spectrum in wavelength scale (Light).

### 6.3.2 Fabrication and development of FIR absorber

Electromagnetic absorbers are artificially made designs that can inhibit the reflection and transmission properties of the electromagnetic radiation simultaneously. The design is based on SRR geometry [6] and the simulations were conducted in the novel research of M. R. AlShareef and O. M. Ramahi in 2013 [144]. Electromagnetical small resonators based on the SRR classic design can produce "electrically small resonators to harvest microwaves energy to the infrared frequency regime". The absorbed power can be converted to electric signal providing a triggering motion to the electrons in the substrate which has to be a semiconductor, collecting the FIR radiation. The modeled design was composed of a metallic SRR with permittivity dispersion to correspond with the targeting frequency of approximately 450 GHz.

For the design, under the metallic SRR the substrate that was used is Silicon in order to provide semiconducting properties for triggering electron motion and conversion of light to electric energy. The Silicon substrate also it is not able to absorb the blue and green wavelength's radiation, guaranteeing that the loses of the total system will be minor. The metallic metamaterial will be covered with Silver (Ag) in order to provide the metallic properties that are needed and follow the Drude model complex dielectric dispersion [145]. Silver exhibits low absorption losses compared to other metals and can provide a dielectric permittivity constant [146] that shows dispersion from millimiter until UV waves and is commonly used as a layer in solar cell technology for its characteristics.

Advance of 2PP technology give the opportunity to fabricate this kind of complex metallic components on silicon with high accuracy avoiding diformations compared to conventional lithographic techniques and using a post-process electroless silver plating process to compose a selective silver design with silicon substrate. The proposed silver design is presented below, with dimensions a=40 $\mu m$, b=20 $\mu m$, c=10 $\mu m$, d=15 $\mu m$ and thickness h=10 $\mu m$.

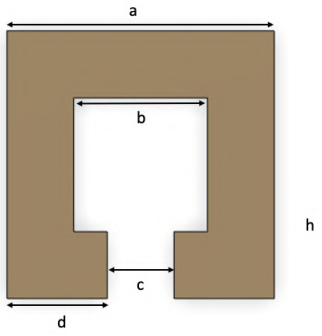


Figure 6.3.2.1: CAD design of the proposed SRR FIR absorber.

The simulations were done by M. R. AlShareef to verify that this specific geometry has the potential to harvest energy measuring reflection and transmission coefficients using the FDTD method, following the same protocol that it was discussed on chapter 4.1 of the present thesis. The simulations

were also done for symmetric array of SRR and asymmetric array. Asymmetric array resulted in higher efficiency than the symmetric array. The optimized array is obtained by rotating the SRR across the y plane to create deformations that enhancing the electromagnetic response of metamaterials, as it was discussed thoroughly on chapter 4. This occurs due to capacitive and inductive mutual coupling between adjacent cells at which optimal energy harvesting is achieved. Adjacent currents induce a stronger electric field across the gap of the SRR, providing increased absorbed power through the medium. The power efficiency, that is calculated by the ratio of total infrared power that strikes the medium to the maximum infrared power received by the SRR using a resistive load to obtain the difference, is exhibited in Figure 6.3.2.2.

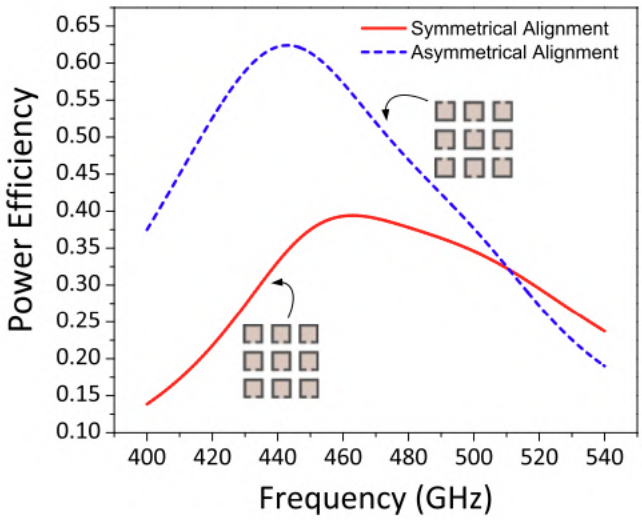


Figure 6.3.2.2: Simulation results of power efficiencies of symmetric and asymmetric SRR absorber loaded by a 2kΩ resistance, obtained from [144].

For the fabrication of the asymmetric SRR array, Galvo setup using 2PP technique was used as it was presented in chapter 3.3 of the thesis. The photosensitive material that was used is SZ2080 with 30% DMAEMA (chapter 3.2), placed on Silicon substrate. In order to get the metallic properties that are mandatory for FIR absorption, the sample was further processed following the protocol for metallization with silver as it was analyzed in chapter

5.3. Scheme of the array (Figure 6.3.2.3) and SEM images of the fabricated structure (Figure 6.3.2.4) are presented below.

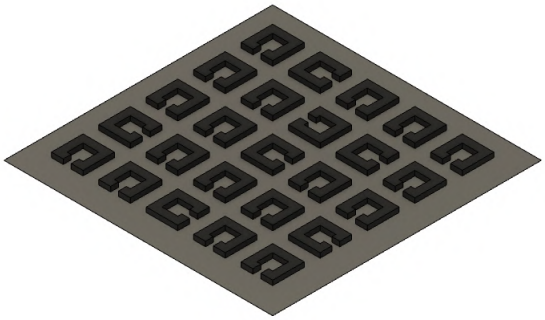

Figure 6.3.2.3: Scheme of the proposed design with silver SRR, placed on Silicon substrate.

The structure fabricated using Zeiss 20X Objective, Plan-Apochromat (0.8 NA), with the average laser power that it was used was 190 mW and the scanning speed of the printing process was set to be 1500 $\mu m/s$.

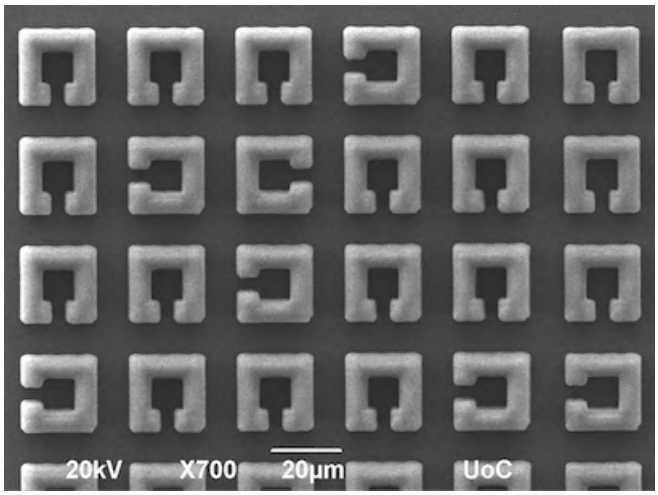


Figure 6.3.2.4: SEM image of the fabricated SRR, exploiting the resolution that 2PP printint technique can provide.

# 7 Conclusions

## 7.1 Synopsis of the thesis

Electromagnetic metamaterials changed the way we understand nature. With the rapid growth of technology, metamaterials started to be a topic of high interest for researchers in the field of photonics, nanotechnology, telecommunications and sensors just to name a few. The experimental obstacles of the poor fabrication techniques started to overcome, especially in the last decade providing high impact accomplished not only in research, but in industry also. More especially, metamaterials provide the opportunity to manipulate wavelengths of light that cannot be done using nature's materials which are limited by their electromagnetic characteristics such as electric permittivity and magnetic permeability. Using specific architecture for the meta-atom, metamaterials are acting like nature's materials with tunable properties, providing a straightforward way to manipulate the complete electromagnetic spectrum. In the present thesis, the metamaterials that were studied focused on low THz frequencies, which is a band that nature's elements exhibit limitations in their electromagnetic response. Since the architecture of the meta-atom has crucial impact on the response and behaviour of the material, the suitable technique that was used for the fabrication of the meta-atoms was 2PP, which is a real 3D printing technique providing high resolution and a large variety of materials.

In the first part of the work (Chapter 2), the theoretical background was briefly explained in order to connect classical electromagnetism, from Maxwell's equations, with nowadays complex electromagnetic media such as metamaterials. After, the FDTD method, that was used for the simulations of the metamaterials to find the optimize response and architecture of the meta-atom, was analyzed to highlight the importance of combining theoretical calculations with real life experiments and finally 2PP was explained from theoretical aspect.

In the next chapter of the thesis, the suitable photosensitive materials that was used for fabrication of the structures were analyzed, including the synthesis of the material and the sample handling before the polymerization process. After, the fabrication process was further analyzed presenting the 2PP setup and the fabrication steps.

In order to introduce the main research of the thesis, in Chapter 4 an introduction in low THz metamaterials were done, combining theoretical models with the fabrication process, mathematical results and SEM images of the fabricated suggested structures. Starting from a classical cross-shaped SRR design, the electromagnetic response was calculated. After, an asymmetry was included to the design to observe how the broken symmetry will result to different behaviour of the material. Finally, a doubly-symmetry was included to observe that in broken symmetries the electromagnetic response is enhanced compared to plain geometries or symmetric architectures.

In Chapter 5, the complete study and development of a suggested electromagnetic metamaterial with high transmission response in low THz regime was presented. First, the idea behind the design was analyzed. After, the fabrication process and the results of the fabricated structures were exhibited through SEM images. Then, a post-process state of the art electroless silver coating method was studied and operated in the fabricated structures, in order to get metallic structure with high conductivity so it would be suitable for characterization in low THz regime, benefit from the physical mechanism of photoconductivity. Finally, the characterization and the theoretical predictions of the fabricated sample were presented. Theory and experiment come in alignment in the aspect of the resonance frequency, but not in the intensity. The extensive losses that occur during the post-process metalization method, as well as physical parameters that are induced in the characterization methods, result in significant losses in the experimental results. Although, the results are quite satisfying taking everything into account, providing strong indication that the suggested metamaterial can enhance the Electromagnetically Induced Transparency (EIT) at the frequency of 2 THz. Further experiments can be operated, trying to avoid some systematic errors that are included in the whole procedure, from the fabrication until the characterization of the metamaterial.

In the final chapter, a demonstration of the capabilities that 2PP and metamaterials combined can provide was done in a variety of frequency bands. Starting from NIR regime, developing a photonic crystal for promising biosensing applications, to a gas sensor metamaterial at MIR regime and finally in a promising energy harvesting metamaterial operating at FIR regime that can enhance photovoltaics efficiency and performance.

## 7.2 Future plans

The main aim of this work was to design functional metamaterials that can enhance the electromagnetic response in THz regime, where nature's elements shows limitations. One of my major future's plans is to fabricate a more efficient sample and get optimal results which will result in better transparency of the metasurface.

Some of my side projects had to deal with metamaterials in varying frequency regimes, that theoretically have some interesting characteristics. Thus, I would like to prove experimentally the behaviour of the FIR metamaterial for energy harvesting, as well as the MIR metamaterial for gas sensing applications. Both of them have a high impact in scientific community since they are relevant with the environment and renewable sources of energy, a challenging deal we have to face up with in order to keep our planet viable for next generations.

Last but not least, metamaterials are very interesting to investigate, but research means that you can always learn something new and this is something I would like also to do.

# References


1. Mahon, B. How Maxwell's equations came to light. *Nature Photonics* **9,** 2–4. https://doi.org/10.1038/nphoton.2014.306 (Jan. 1, 2015).
2. Pendry, J. B. Negative Refraction Makes a Perfect Lens. *Phys. Rev. Lett.* **85,** 3966–3969. https://link.aps.org/doi/10.1103/PhysRevLett.85.3966 (18 Oct. 2000).
3. Ferguson, B. & Zhang, X.-C. Materials for terahertz science and technology. *Nature Materials* **1,** 26–33. https://doi.org/10.1038/nmat708 (2002).
4. Grimberg, R. Electromagnetic metamaterials. *Materials Science and Engineering: B* **178.** Selected Papers from the 9th International Conference on Physics of Advanced Materials (ICPAM9), 1285–1295. ISSN: 0921-5107. https://www.sciencedirect.com/science/article/pii/S0921510713001335 (2013).
5. Veselago, V. G. & Narimanov, E. E. The left hand of brightness: past, present and future of negative index materials. *Nature Materials* **5,** 759–762. https://doi.org/10.1038/nmat1746 (2006).
6. Smith, D. R., Pendry, J. B. & Wiltshire, M. C. K. Metamaterials and Negative Refractive Index. *Science* **305,** 788–792. eprint: https://www.science.org/doi/pdf/10.1126/science.1096796. https://www.science.org/doi/abs/10.1126/science.1096796 (2004).
7. Wuestner, S., Pusch, A., Tsakmakidis, K. L., Hamm, J. M. & Hess, O. Overcoming Losses with Gain in a Negative Refractive Index Metamaterial. *Phys. Rev. Lett.* **105,** 127401. https://link.aps.org/doi/10.1103/PhysRevLett.105.127401 (12 Sept. 2010).
8. Jaksic, Z., Dalarsson, N. & Maksimovic, M. Negative Refractive Index Metamaterials: Principles and Applications. *Microwave Review* **12** (Apr. 2006).
9. Wang, B., Zhou, J., Koschny, T., Kafesaki, M. & Soukoulis, C. M. Chiral metamaterials: simulations and experiments. *Journal of Optics A: Pure and Applied Optics* **11,** 114003. https://dx.doi.org/10.1088/1464-4258/11/11/114003 (Sept. 2009).

10. Smith, D. R., Padilla, W. J., Vier, D. C., Nemat-Nasser, S. C. & Schultz, S. Composite Medium with Simultaneously Negative Permeability and Permittivity. *Phys. Rev. Lett.* **84,** 4184–4187. https://link.aps.org/doi/10.1103/PhysRevLett.84.4184 (18 May 2000).

11. Aristov, A. I. *et al.* 3D plasmonic crystal metamaterials for ultrasensitive biosensing. *Scientific Reports* **6,** 25380. https://doi.org/10.1038/srep25380 (2016).

12. Kabashin, A. V., Patskovsky, S. & Grigorenko, A. N. Phase and amplitude sensitivities in surface plasmon resonance bio and chemical sensing. *Opt. Express* **17,** 21191–21204. https://opg.optica.org/oe/abstract.cfm?URI=oe-17-23-21191 (Nov. 2009).

13. Lin, K.-T., Lin, H., Yang, T. & Jia, B. Structured graphene metamaterial selective absorbers for high efficiency and omnidirectional solar thermal energy conversion. *Nature Communications* **11,** 1389. https://doi.org/10.1038/s41467-020-15116-z (2020).

14. Kafesaki, M., Shen, N. H., Tzortzakis, S. & Soukoulis, C. M. Optically switchable and tunable terahertz metamaterials through photoconductivity. *Journal of Optics* **14,** 114008. https://dx.doi.org/10.1088/2040-8978/14/11/114008 (Sept. 2012).

15. Xomalis, A. *et al.* Enhanced Refractive Index Sensing with Direction-Selective Three-Dimensional Infrared Metamaterials. *ACS Applied Optical Materials* **0,** null. eprint: https://doi.org/10.1021/acsaom.2c00001. https://doi.org/10.1021/acsaom.2c00001 (0).

16. He, J. *et al.* Recent progress and applications of terahertz metamaterials. *Journal of Physics D: Applied Physics* **55,** 123002. https://dx.doi.org/10.1088/1361-6463/ac3282 (Nov. 2021).

17. Landy, N. I., Sajuyigbe, S., Mock, J. J., Smith, D. R. & Padilla, W. J. Perfect Metamaterial Absorber. *Phys. Rev. Lett.* **100,** 207402. https://link.aps.org/doi/10.1103/PhysRevLett.100.207402 (20 May 2008).

18. Zhang, S., Genov, D. A., Wang, Y., Liu, M. & Zhang, X. Plasmon-Induced Transparency in Metamaterials. *Phys. Rev. Lett.* **101,** 047401. https://link.aps.org/doi/10.1103/PhysRevLett.101.047401 (4 July 2008).

19. Wang, Q. *et al.* Broadband metasurface holograms: toward complete phase and amplitude engineering. *Scientific Reports* **6,** 32867. https://doi.org/10.1038/srep32867 (2016).

20. Yu, N. *et al.* Light Propagation with Phase Discontinuities: Generalized Laws of Reflection and Refraction. *Science* **334,** 333–337. eprint: https://www.science.org/doi/pdf/10.1126/science.1210713. https://www.science.org/doi/abs/10.1126/science.1210713 (2011).

21. Ni, X., Kildishev, A. V. & Shalaev, V. M. Metasurface holograms for visible light. *Nature Communications* **4,** 2807. https://doi.org/10.1038/ncomms3807 (2013).

22. Wang, L. *et al.* Artificial birefringent metallic planar structures for terahertz wave polarization manipulation. *Opt. Lett.* **39,** 311–314. https://opg.optica.org/ol/abstract.cfm?URI=ol-39-2-311 (Jan. 2014).

23. Jiang, W. *et al.* Electromagnetic wave absorption and compressive behavior of a three-dimensional metamaterial absorber based on 3D printed honeycomb. *Scientific Reports* **8,** 4817. https://doi.org/10.1038/s41598-018-23286-6 (2018).

24. Yee, K. Numerical solution of initial boundary value problems involving maxwell's equations in isotropic media. *IEEE Transactions on Antennas and Propagation* **14,** 302–307 (1966).

25. Taflove, A. Application of the Finite-Difference Time-Domain Method to Sinusoidal Steady-State Electromagnetic-Penetration Problems. *IEEE Transactions on Electromagnetic Compatibility* **EMC-22,** 191–202 (1980).

26. Slyusar, V. *Metamaterials on antenna solutions* in (Oct. 2009).

27. Farsari, M., Vamvakaki, M. & Chichkov, B. N. Multiphoton polymerization of hybrid materials. *Journal of Optics* **12,** 124001 (2010).

28. Kawata, S., Sun, H.-B., Tanaka, T. & Takada, K. Finer Features for Functional Microdevices. *Nature* **412,** 697–8 (Sept. 2001).

29. Jeon, S., Malyarchuk, V., Rogers, J. A. & Wiederrecht, G. P. Fabricating three dimensional nanostructures using two photon lithography in a single exposure step. *Opt. Express* **14,** 2300–2308. https://opg.optica.org/oe/abstract.cfm?URI=oe-14-6-2300 (Mar. 2006).

30. Lee, K.-S., Yang, D.-Y., Park, S. H. & Kim, R. H. Recent developments in the use of two-photon polymerization in precise 2D and 3D microfabrications. *Polymers for Advanced Technologies* **17,** 72–82. eprint: https://onlinelibrary.wiley.com/doi/pdf/10.1002/pat.664. https://onlinelibrary.wiley.com/doi/abs/10.1002/pat.664 (2006).

31. Zheng, X. *et al.* Multiscale metallic metamaterials. *Nature Materials* **15,** 1100–1106. https://doi.org/10.1038/nmat4694 (2016).

32. Lapine, M. & Tretyakov, S. Contemporary notes on metamaterials. *Microwaves, Antennas  Propagation, IET* **1,** 3–11 (Mar. 2007).

33. Wartak, M. S., Tsakmakidis, K. L. & Hess, O. Introduction to metamaterials. *Physics in Canada* **67,** 30–34 (2011).

34. Taflove, A. *Computational Electrodynamics: The Finite-difference Time-domain Method* ISBN: 9780890067925. https://books.google.gr/books?id=viVRAAAAMAAJ (Artech House, 1995).

35. Markoš, P. & Soukoulis, C. Left-Handed Materials (Jan. 2003).

36. Soukoulis, C. M., Kafesaki, M. & Economou, E. N. Negative-Index Materials: New Frontiers in Optics. *Advanced materials* **18,** 1941–1952 (2006).

37. Courtney, C. Time-domain measurement of the electromagnetic properties of materials. *IEEE Transactions on Microwave Theory and Techniques* **46,** 517–522 (1998).

38. Depine, R. & Lakhtakia, A. A new condition to identify isotropic dielectric-magnetic materials displaying negative phase velocity. *Microwave and Optical Technology Letters* **41,** 315–316 (May 2004).

39. McCall, M. W., Lakhtakia, A. & Weiglhofer, W. S. The negative index of refraction demystified. *European Journal of Physics* **23,** 353–359. https://doi.org/10.1088%2F0143-0807%2F23%2F3%2F314 (May 2002).

40. Sehmi, H. S., Langbein, W. & Muljarov, E. A. Optimizing the Drude-Lorentz model for material permittivity: Method, program, and examples for gold, silver, and copper. *Phys. Rev. B* **95,** 115444. https://link.aps.org/doi/10.1103/PhysRevB.95.115444 (11 Mar. 2017).

41. Rychlewski, J. On Hooke's law. *Journal of Applied Mathematics and Mechanics* **48,** 303–314. ISSN: 0021-8928. https://www.sciencedirect.com/science/article/pii/0021892884901370 (1984).

42. Eldlio, M., Che, F. & Cada, M. in *IAENG Transactions on Engineering Technologies* 41–49 (Springer, 2014).

43. *Theoretical study of despersive materials and metamaterials in 1 and 2 dimensions, S.Papapamakarios* 2021.

44. Griffiths, D. J. *Introduction to Electrodynamics* 4th ed. (Cambridge University Press, 2017).

45. Kinsler, P. & McCall, M. W. Criteria for negative refraction in active and passive media. *Microwave and Optical Technology Letters* **50,** 1804–1807. eprint: https://onlinelibrary.wiley.com/doi/pdf/10.1002/mop.23489. https://onlinelibrary.wiley.com/doi/abs/10.1002/mop.23489 (2008).

46. Chen, Y., Hsueh, Y.-C., Man, M. & Webb, K. J. Enhanced and tunable resolution from an imperfect negative refractive index lens. *J. Opt. Soc. Am. B* **33,** 445–451. https://opg.optica.org/josab/abstract.cfm?URI=josab-33-3-445 (Mar. 2016).

47. Kang, L., Zhao, Q., Zhao, H. & Zhou, J. Magnetically tunable negative permeability metamaterial composed by split ring resonators and ferrite rods. *Opt. Express* **16,** 8825–8834. https://opg.optica.org/oe/abstract.cfm?URI=oe-16-12-8825 (June 2008).

48. Ou, J. Y., Plum, E., Jiang, L. & Zheludev, N. I. Reconfigurable Photonic Metamaterials. *Nano Letters* **11.** PMID: 21480583, 2142–2144. eprint: https://doi.org/10.1021/nl200791r. https://doi.org/10.1021/nl200791r (2011).

49. Lapine, M. *et al.* Structural tunability in metamaterials. *Applied Physics Letters* **95,** 084105 (2009).

50. Laroussi, M. & Roth, J. Numerical calculation of the reflection, absorption, and transmission of microwaves by a nonuniform plasma slab. *IEEE Transactions on Plasma Science* **21,** 366–372 (1993).

51. Zhang, S. *et al.* Experimental Demonstration of Near-Infrared Negative-Index Metamaterials. *Phys. Rev. Lett.* **95,** 137404. https://link.aps.org/doi/10.1103/PhysRevLett.95.137404 (13 Sept. 2005).

52. Smith, D. R., Schultz, S., Marko š, P. & Soukoulis, C. M. Determination of effective permittivity and permeability of metamaterials from reflection and transmission coefficients. *Phys. Rev. B* **65,** 195104. https://link.aps.org/doi/10.1103/PhysRevB.65.195104 (19 Apr. 2002).

53. Kirby, E. I., Hamm, J. M., Tsakmakidis, K. L. & Hess, O. FDTD analysis of slow light propagation in negative-refractive-index metamaterial waveguides. *Journal of Optics A: Pure and Applied Optics* **11,** 114027. https://dx.doi.org/10.1088/1464-4258/11/11/114027 (Sept. 2009).

54. Bilotti, F. & Sevgi, L. Metamaterials: Definitions, properties, applications, and FDTD-based modeling and simulation (Invited paper). *International Journal of RF and Microwave Computer-Aided Engineering* **22,** 422–438. eprint: https://onlinelibrary.wiley.com/doi/pdf/10.1002/mmce.20634. https://onlinelibrary.wiley.com/doi/abs/10.1002/mmce.20634 (2012).

55. Ritter, J. & Amdt, F. Efficient FDTD/matrix-pencil method for the full-wave scattering parameter analysis of waveguiding structures. *IEEE Transactions on Microwave Theory and Techniques* **44,** 2450–2456 (1996).

56. Sullivan, D., Gandhi, O. & Taflove, A. Use of the finite-difference time-domain method for calculating EM absorption in man models. *IEEE Transactions on Biomedical Engineering* **35,** 179–186 (1988).

57. Oskooi, A. F. *et al.* MEEP: A flexible free-software package for electromagnetic simulations by the FDTD method. *Computer Physics Communications* **181,** 687–702 (2010).

58. Umashankar, K., Taflove, A. & Rao, S. Electromagnetic scattering by arbitrary shaped three-dimensional homogeneous lossy dielectric objects. *IEEE Transactions on Antennas and Propagation* **34,** 758–766 (1986).

59. Sullivan, D. M. Exceeding the Courant condition with the FDTD method. *IEEE Microwave and Guided Wave Letters* **6,** 289– (1996).

60. Cassier, M., Joly, P. & Kachanovska, M. Mathematical models for dispersive electromagnetic waves: An overview. *Computers Mathematics with Applications* **74.** Proceedings of the International Conference on Computational Mathematics and Inverse Problems, On occasion of the 60th birthday of Prof. Peter Monk, 2792–2830. ISSN: 0898-1221. https://www.sciencedirect.com/science/article/pii/S0898122117304546 (2017).

61. Al-Jabr, A. & Alsunaidi, M. A General ADE-FDTD Algorithm for the Simulation of Different Dispersive Materials. **1** (Jan. 2009).

62. Sullivan, D. Electromagnetic Simulation Using the FDTD Method, Second Edition. *IEEE Microwave Theory Tech Soc* (May 2013).

63. Shibayama, J., Watanabe, K., Ando, R., Yamauchi, J. & Nakano, H. Frequency-dependent formulations of a Drude-critical points model for explicit and implicit FDTD methods using the trapezoidal RC technique. *IEICE transactions on electronics* **95,** 725–732 (2012).

64. Sullivan, D. Z-transform theory and the FDTD method. *IEEE Transactions on Antennas and Propagation* **44,** 28–34 (1996).

65. Lee, K.-S., Yang, D.-Y., Park, S. H. & Kim, R. H. Recent developments in the use of two-photon polymerization in precise 2D and 3D microfabrications. *Polymers for Advanced Technologies* **17,** 72–82. eprint: https://onlinelibrary.wiley.com/doi/pdf/10.1002/pat.664. https://onlinelibrary.wiley.com/doi/abs/10.1002/pat.664 (2006).

66. Colas des Francs, G., Girard, C., Laroche, T., Lévêque, G. & Martin, O. J. Theory of molecular excitation and relaxation near a plasmonic device. *The Journal of chemical physics* **127,** 034701 (2007).

67. Boyd, R. W. *Nonlinear optics* (Academic press, 2020).

68. Göppert-Mayer, M. Elementary processes with two quantum transitions. *Annalen der Physik* **18,** 466–479 (Aug. 2009).

69. Misawa, H. & Juodkazis, S. *3D laser microfabrication: principles and applications* (John Wiley & Sons, 2006).

70. Varadan, V. K. & Varadan, V. V. *Micro stereo lithography for fabrication of 3D polymeric and ceramic MEMS* in *MEMS Design, Fabrication, Characterization, and Packaging* **4407** (2001), 147–157.

71. Serbin, J. *et al.* Femtosecond laser-induced two-photon polymerization of inorganic–organic hybrid materials for applications in photonics. *Optics letters* **28,** 301–303 (2003).

72. Pawlicki, M., Collins, H. A., Denning, R. G. & Anderson, H. L. Two-photon absorption and the design of two-photon dyes. *Angewandte Chemie International Edition* **48,** 3244–3266 (2009).

73. Lee, K.-S., Kim, R. H., Yang, D.-Y. & Park, S. H. Advances in 3D nano/microfabrication using two-photon initiated polymerization. English. *Progress in Polymer Science* **33,** 631–681 (2008).

74. Faraji Rad, Z., Prewett, P. D. & Davies, G. J. High-resolution two-photon polymerization: the most versatile technique for the fabrication of microneedle arrays. *Microsystems & Nanoengineering* **7,** 71. https://doi.org/10.1038/s41378-021-00298-3 (2021).

75. *Polymer and Photonic Materials Towards Biomedical Breakthroughs* English (eds Van Hoorick, J., Ottevaere, P., Thienpont, H., Dubruel, P. & Van Vlierberghe, S.) ISBN: 978-3-319-75800-8 (Springer International Publishing AG, Switzerland, 2018).

76. Sun, H. & Kawata, S. Two-photon photopolymerization and 3D lithographic microfabrication. *Advances in Polymer Science* **170,** 169–273 (2005).

77. Schmidt, V., Kuna, L., Satzinger, V., Jakopic, G. & Leising, G. Two-photon 3D lithography: A Versatile Fabrication Method for Com-plex 3D Shapes and Optical Interconnects within the Scope of Innovative Industrial ... *JLMN-Journal of Laser Micro/Nanoengineering* **2** (Oct. 2007).

78. Psycharakis, S., Tosca, A., Melissinaki, V., Giakoumaki, A. & Ranella, A. Tailor-made three-dimensional hybrid scaffolds for cell cultures. *Biomedical materials (Bristol, England)* **6,** 045008 (Aug. 2011).

79. Skliutas, E. *et al. Nanophotonics* **10,** 1211–1242. https://doi.org/10.1515/nanoph-2020-0551 (2021).

80. Schmidt, H. K. Inorganic-organic composites by sol-gel techniques (1994).

81. Speight, J. G. in *Reaction Mechanisms in Environmental Engineering* (ed Speight, J. G.) 337–384 (Butterworth-Heinemann, 2018). ISBN: 978-0-12-804422-3. https://www.sciencedirect.com/science/article/pii/B9780128044223000109.

82. Wen, J. & Wilkes, G. L. Organic/Inorganic Hybrid Network Materials by the SolGel Approach. *Chemistry of Materials* **8,** 1667–1681. eprint: https://doi.org/10.1021/cm9601143. https://doi.org/10.1021/cm9601143 (1996).

83. Chattopadhyay, D. & Kothapalli, R. V. Structural engineering of polyurethane coatings for high performance applications. *Progress in Polymer Science* **32,** 352–418 (Mar. 2007).

84. Ladika, D. *et al.* Synthesis and application of triphenylamine-based aldehydes as photo-initiators for multi-photon lithography. *Applied Physics A* **128,** 745. https://doi.org/10.1007/s00339-022-05887-1 (2022).

85. Žukauskas, A. *et al.* Effect of the photoinitiator presence and exposure conditions on laser-induced damage threshold of ORMOSIL (SZ2080). *Optical Materials* **39,** 224–231. ISSN: 0925-3467. https://www.sciencedirect.com/science/article/pii/S0925346714005710 (2015).

86. Ovsianikov, A. *et al.* Ultra-Low Shrinkage Hybrid Photosensitive Material for Two-Photon Polymerization Microfabrication. *ACS Nano* **2,** 2257–2262. eprint: https://doi.org/10.1021/nn800451w. https://doi.org/10.1021/nn800451w (2008).

87. Schroeder, W. F., Asmussen, S. L., Cook, W. D. & Vallo, C. I. Efficiency of 4,4-bis(N,N-diethylamino) benzophenone for the polymerization of dimethacrylate resins in thick sections. *Polymer International* **60,** 1362–1369. eprint: https://onlinelibrary.wiley.com/doi/pdf/10.1002/pi.3089. https://onlinelibrary.wiley.com/doi/abs/10.1002/pi.3089 (2011).

88. Sakellari, I. *et al.* Quantum dot based 3D printed woodpile photonic crystals tuned for the visible. *Nanoscale Adv.* **1,** 3413–3423. http://dx.doi.org/10.1039/C9NA00357F (9 2019).

89. Schizas, C. *et al.* On the design and fabrication by two-photon polymerization of a readily assembled micro-valve. *The International Journal of Advanced Manufacturing Technology* **48,** 435–441 (2010).

90. Scheps, R. & Myers, J. F. Performance of a diode-pumped laser repetitively Q-switched with a mechanical shutter. *Applied Optics* **33,** 969–978 (1994).

91. Yoshida, A., Kaburagi, Y. & Hishiyama, Y. in *Materials Science and Engineering of Carbon* (eds Inagaki, M. & Kang, F.) 71–93 (Butterworth-Heinemann, 2016). ISBN: 978-0-12-805256-3. https://www.sciencedirect.com/science/article/pii/B9780128052563000052.

92. Smith, K. C. A. & Oatley, C. W. The scanning electron microscope and its fields of application. *British Journal of Applied Physics* **6,** 391. https://dx.doi.org/10.1088/0508-3443/6/11/304 (Nov. 1955).

93. Hossain, M. I., Faruque, M. R. I., Islam, M. T. & Ullah, M. H. A New Wide-Band Double-Negative Metamaterial for C- and S-Band Applications. *Materials* **8,** 57–71. ISSN: 1996-1944. https://www.mdpi.com/1996-1944/8/1/57 (2015).

94. Ghosh, S., Bhattacharyya, S., Chaurasiya, D. & Srivastava, K. V. An Ultrawideband Ultrathin Metamaterial Absorber Based on Circular Split Rings. *IEEE Antennas and Wireless Propagation Letters* **14,** 1172–1175 (2015).

95. Katsarakis, N., Koschny, T., Kafesaki, M., Economou, E. & Soukoulis, C. Electric coupling to the magnetic resonance of split ring resonators. *Applied physics letters* **84,** 2943–2945 (2004).

96. Li, S., Shen, Z., Yin, W., Zhang, L. & Chen, X. 3D printed cross-shaped terahertz metamaterials with single-band, multi-band and broadband absorption. *Optical Materials* **122,** 111739. ISSN: 0925-3467. https://www.sciencedirect.com/science/article/pii/S0925346721009393 (2021).

97. Vafapour, Z. & Forouzeshfard, M. R. Disappearance of Plasmonically Induced Reflectance by Breaking Symmetry in Metamaterials. *Plasmonics* **12,** 1331–1342. https://doi.org/10.1007/s11468-016-0391-2 (2017).

98. Liu, N. *et al.* Planar Metamaterial Analogue of Electromagnetically Induced Transparency for Plasmonic Sensing. *Nano Letters* **10.** PMID: 20017551, 1103–1107. eprint: https://doi.org/10.1021/nl902621d. https://doi.org/10.1021/nl902621d (2010).

99. Cen, C. *et al.* A dual-band metamaterial absorber for graphene surface plasmon resonance at terahertz frequency. *Physica E: Low-dimensional Systems and Nanostructures* **117,** 113840. ISSN: 1386-9477. https://www.sciencedirect.com/science/article/pii/S1386947719309932 (2020).

100. Singh, R. *et al.* The Fano Resonance in Symmetry Broken Terahertz Metamaterials. *IEEE Transactions on Terahertz Science and Technology* **3** (Jan. 2014).

101. Hau, L. V., Harris, S. E., Dutton, Z. & Behroozi, C. H. Light speed reduction to 17 metres per second in an ultracold atomic gas. *Nature* **397,** 594–598. https://doi.org/10.1038/17561 (1999).

102. Phillips, D. F., Fleischhauer, A., Mair, A., Walsworth, R. L. & Lukin, M. D. Storage of Light in Atomic Vapor. *Phys. Rev. Lett.* **86,** 783–786. https://link.aps.org/doi/10.1103/PhysRevLett.86.783 (5 Jan. 2001).

103. Fleischhauer, M., Imamoglu, A. & Marangos, J. P. Electromagnetically induced transparency: Optics in coherent media. *Rev. Mod. Phys.* **77,** 633–673. https://link.aps.org/doi/10.1103/RevModPhys.77.633 (2 July 2005).

104. Singh, R., Rockstuhl, C., Lederer, F. & Zhang, W. Coupling between a dark and a bright eigenmode in a terahertz metamaterial. *Phys. Rev. B* **79,** 085111. https://link.aps.org/doi/10.1103/PhysRevB.79.085111 (8 Feb. 2009).

105. Tassin, P. *et al.* Electromagnetically induced transparency and absorption in metamaterials: the radiating two-oscillator model and its experimental confirmation. *Physical review letters* **109,** 187401 (2012).

106. Terzaki, K. *et al.* 3D conducting nanostructures fabricated using direct laser writing. *Opt. Mater. Express* **1,** 586–597. https://opg.optica.org/ome/abstract.cfm?URI=ome-1-4-586 (Aug. 2011).

107. Mattox, D. M. *Handbook of physical vapor deposition (PVD) processing* (William Andrew, 2010).

108. Pierson, H. O. *Handbook of chemical vapor deposition: principles, technology and applications* (William Andrew, 1999).

109. Vasilantonakis, N. *et al.* Three-dimensional metallic photonic crystals with optical bandgaps. *Advanced Materials* **24,** 1101–1105 (2012).

110. Dorney, T. D., Baraniuk, R. G. & Mittleman, D. M. Material parameter estimation with terahertz time-domain spectroscopy. *JOSA A* **18,** 1562–1571 (2001).

111. Zhao, G., Schouten, R. N., van der Valk, N., Wenckebach, W. T. & Planken, P. C. M. Design and performance of a THz emission and detection setup based on a semi-insulating GaAs emitter. *Review of Scientific Instruments* **73,** 1715–1719. eprint: https://doi.org/10.1063/1.1459095. https://doi.org/10.1063/1.1459095 (2002).

112. Norman, T. in *Integrated Security Systems Design (Second Edition)* (ed Norman, T.) Second Edition, 251–266 (Butterworth-Heinemann, Boston, 2014). ISBN: 978-0-12-800022-9. https://www.sciencedirect.com/science/article/pii/B9780128000229000127.

113. Markoš, P. & Soukoulis, C. M. Transmission properties and effective electromagnetic parameters of double negative metamaterials. *Opt. Express* **11,** 649–661. https://opg.optica.org/oe/abstract.cfm?URI=oe-11-7-649 (Apr. 2003).

114. Lipson, R. & Lu, C. Photonic crystals: A unique partnership between light and matter. *EUROPEAN JOURNAL OF PHYSICS Eur. J. Phys* **30,** 33–48 (July 2009).

115. Yablonovitch, E. Inhibited Spontaneous Emission in Solid-State Physics and Electronics. *Phys. Rev. Lett.* **58,** 2059–2062. https://link.aps.org/doi/10.1103/PhysRevLett.58.2059 (20 May 1987).

116. John, S. Strong localization of photons in certain disordered dielectric superlattices. *Phys. Rev. Lett.* **58,** 2486–2489. https://link.aps.org/doi/10.1103/PhysRevLett.58.2486 (23 June 1987).

117. Ho, K. M., Chan, C. T. & Soukoulis, C. M. Existence of a photonic gap in periodic dielectric structures. *Phys. Rev. Lett.* **65,** 3152–3155. https://link.aps.org/doi/10.1103/PhysRevLett.65.3152 (25 Dec. 1990).

118. Yablonovitch, E., Gmitter, T. J. & Leung, K. M. Photonic band structure: The face-centered-cubic case employing nonspherical atoms. *Phys. Rev. Lett.* **67,** 2295–2298. https://link.aps.org/doi/10.1103/PhysRevLett.67.2295 (17 Oct. 1991).

119. El-Kady, I., Sigalas, M., Biswas, R., Ho, K. & Soukoulis, C. Metallic photonic crystals at optical wavelengths. *Physical Review B* **62,** 15299 (2000).

120. Němec, H. *et al.* Highly tunable photonic crystal filter for the terahertz range. *Optics letters* **30,** 549–551 (2005).

121. Nair, R. V. & Vijaya, R. Photonic crystal sensors: An overview. *Progress in Quantum Electronics* **34,** 89–134 (2010).

122. Luo, C., Johnson, S. G., Joannopoulos, J. & Pendry, J. Subwavelength imaging in photonic crystals. *Physical Review B* **68,** 045115 (2003).

123. Lin, S.-Y., Moreno, J. & Fleming, J. Three-dimensional photonic-crystal emitter for thermal photovoltaic power generation. *Applied physics letters* **83,** 380–382 (2003).

124. Fenzl, C., Hirsch, T. & Wolfbeis, O. S. Photonic crystals for chemical sensing and biosensing. *Angewandte Chemie International Edition* **53,** 3318–3335 (2014).

125. Kabashin, A. V. *et al.* Plasmonic nanorod metamaterials for biosensing. *Nature materials* **8,** 867–871 (2009).

126. Kabouraki, E. *et al. Nanophotonics* **10,** 3759–3768. https://doi.org/10.1515/nanoph-2021-0263 (2021).

127. Vedam, K. Spectroscopic ellipsometry: a historical overview. *Thin solid films* **313,** 1–9 (1998).

128. Chance, K. & Kurucz, R. An improved high-resolution solar reference spectrum for earth's atmosphere measurements in the ultraviolet, visible, and near infrared. *Journal of Quantitative Spectroscopy and Radiative Transfer* **111.** Special Issue Dedicated to Laurence S. Rothman on the Occasion of his 70th Birthday., 1289–1295. ISSN: 0022-4073. https://www.sciencedirect.com/science/article/pii/S0022407310000610 (2010).

129. Dickinson, R. E. & Cicerone, R. J. Future global warming from atmospheric trace gases. *Nature* **319,** 109–115 (1986).

130. Diem, M., Koschny, T. & Soukoulis, C. M. Wide-angle perfect absorber/thermal emitter in the terahertz regime. *Phys. Rev. B* **79,** 033101. https://link.aps.org/doi/10.1103/PhysRevB.79.033101 (3 Jan. 2009).

131. Celanovic, I., Perreault, D. & Kassakian, J. Resonant-cavity enhanced thermal emission. *Phys. Rev. B* **72,** 075127. https://link.aps.org/doi/10.1103/PhysRevB.72.075127 (7 Aug. 2005).

132. Galli, I. *et al.* Molecular Gas Sensing Below Parts Per Trillion: Radiocarbon-Dioxide Optical Detection. *Phys. Rev. Lett.* **107,** 270802. https://link.aps.org/doi/10.1103/PhysRevLett.107.270802 (27 Dec. 2011).

133. Ishak, B. Spectra of atoms and molecules (3rd edition), by Peter F. Bernath. *Contemporary Physics* **58,** 201–202. eprint: https://doi.org/10.1080/00107514.2017.1291731. https://doi.org/10.1080/00107514.2017.1291731 (2017).

134. Lalic, B. *et al. Agricultural Meteorology and Climatology* ISBN: 978-88-6453-795-5 (Dec. 2018).

135. Shao, W. *et al.* Facile synthesis of low temperature sintering Ag nanopaticles for printed flexible electronics. *Journal of Materials Science: Materials in Electronics* **29** (Mar. 2018).

136. Lochbaum, A. *et al.* Compact Mid-Infrared Gas Sensing Enabled by an All-Metamaterial Design. *Nano Letters* **20.** PMID: 32343585, 4169–4176. eprint: https://doi.org/10.1021/acs.nanolett.0c00483. https://doi.org/10.1021/acs.nanolett.0c00483 (2020).

137. Smith, D. R., Vier, D. C., Koschny, T. & Soukoulis, C. M. Electromagnetic parameter retrieval from inhomogeneous metamaterials. *Phys. Rev. E* **71,** 036617. https://link.aps.org/doi/10.1103/PhysRevE.71.036617 (3 Mar. 2005).

138. Cen, C. *et al.* High Quality Factor, High Sensitivity Metamaterial Graphene—Perfect Absorber Based on Critical Coupling Theory and Impedance Matching. *Nanomaterials* **10.** ISSN: 2079-4991. https://www.mdpi.com/2079-4991/10/1/95 (2020).

139. Li, S., Zhang, L. & Chen, X. 3D-printed terahertz metamaterial absorber based on vertical split-ring resonator. *Journal of Applied Physics* **130,** 034504. eprint: https://doi.org/10.1063/5.0056276. https://doi.org/10.1063/5.0056276 (2021).

140. Marcelli, A., Cricenti, A., Kwiatek, W. & Petibois, C. Biological applications of synchrotron radiation infrared spectromicroscopy. *Biotechnology advances* **30,** 1390–404 (Feb. 2012).

141. Alharbi, F. H. & Kais, S. Theoretical limits of photovoltaics efficiency and possible improvements by intuitive approaches learned from photosynthesis and quantum coherence. *Renewable and Sustainable Energy Reviews* **43,** 1073–1089. ISSN: 1364-0321. https://www.sciencedirect.com/science/article/pii/S136403211401048X (2015).

142. Hong, Y. J. *et al.* Visible-color-tunable light-emitting diodes. *Advanced materials* **23,** 3284–3288 (2011).

143. Rao, A. & Friend, R. H. Harnessing singlet exciton fission to break the Shockley–Queisser limit. *Nature Reviews Materials* **2,** 17063. https://doi.org/10.1038/natrevmats.2017.63 (2017).

144. AlShareef, M. R. & Ramahi, O. M. Electrically small resonators for energy harvesting in the infrared regime. *Journal of Applied Physics* **114,** 223101. eprint: https://doi.org/10.1063/1.4846076. https://doi.org/10.1063/1.4846076 (2013).

145. Bade, W. Drude-Model Calculation of Dispersion Forces. I. General Theory. *The Journal of Chemical Physics* **27,** 1280–1284 (1957).

146. Pillai, S., Catchpole, K. R., Trupke, T. & Green, M. A. Surface plasmon enhanced silicon solar cells. *Journal of Applied Physics* **101,** 093105. eprint: https://doi.org/10.1063/1.2734885. https://doi.org/10.1063/1.2734885 (2007).